

Rita Joana Rodrigues da Silva Rua Ferreira

Licenciada em Anatomia Patológica, Citológica e Tanatológica



Cilia motility studies in zebrafish embryos

Dissertação para a obtenção do Grau de Mestre em
Genética Molecular e Biomedicina

Orientador: Susana Santos Lopes,
Investigadora Principal, Centro de Estudos de Doenças Crónicas,
Faculdade de Ciências Médicas, Universidade Nova de Lisboa

Co-orientador: Paula Gonçalves, Professora Auxiliar,
Faculdade Ciências e Tecnologia, Universidade Nova de Lisboa

Júri:

Presidente: Prof. Dra Paula Gonçalves
Arguente: Dr. Jorge Carneiro
Vogal: Dra. Susana Santos Lopes

Cilia motility studies in zebrafish embryos

Submitted by

Rita Joana Rodrigues da Silva Rua Ferreira

A thesis submitted in fulfilment of the requirements for the degree of

Masters in Molecular Genetics and Biomedicine

October 2012

Cilia motility studies in zebrafish

Copyright Rita Joana Rodrigues da Silva Rua Ferreira, FCT/UNL, UNL

A Faculdade de Ciências e Tecnologia e a Universidade Nova de Lisboa têm o direito, perpétuo e sem limites geográficos, de arquivar e publicar esta dissertação através de exemplares impressos reproduzidos em papel ou de forma digital, ou por qualquer outro meio conhecido ou que venha a ser inventado, e de a divulgar através de repositórios científicos e de admitir a sua cópia e distribuição com objectivos educacionais ou de investigação, não comerciais, desde que seja dado crédito ao autor e editor.

**To my family,
Tiago and Sara.**

Acknowledgements

First, I would like to thank Susana Lopes, my supervisor, for being such a good scientist and for knowing how to motivate her students to accomplish more and more. Our snack breaks were always a nice place for discussions and new ideas came from that. Thank you for giving me the opportunity to work in a newly established lab and for encouraging me to search new scientific challenges. For all this time thank you for being my friend and for being so quickly in correcting my thesis. I will never forget our support and I hope we will meet again in a near future.

I thank Petra and Bárbara for this last year of laughing and nice work environment. Our lab was always a funny place to work and learn with our discussions. I will miss our lunch times where Bárbara has always new amazing things to tell us. She knows a lot about everything. Thank you for your support during this time. I wish the best for both of you.

I would like to thank Cláudia and Marta for being such a nice lab neighbors. We became friends and now I am sure I will miss you a lot. Hope you will come to Strasbourg to visit me.

I also thank Maysa Franco and Liliana Vale for taking care of IGC's Fish Facility. I could not forget Pedro Almada for all the help in the Spinning Disk. During this year I bugged you a lot and you always help me. Thanks, thanks, thanks!!!

I would like to thank specially to my family just for being there every time I needed. My mood after work made me treated you not always the best way but I love you all and without your support nothing of this would be possible. Thanks Pai João, Mãe Té, Jotapê, Gui, Inês e Catarina. Thanks also to my grandparents that don't have a clue on what I am doing so far but supported me all my whole life. I dedicate this work to all my family.

Another special thanks to my boyfriend Tiago, that always tried to kept my mind out of work. Thank you for the times we spent watching sport channels, USA Open, *Rolando Garros*, among others, because sometimes I really needed your 'wake-up call' to see that life is not all work, work and work. Thank you for your unconditional love!

A special thanks to my best friend Sara that loves and supports me unconditionally although in the last year she had my company just a few times. Work always kept me distant from our meetings. Fortunately cell phones exist and you still considered myself as your 'sister'! Thanks for your support. I dedicate this work also to you, Sara.

Finally, my deepest gratitude goes to Adán Guerrero for teaching me so many things about science. Without you this work would not have been possible in the way it was. You are a really good scientist and teacher and I am sure that your future will be great. I am feeling very lucky for having you as a friend. I will never forget what you did for me. Thank you SO MUCH!

Abstract

Motile ciliary dysfunctions cause specific Ciliopathies that affect mainly the respiratory tract, fertilization and left-right body establishment. The embryonic organ where left-right decisions are first taken is called the organizer, a ciliated organ where a leftward cilia driven fluid-flow is generated. The organizer is named node in the mouse and Kupffer's vesicle (KV) in zebrafish. The correct left-right axis formation is highly dependent on signaling pathways downstream of such directional fluid-flow.

Motile cilia need to be coordinated and Ciliary Beat Frequency (CBF) is characteristic of different types of cilia depending on their function. Using zebrafish as a model, our group has been studying cilia length regulation and motility in wild-type and *deltaD*^{-/-} mutant embryos. Recently, we showed that *Notch* signalling was directly involved in the control of cilia length in the KV cells given that the *deltaD*^{-/-} mutant present shorter KV cilia.

The goal of this project was to characterize the CBF of *deltaD*^{-/-} KV cilia vs. wild-type cilia and reveal how potential differences in CBF impact on KV fluid flow, using spectral analysis associated with high-speed videomicroscopy. By decomposing and comparing the obtained CBF with Fast Fourier Transform, we identified two major populations of motile cilia in wild-type as well as in *deltaD*^{-/-} mutant embryos. However, we found the CBF populations had differential relative contributions and different distributions between wild-type and mutant embryos. Furthermore, by measuring the velocity of native particles we studied the KV fluid-flow and concluded that the dispersion of the flow velocity was much wider in the *deltaD*^{-/-} mutants. On the other hand, based on a gene expression study of motility genes downstream of DeltaD, we concluded that motility related genes (*dnah7*, *rsph3* and *foxj1a*) were deregulated in the mutants.

During this project we generated data that led to new hypotheses that will allow us to test the causality between the described correlations.

Key-words: Kupffer's vesicle, motile cilia, cilia beat frequency, fluid-flow, *deltaD*^{-/-} mutants

Resumo

Cílios primários disfuncionais causam Ciliopatias que afectam principalmente o trato respiratório, a taxa de fertilização e o estabelecimento do eixo esquerda-direita. O órgão embrionário onde primeiramente são tomadas decisões relativas ao eixo esquerda-direita é denominado de 'organizador'. É um órgão ciliado onde um fluido direcionado para a esquerda é gerado pelo movimento dos cílios. Este 'organizador' é denominado de 'nó' no rato e de 'vesícula de Kupffer' (VK) no peixe-zebra. A correta formação do eixo direita-esquerda é altamente dependente das vias de sinalização a jusante do fluxo direcional para a esquerda.

Os cílios móveis necessitam de ser coordenados e a frequência de batimento ciliar (FBC) é característica de cada tipo de cílio e está dependente da sua função. Usando o peixe-zebra como modelo, o nosso grupo tem vindo a estudar a regulação do tamanho e da motilidade ciliar em embriões *selvagens* e em mutantes *deltaD^{-/-}*. Recentemente, o nosso grupo mostrou que a sinalização *Notch* está diretamente envolvida no controlo do tamanho dos cílios das células da VK, tendo em conta que os mutantes *deltaD^{-/-}* apresentam cílios curtos.

O objectivo deste projeto foi a caracterização das FBC dos mutantes *deltaD^{-/-}* em comparação com embriões *wild-type*, e revelar qual o impacto de potenciais diferenças das FBC no fluxo do fluido da VK. Realizámos uma análise espectral dos cílios individualmente, através da utilização de vídeo-microscopia de alta velocidade. Por decomposição e comparação das FBC obtidas com a transformada rápida de Fourier, identificámos duas populações de cílios móveis tanto em embriões selvagens como nos mutantes *deltaD^{-/-}*. Para além disso, medimos a velocidade através da filmagem de partículas naturalmente existentes na VK, estudámos o fluxo do fluido e concluímos que existia uma maior dispersão dos valores de velocidade das partículas nos mutantes. Por outro lado, com base num estudo de expressão genética realizado em genes relacionados com a motilidade ciliar a jusante do DeltaD, observámos que três desses genes (*dnah7*, *rsph3* and *foxj1a*) apresentavam uma expressão desregulada nos mutantes *deltaD^{-/-}*.

Até agora, mostrámos que não só os cílios são mais curtos na VK dos mutantes *deltaD^{-/-}*, como a sua motilidade é diferente. A expressão de genes de motilidade também está desregulada.

Durante este projecto obtivemos dados que nos direccionaram para novas hipóteses, que nos permitirão testar a causalidade entre as correlações descritas.

Palavras chave: Vesícula de Kupffer, cílios móveis, frequência de batimento ciliar, fluxo, mutantes *deltaD^{-/-}*

General index

Acknowledgements	ix
Abstract	xi
Resumo	xiii
 General index	 xv
Figures index	xix
Tables index	xxi
 1. Introduction	 1
1.1. Cilia and flagella	3
1.1.1. Cilia localization	5
1.2. Ciliopathies	7
1.2.1. Primary ciliary dyskinesia	8
1.3. Role of cilia in the left-right patterning	9
1.3.1. The two left-right models	9
1.3.2. Left-right signaling cascade	11
1.4. Embryonic left-right organizers	11
1.4.1. Mouse node	11
1.4.2. Zebrafish Kupffer's vesicle	14
1.5. Motile cilia generated flow in zebrafish	17
1.5.1. Motile cilia beat pattern	17
1.5.2. Motile Cilia Beat Frequency	17
1.5.3. Fluid hydrodynamics	18
1.5.4. Directional flow	19
1.5.5. Interplay between models and experiments	21
1.6. Project goals	22

2. Materials and Methods	23
2.1. Recording Cilia Beat Frequencies in the Kupffer's vesicle	25
2.1.1. Zebrafish mating	25
2.1.2. Mounting zebrafish live embryos for recording Cilia Beat Frequency in the Kupffer's vesicle	25
2.1.3. Microscope setup	26
2.1.4. Recording Kupffer's vesicle cilia – image frames acquisition	27
2.1.5. Image processing and kymograph design	28
2.1.6. Cilia Beat Frequency spectral analysis	30
2.1.7. Statistical analysis of Cilia Beat Frequency results	31
2.2. Cilia localization/distribution inside Kupffer's vesicle	31
2.3. High-speed videomicroscopy for measuring the Kupffer's vesicle fluid flow	32
2.4. Molecular study of motility genes downstream of DeltaD	33
2.4.1. Whole-mount <i>in situ</i> Hybridization	33
2.4.2. Quantitative real-time Polymerase Chain Reaction	34
2.4.3. Cloning of <i>dynein axonemal heavy chain 7</i> (dnah7)	36
2.4.3.1. PCR amplification	36
2.4.3.2. <i>dnah7</i> cloning into pGEM®-T easy vector system	37
2.4.3.3. mRNA <i>in vitro</i> transcription and probe production	38
3. Results	41
3.1. Recording Cilia Beat Frequencies in the Kupffer's vesicle	43
3.1.1. Cilia Beat Frequency analysis in wild-type identifies two cilia populations	43
3.1.2. <i>deltaD</i> ^{-/-} mutants have a wider range of Cilia Beat Frequencies	46
3.2. Cilia localization/distribution in the Kupffer's vesicle	50
3.3. High-speed videomicroscopy for measuring the Kupffer's vesicle fluid flow	51
3.3.1. Cilia Beat Frequency variations seem to affect KV vesicle fluid flow	51
3.4. Molecular study of motility genes downstream of DeltaD	52
3.4.1. Motility related genes are differently expressed in <i>deltaD</i> ^{-/-} mutants	52

3.4.1.1.	<i>dnah7</i> gene expression	53
3.4.1.2.	<i>foxj1a</i> gene expression	53
3.4.1.3.	<i>rsph3</i> gene expression	54
3.4.2.	Motile-related genes were up-regulated in <i>deltaD</i> ^{-/-} mutants by qPCR	56
4.	Discussion	59
	References	65
	Annex I	73
	Annex II	77
	Anexx III	89

Figures index

Figure 1.1 – Schematics of a 9+2 configuration cilia	3
Figure 1.2 – The green alga <i>Chlamydomonas reinhardtii</i> with two motile cilia/flagella	4
Figure 1.3 – The ciliated Tetrahymena	4
Figure 1.4 - Motile and primary cilia in diverse organisms and cell types	5
Figure 1.5 – Schematic representation of “9+2” and “9+0” axoneme cross-sections and IFT	6
Figure 1.6 - Organs affected in human Ciliopathies	7
Figure 1.7 – Body plan and axes in zebrafish: anterior-posterior, dorsal-ventral, left-right	9
Figure 1.8 – Schematic representation of the two L-R models	10
Figure 1.9 – Scanning Electron micrographs of a mouse node	12
Figure 1.10 - Model of the generation of nodal flow	12
Figure 1.11 – Trajectory of Node Cilia Movement	13
Figure 1.12 – Cilium in wild-type mouse node	13
Figure 1.13 – DIC images of the zebrafish KV	14
Figure 1.14 – Immunofluorescence experiment for visualizing KV cilia	15
Figure 1.15 – Typical three-dimensional (3-D) reconstructions of confocal data sets of KV cilia at the 9 th somite stage projected in the Cave	16
Figure 1.16 – Mouse, medaka and zebrafish left-right organizers	16
Figure 1.17 - Fluid dynamics at low Reynolds number	19
Figure 1.18 - Pumping flow with motile cilia at low Reynolds numbers	20
 Figure 2.1 – Mounting of zebrafish live embryos for recording CBF in the KV	 25
Figure 2.2 – DIC image of a zebrafish KV from a live embryo filmed from the dorsal side	26
Figure 2.3 – ROI representation	27
Figure 2.4 – Motile cilia after image processing	28
Figure 2.5 – ImageJ kymograph design	29
Figure 2.6 – Kymograph with the traced line represented	29
Figure 2.7 - Fast Fourier transform (FFT) spectral analysis	30
Figure 2.8 – Schematic Kupffer’s vesicle used to annotate cilia localization	31

Figure 2.9 - Zebrafish KV with a tracked particle inside	32
Figure 2.10 – Example of a plate for qPCR	36
Figure 2.11 – Scheme of pGEM®-T easy vector system	38
Figure 3.1 – WT CBF population	43
Figure 3.2 – WT cilia population with single CBFs	44
Figure 3.3 - WT cilia population with double CBFs	45
Figure 3.4 - Classification of double CBFs into dominant and secondary frequencies of the WT double cilia population	46
Figure 3.5 – <i>deltaD</i> ^{-/-} mutants CBF population	47
Figure 3.6 - <i>deltaD</i> ^{-/-} cilia population with single CBFs	47
Figure 3.7 - <i>deltaD</i> ^{-/-} cilia population with double CBFs	48
Figure 3.8 - Classification of double CBFs into dominant and secondary frequencies of the <i>deltaD</i> ^{-/-} double cilia population	49
Figure 3.9 – Spatial distribution of the two motile cilia populations in the KV	50
Figure 3.10 - Comparison of KV fluid flow velocity between WT and <i>deltaD</i> ^{-/-} mutant embryos	51
Figure 3.11 – WISH experiment for <i>ntl</i> gene in WT 8 th somite-stage embryos	52
Figure 3.12 – WISH experiment for <i>dnah7</i> in WT (upper panel) and <i>deltaD</i> ^{-/-} mutants at 8 th somite-stage embryos (lower panel)	53
Figure 3.13 – WISH experiment for <i>foxf1a</i> in WT (upper panel) and <i>deltaD</i> ^{-/-} mutants at bud-stage and 8 th somite-stage embryos (lower panel)	54
Figure 3.14 – WISH experiment for <i>rsph3</i> in Wild-type (upper panel) and <i>deltaD</i> ^{-/-} mutants at 8 th somite-stage embryos (lower panel)	55
Figure 3.15 – Gene expression analysis of cilia motility-related genes by qPCR in WT and <i>deltaD</i> ^{-/-} mutants	56

Tables index

Table 1.1 – Cilia properties in various embryonic models	18
Table 2.1 – WISH experiment	34
Table 2.2 – qPCR analysis	35
Table 2.3 – Reaction mixture for the <i>dnah7</i> DNA ligation with pGEM®-T easy vector system	37
Table 2.4 – Reaction mixture for <i>dnah7</i> insert release with <i>Not I</i>	38
Table 2.5 – Reaction mixture for the plasmid digestion with <i>SacI</i>	39
Table 2.6 – Reaction mixture for the plasmid digestion with <i>SacII</i>	39
Table 2.7 – Reaction mixture for <i>in vitro</i> transcription and RNA probe production	40
Table 3.1 – Summary statistics over variability in CBF	49
Table 3.2 – Summary of the molecular study on motility genes downstream of DeltaD	57

CHAPTER 1

Introduction

1.1 Cilia and Flagella

Cilia and flagella are ubiquitous antenna-like organelles encountered from protists to mammals that protrude out of nearly all vertebrate cells into the local environment (Supatto & Vermot 2011; Fliegauf et al. 2007).

The distinction between cilia and flagella is mostly historical, as both organelles display a common architecture (Theegarten & Ebsen 2011; Afzelius 1995). Cilia were probably first observed and their motile function appreciated by Antony van Leeuwenhoek in 1674-75, although the term for these organelles was probably first used by Otto Friedrich Müller in 1786 (reviewed in Bloodgood 2010).

Cilia and flagella number, length and disposition can be highly variable from one cell type to another. They elongate from a basal body, made of nine triplets of microtubules surrounding a cartwheel, a hub-like central axis with radiating arm-like extensions located at the proximal tip of the basal body (Vincensini et al. 2011). The core structure of cilia and flagella is the axoneme, a cylinder composed of nine doublets of microtubules (Vincensini et al. 2011) - Figure 1.1.

Cilia and flagella play important roles in cellular motility, signal transduction, embryonic development, and human disease (Nicastro et al. 2011), and can be found in several distinct organs and tissues (Figure 1.4).

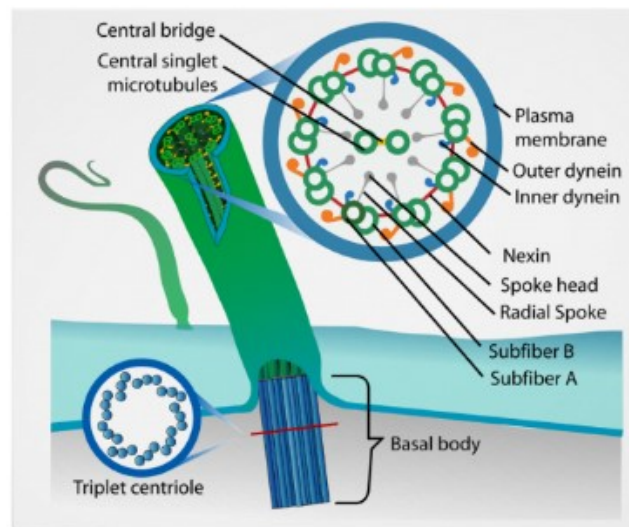


Figure 1.1 – Schematics of a 9+2 configuration cilia. Representation of a basal body and a cross section of a 9+2 axoneme. Adapted by Bloodgood et al. (Bloodgood 2010).

The most striking function of cilia and flagella is their involvement in cell motility. In protists, flagella propel the organism in the aqueous environment, a feature also displayed by gametes in many species (Vincensini et al. 2011; Guerrero et al. 2011).

Many major discoveries about cilia have been made in ‘simple’ organisms such as the nematode *Caenorhabditis elegans*, the unicellular alga *Chlamydomonas reinhardtii* (Figure 1.2), the ciliates

Paramecium and *Tetrahymena* (Figure 1.3), or the kinetoplastid *Trypanosoma*, that are more amenable to experimentation and genetic manipulation than vertebrate models – mouse, *zebrafish* and *Xenopus* (Vincensini et al. 2011). Ciliates such as *Paramecium* and *Tetrahymena* are solid models for cilia studies, especially for the understanding of basal body and centriole assembly (Vincensini et al. 2011).



Figure 1.2 – The green alga *Chlamydomonas reinhardtii* with two motile cilia/flagella. The green alga *Chlamydomonas* possesses two flagella (~12 μm in length) that protrude from the apical end of the cell. The flagella beat in a breaststroke fashion and play an important role in response to light and in gamete adhesion. *Chlamydomonas* displays numerous practical and technical advantages for the study of the eukaryotic flagellum. *Chlamydomonas* cells exhibit complex swimming behaviours in response to various light stimuli, allowing for the dissection of flagellar beating regulatory pathways (Vincensini et al. 2011). Adapted from (Vincensini et al. 2011).



Figure 1.3 – The ciliated *Tetrahymena*. The 50 μm long *Tetrahymena* cell contains approximately 750 basal bodies. The huge number of cilia and basal bodies is a great advantage for biochemical studies of basal bodies, RNAi (RNA interference) studies, GFP tagging, genetic knockins and knockouts, and ultrastructural studies (Vincensini et al. 2011).

The synthesis of structural and functional components of cilia occurs in the cytoplasm and a specialized system termed intraflagellar transport (IFT), is responsible for moving cargo (IFT particles) toward the axonemal tip or away from it (anterograde and retrograde transport, respectively - Figure 1.5c). Pioneering work in the green alga *Chlamydomonas reinhardtii*, led to the discovery and exhaustive characterization of a large number of genes involved in flagellum motility and construction, such as axonemal dynein motors (reviewed in (Vincensini et al. 2011)) or the actors of the intraflagellar transport (IFT) machinery, including motors (Pazour et al. 2000; Vincensini et al. 2011; Dentler et al. 2009) and particle components (Piperno & Mead 1997; Cole et al. 1998), reviewed in (Vincensini et al. 2011).

1.1.1 Cilia Classification

Cilia are classified according to their internal molecular arrangement and their ability to move (Supatto & Vermot 2011). Two cilia types can be defined: primary and motile cilia.

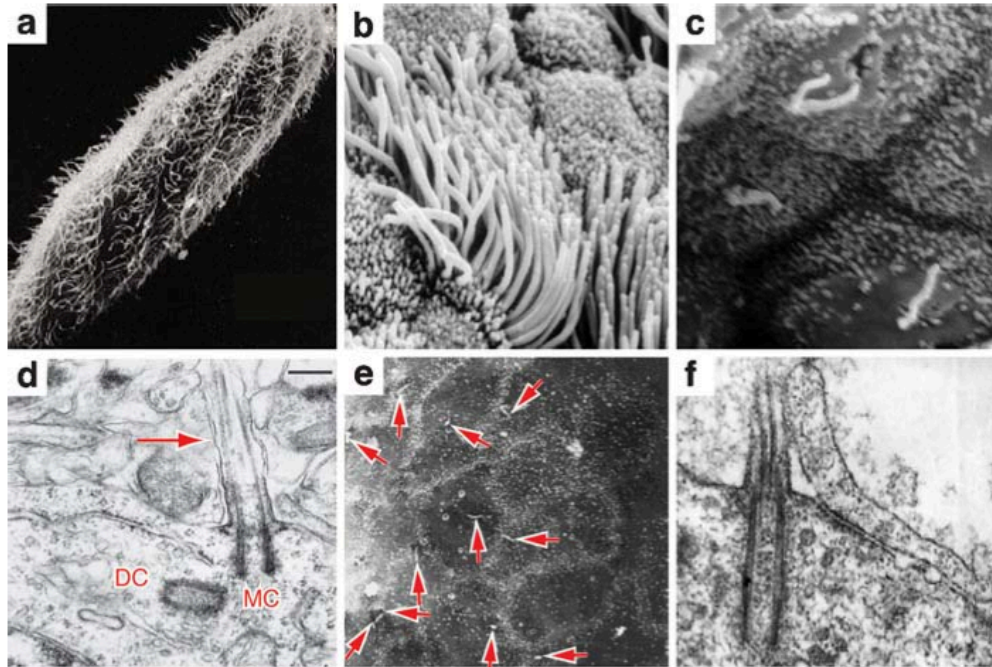


Figure 1.4 - Motile and primary cilia in diverse organisms and cell types. (a) The protozoan *Paramecium* is covered with motile cilia that enable it to swimming. (b) Motile cilia in the mammalian trachea. (c) Primary cilia in the renal tubules epithelia. (d) Electron micrograph of a mouse pyramidal neuron displaying a primary cilium. MC and DC denote the mother and daughter centrioles, respectively. (e) Primary cilia in the epithelial cells surrounding the lumen of pancreatic ducts. (f) Micrograph of a primary cilium emerging from a human odontoblast. Figure from (Badano et al. 2006).

The primary cilium is generally shorter and immotile, and is present as a solitary structure on most cells including epithelial cells, fibroblasts or neurons (Vincensini et al. 2011; Supatto & Vermot 2011). They are related with sensory and signalling functions. According to internal arrangement, primary cilia have a 9+0 axoneme (no central microtubule pair) and lack of dynein arms (Vincensini et al. 2011) - Figure 1.5b.

They were long thought to be vestigial, but were recently found to act as a complex signalling centre (Singla & Reiter 2006). Primary cilia participate in numerous biological processes ranging from chemo- and mechano-sensation to the transduction of an expanding list of signalling cascades that are essential to regulate cellular and tissue homeostasis (Vincensini et al. 2011; Singla & Reiter 2006). Their functional importance is highlighted by the growing list of diseases caused by defects at the level of the primary cilium.

In contrast, motile cilia are found by the hundreds at the surface of epithelial cells lining the ventricles of the brain, the respiratory tract and the oviduct, and they beat in a synchronized manner to direct fluid movement (Supatto & Vermot 2011; Vincensini et al. 2011). Most motile cilia possess a 9+2

structure (Figure 1.1 and 1.5a) and are involved in ciliary beating. A 9+2 structure means the axoneme of motile cilia is composed of nine peripheral doublet microtubules with attached outer and inner dynein arms (ODA and IDA, respectively) and radial spokes, surrounding a central complex (CC) with two central microtubules and the central sheath. ODAs and IDAs (axonemal dyneins^{*}) generate the force necessary for motility. The motor activity of dyneins is also regulated by several other components (Supatto & Vermot 2011; Theegarten & Ebsen 2011; Schwabe et al. 2008): (i) the radial spokes, which are T-shaped projections originating from each peripheral doublet and directed towards the central pair, (ii) the projections associated with the central pair, and (iii) the dynein regulatory complex, which is constituted by the nexin links. The basis for axonemal movement is the sliding of microtubules relative to one another (Supatto & Vermot 2011; Theegarten & Ebsen 2011; Schwabe et al. 2008). Dynein-generated forces that cause sliding between pairs of doublet microtubules produce axonemal bending for axonemal microtubules are anchored to the cell via the basal bodies, microtubule sliding causes the axoneme to bend (Supatto & Vermot 2011; Theegarten & Ebsen 2011; Schwabe et al. 2008).

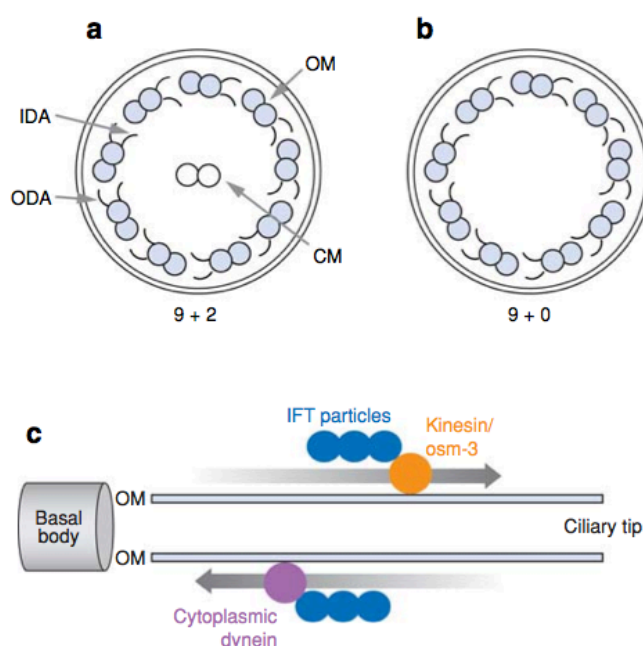


Figure 1.5 – Schematic representation of “9+2” and “9+0” axoneme cross sections and intraflagellar transport. (a, b) Simplified diagram of the ultrastructure of motile and primary cilia. The axoneme of (a) 9+2 cilia is composed of nine outer doublets of microtubules (OM) surrounding a central pair (CM), whereas in (b) 9+0 the latter is not present. Inner (IDA) and outer (ODA) dynein arms are responsible for generating force for movement and project from one outer doublet to the next. (c) Along the outer microtubule doublets (OM) and under the ciliary membrane, IFT particles are transported towards the ciliary tip (anterograde) by kinesin and back to the basal body and the cell (retrograde) by the molecular motor cytoplasmic dynein. Figure and legend from (Badano et al. 2006).

^{*} Axonemal dyneins are protein complexes composed of one to three dynein heavy chains and a variable number of intermediate and light chains. The dyneins heavy chains possess ATPase and motor activity, whereas the light and intermediate dyneins regulate their activity. These dyneins are specific of axonemes, not be confused with cytoplasmic dyneins.

1.2 Ciliopathies and laterality defects

Given the multiple functions of cilia in development, cilia defects cause multiple human diseases known as Ciliopathies (Marshall 2008; Fliegauf et al. 2007; Goetz & Anderson 2010), like polycystic kidney disease (PKD) and primary ciliary dyskinesia (PCD). The role of motile cilia in a number of physiological processes has been long recognized and thus the consequences of motile cilia dysfunction have four major manifestations in mammals: early embryonic death due to failure of embryonic turning; respiratory dysfunction; reproductive sterility; and hydrocephalus (Badano et al. 2006) (Figure 1.6). Ciliary dysfunctions involving motile cilia also result in body laterality defects (McGrath 2003), like *situs inversus* (Afzelius 1995).

Not all Ciliopathies are related to motile cilia. Some are based in defects occurred in primary cilia, like PKD (polycystic kidney disease), BBS (*Bardet-Biedl* syndrome), *Joubert* Syndrome, orofacial digital syndrome, *Alström* syndrome or *Meckel Gruber* syndrome (Fliegauf et al. 2007; Vincensini et al. 2011). The link between the primary cilium and genetic diseases was first established by the study of Pazour et al. (Pazour et al. 2000) who discovered that IFT88, a gene essential for IFT and flagellum construction in *Chlamydomonas reinhardtii* was mutated in a mouse model for PKD. This mouse model has been instrumental in the revelation of the essential role of the primary cilium in the development of several tissues in vertebrates (Pazour et al. 2000; Vincensini et al. 2011).

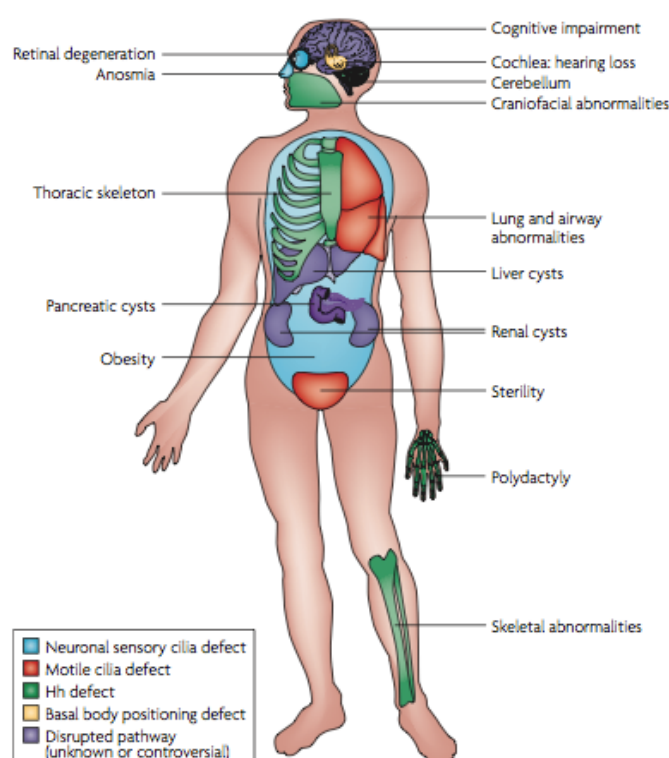


Figure 1.6 - Organs affected in human Ciliopathies. Numerous pleiotropic human disorders have been attributed to defects in cilia formation. Some aspects of these syndromes have been attributed to defective hedgehog (Hh) signalling. Other attributes of human disorders result from defective specialized cilia. Infertility observed in patients with ciliopathies is the result of defective sperm flagella and motile oviduct cilia. Adapted from (Goetz & Anderson 2010).

1.2.1 Primary ciliary dyskinesia

Primary ciliary dyskinesia (PCD) is a rare, usually inherited, autosomal disease with a recessive pattern. Estimation of prevalence is difficult and given between 1:10,000 to 40,000 live births (Afzelius 1995; Afzelius 2004; Theegarten & Ebsen 2011). Includes a group of diseases that present alterations in the motility of respiratory cilia. The coexistence of PCD and *situs inversus*[†] is called *Kartagener* syndrome and has a frequency between 40% and 50% among patients with PCD (Afzelius 1995).

Symptoms vary according to the age in which diagnosis is made, but commonly PCD is characterized by the presence of simultaneous chronic infections of the upper and lower respiratory tracts, including the middle ear, starting from the time of birth. Early diagnosis is very important because it is possible to institute a number of respiratory measures that help to prevent the irreversible lung damage (Ellerman & Bisgaard 1997). Diagnosis of PCD requires the presence of the characteristic clinical phenotype and either specific ultrastructural ciliary defects identified by TEM or/and by abnormal ciliary function (Bush et al. 2007; Theegarten & Ebsen 2011; Armengot et al. 2012).

Although PCD is a uniform clinical entity, studies conducted with electron microscopy have shown that there are different subgroups within it. Axonemal dynein absence affects 70%-80% of patients (Afzelius 2004; Jorissen et al. 1997). However, there are cases of patients with PCD and *situs inversus* (*Kartagener* syndrome) with a completely normal ciliary ultrastructure (Afzelius 2004; Theegarten & Ebsen 2011; Merveille et al. 2010). On the other hand, it has been observed that there may be ciliary abnormalities in the context of infection and inflammation (secondary ciliary dyskinesia). For these reasons, the diagnostic validity of the ultrastructural study is limited (Bush et al. 2007), and has been replaced by high-speed videomicroscopy (Armengot et al. 2012; Green et al. 1993). Normal cilia beat frequency (CBF) is about 11-18 Hz, and any mean frequency less than 10 Hz is considered abnormal (Green et al. 1993). According to Jackson et al. (Jackson et al. 2012) investigation, high-speed videomicroscopy for studying CBF and motility pattern have to be done under 37°C since different temperatures may increase the risk of PCD misdiagnosis. At present, guidelines and algorithms have been developed to standardize diagnostic procedures (Bush et al. 2007) in order to ameliorate the PCD diagnostics.

Studies carried out in the green alga *Chlamydomonas reinhardtii* established the link between cilia and several genetic diseases (Vincensini et al. 2011). Loss-of-function mutations in the human ortholog of *Chlamydomonas reinhardtii* ODA7 disrupt dynein arm assembly and cause PCD (reviewed in Vincensini et al. 2011).

[†] Mirror-image organ arrangement and other forms of heterotaxy are main symptoms.

1.3 Role of cilia in the left-right patterning

The establishment of left-right (L-R) asymmetries in vertebrates occurs during early stages of embryonic development through a complex process involving epigenetic and genetic mechanisms (Lopes et al. 2010). Three consecutive axes are established during early development; they are the dorsal-ventral, anterior-posterior and left-right axes (Figure 1.7) (Hirokawa et al. 2009).

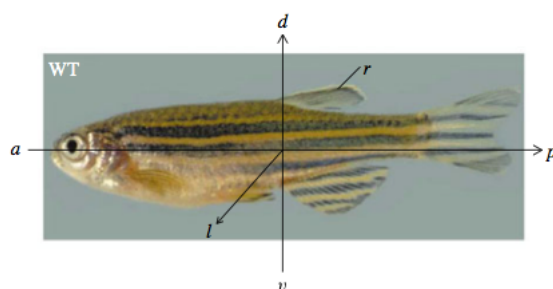


Figure 1.7 – Body plan and axes in zebrafish: anterior-posterior, dorsal-ventral, left-right.
Adapted from (A. A. Smith et al. 2012)

The embryonic node, also known as the L-R organizer of the vertebrate embryo, is a ciliated structure where motile cilia generate an important fluid-flow named 'Nodal flow'. The Nodal flow is thought to generate the first cues to establish the L-R axis of symmetry (Nonaka et al. 1998), either a chemical or/and a mechanosensory signalling pathway that will culminate with correct positioning of internal organs. Sometimes this process fails and gives rise to laterality defects or heterotaxy (Nonaka et al. 1998; McGrath 2003) like in *Kartagener syndrome*.

1.3.1 The two left-right models

The mechanism by which L-R is transferred to the LPM remains a major unanswered question in L-R patterning (Hamada 2008; Marshall & Nonaka 2006). There are two prevailing models: one arguing that a morphogen becomes concentrated on the left side of the node in response to flow - 'morphogen model' (Okada et al. 2005; Nonaka et al. 1998; Tanaka et al. 2005) (Figure 1.8A); and other suggesting that 'two different cilia types' in the node perform different functions (McGrath et al. 2003; Tabin & Vogan 2003) (Figure 1.8B).

During the development of L-R theories, Tanaka and colleagues (Tanaka et al. 2005) argued that lipid-bound vesicles containing morphogens are carried leftwards, breaking on the left side of the node and thereby releasing their cargoes asymmetrically. This study showed that fibroblast growth factor (FGF) signaling triggers the secretion of little membrane-vesicles (0.3–5 μm) termed 'nodal vesicular parcels' (NVPs), that carry Sonic hedgehog (Shh) and retinoic acid (RA) inside the mouse node (Tanaka et al. 2005). Based on Tanaka's findings, Cartwright and colleagues (Cartwright et al. 2006) modeled the movement of NVPs across the mouse node and demonstrated that the flow should indeed cause them to accumulate on the left side of the node, as required for symmetry breaking. However, based on the biophysical properties of node such as high viscosity, they argued

that the morphogens can not be delivered to the surrounding cells by their mechanical rupture either by the cilia or the flow. They postulate that if there is rupture it must be induced by a biochemical mechanism not yet discovered (Cartwright et al. 2006). Both studies contributed for the 'morphogen model'.

The second model is called 'two-cilia model' and is based on the discovery that in the embryonic mouse node, there are motile cilia, identifiable with left-right dynein (*Lrd*) (McGrath et al. 2003). In addition, a population of non-motile cilia was reported and suggested to be capable of sensing the mechanical stress of the stronger leftward flow (mechanosensory cilia) (McGrath et al. 2003; Tabin & Vogan 2003). It has been proposed that the mechanosensory cilia trigger a left-sided calcium signal through the action of *polycystic kidney disease 2* (*Pkd2*) channels localized on their axonemes. *Pkd2* is known to form a functional calcium channel that is thought to sense the bending of primary cilia induced by urine flow in the renal tubule, thus functioning as a mechanosensor (Nauli et al. 2003). *Polycystic kidney disease 1 - like 1* (*Pkd1l1*) is the functional partner of *Pkd2* in L-R patterning being conserved between medaka and mouse (Field et al. 2011). *Pkd1l1*-*Pkd2* colocalize on motile cilia in the medaka KV where all cilia are thought to be motile (Kamura et al. 2011).

Currently, a new idea in the field is emerging: all cilia (motile and immotile) may have sensory functions. Motile cilia of the mammalian respiratory epithelium have been reported to exhibit both mechanosensitivity and chemosensitivity (Bloodgood 2010). The mucociliary clearance in the airways is a known example of mechanosensation where rises in viscosity are sensed by the motile cilia that lead to an increase in cytosolic calcium which in turn is associated with increased CBF to accelerate mucus clearance (reviewed in Bloodgood 2010). Recently, it was reported an unexpected demonstration of chemoreception by the localization of different members of the bitter taste-receptor family to motile cilia of airway epithelial cells (Shah et al. 2009). Indeed, bitter compounds induce a rise in intracellular-calcium concentration in ciliated cells as well as an increase in CBF (Shah et al. 2009).

To date, both LR models are equally plausible because the molecular sensors of nodal flow are still unknown.

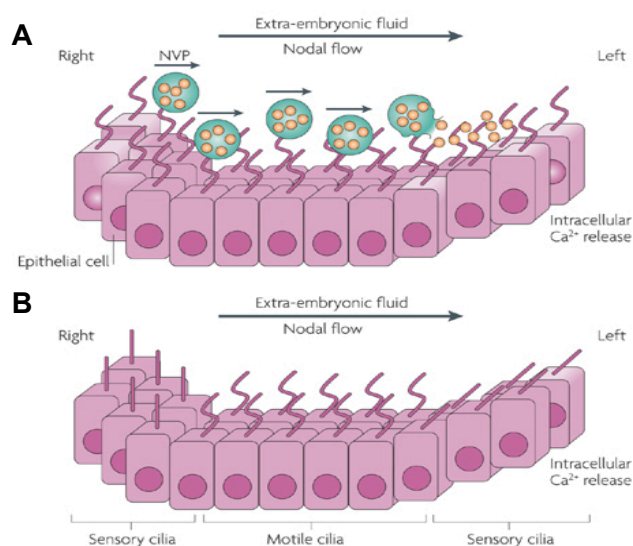


Figure 1.8 – Schematic representation of the two L-R models. (A) 'morphogen model' - NVPs appear to be released from dynamic microvilli, transported to the left side by the nodal flow, and fragmented with the aid of cilia at the left periphery of the node. (B) 'two cilia model' - non-motile cilia are capable of sensing the mechanical stress of the leftward flow generated by motile cilia. Adapted from Tanaka et al. 2005) and (Tabin & Vogan 2003).

1.3.2 Left-right signaling cascade

The establishment of L-R patterning comprises three key steps (Shiratori & Hamada 2006): (i) the first step is the symmetry-breaking event in the embryonic node, a leftward extracellular fluid flow that is generated by the rotational movement of monocilia; (ii) the second step is the transduction of this asymmetric information to the left LPM, where genes such as *Nodal* are asymmetrically expressed. However, the mechanism that produces asymmetrical expression of *Nodal* and *Cerl2* on the left and right sides of the mouse node, and its potential link to the leftward nodal flow, is not fully understood (Lopes et al. 2010); (iii) in the third step, these asymmetric signals drive the morphogenesis of various asymmetric visceral organs (Shiratori & Hamada 2006).

Ciliary motility and the resulting nodal flow have also been shown to be required for L-R axis formation at the posterior notochord in rabbit, the gastrocoel roof plate in *Xenopus laevis*, and in Kupffer's vesicle in zebrafish and medaka fish, finally resulting in the asymmetrical activation of the Nodal signaling cascade in the left LPM (Okada et al. 2005; Essner 2005; Hojo et al. 2007; Schweickert et al. 2007).

To date, the relationship between the fluid flow inside KV and the asymmetric function of *charon* in medaka (Hojo et al. 2007) and zebrafish (Lopes et al. 2010), and its homologue *coco* in *Xenopus* have been studied (Schweickert et al. 2007).

In summary, nodal flow is highly conserved and is important for L-R patterning in mouse, *Xenopus* and fish.

1.4 Embryonic Left-Right organizers

1.4.1 Mouse node

Several studies indicate that the mouse node plays an important role in the establishment of L-R asymmetry (Nonaka et al. 1998; Okada et al. 2005), and that is the reason why this organ is also called mouse L-R organizer. The mouse node (Figure 1.9) is found at the rostral end of the primitive streak. It consists dorsally of epiblast and ventrally of the most caudal aspect of the notochordal plate (Brennan et al. 2002). The node gives rise to midline structures such as the notochord and floor plate that act as a midline barrier necessary for maintaining correct laterality (reviewed in Brennan et al. 2002).

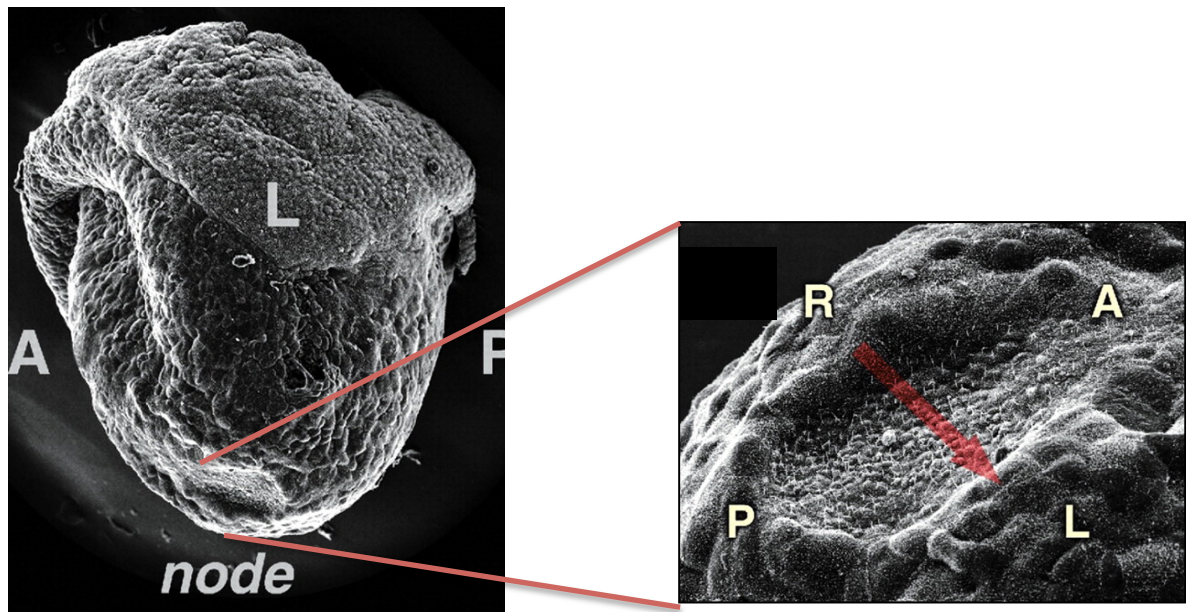


Figure 1.9 – Scanning Electron micrographs of a mouse node. Low-magnification view of a mouse embryo at 7.5 days post-coitum. Reichert's membrane was removed. Higher-magnification view of the mouse node, where is visible nodal cilia and nodal pit cells. Adapted from (Okada et al. 2005).

Ultrastructural studies have shown that monocilia present on cells of the exposed ventral surface of the node generate a net leftward flow of extra-embryonic fluid known as the nodal flow (Sulik et al. 1994; Nonaka et al. 1998), as a result of a clockwise rotation of polarized, posteriorly tilted cilia (Shiratori & Hamada 2006; Nonaka et al. 2005) (Figure 1.10 and 1.11). These motile cilia bend like ropes being whirled in circles (Cartwright et al. 2006). In mouse, posterior tilting of cilia occur passively, since the apical surface of ventral node cells has a convex curvature and, because cilia localize to the posterior side of the plasma membrane, this results in a tilt (reviewed in Brennan et al. 2002).

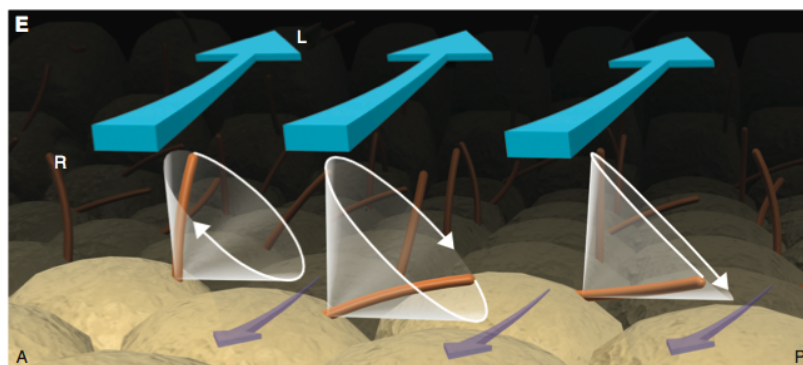


Figure 1.10 - Model of the generation of nodal flow. The orientation is indicated as anterior (A), posterior (P), left (L), and right (R). The conic rotation of the nodal cilia is posteriorly tilted. Therefore, the cilia move in a nearly perpendicular manner from right to left. The return movement from left to right occurs just above the cell surface. The viscous drag thus dumps the movement of the fluid to the right (purple). As a result, unidirectional leftward flow (blue) is generated. Adapted from (Hirokawa et al. 2009).

The precise structure of the motile cilia in the mouse node is still a point of discussion. Motile cilia, such as those of the human respiratory tract or oviduct, generally have a 9+2 configuration in the ciliary axoneme (Figure 1.1 and 1.5a). In contrast, mouse node cilia generally have a 9+0 microtubule arrangement, i.e., they are devoid of central microtubule pair, and thus usually thought to be immotile (Figure 1.5b), which is clearly not the case. Transmission EM of node cilia showed a 9+0 configuration (Sulik et al. 1994; Essner 2005).

At present it is thought that 9+0 node cilia are motile and produce a vortical motion in which the cilium maintains a straight extended orientation but the distal end moves in a circle around the axis of rotation - in contrast to the whip-like back – and – forth motion characteristic of 9+2 cilia (Nonaka et al. 1998). However, two recent studies have identified 9+2 cilia in the mouse node (Figure 1.12), perhaps due to improved fixation conditions (Caspary et al. 2007). Thus, additional studies are needed to define the structure and spatial organization of motile cilia in mouse node.

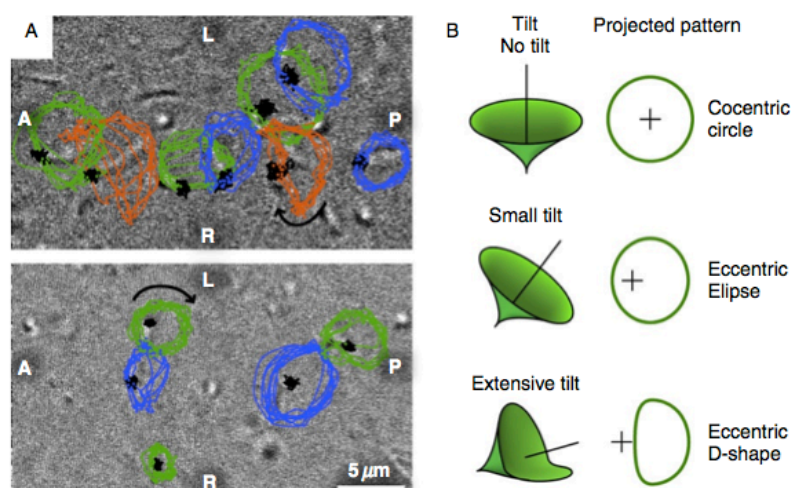


Figure 1.11 – Trajectory of Node Cilia Movement. (A) Trace of node cilia in enhanced DIC images after background subtraction. Positions of root are indicated in black, and tip in blue, green, and orange. Most cilia have a pattern consistent with the projection of a tilted cone (blue and green) whereas some cilia move in a D-shape (orange). A, P, L, and R refer to anterior, posterior, left, and right sides of the node, respectively. The direction of cilia rotation was clockwise (arrows); (B) Relationship between essentially rotatory movement of cilia and their projected images at various tilt angles.

Adapted from (Nonaka et al. 2005)

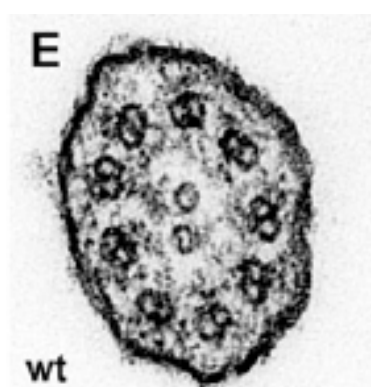


Figure 1.12 – Cilium in wild-type mouse node. Transmission Electron Microscopy (TEM) analysis of cilia from embryonic node of e8.0 wild-type embryos. A central pair is visible, revealing that mouse node cilia could have a 9+2 configuration. Adapted from (Caspary et al. 2007).

Several transcription factors are required for the formation of normal node cilia, like *Foxj1* that is specifically required for the formation of motile cilia in many tissues, and *Rfx3* which acts as transcription factor that binds to X-box motifs present in the regulatory regions of many ciliary genes (Lee & Anderson 2008). In the absence of murine *Foxj1*, cilia of normal length are present on the node but appear to be immotile, and *situs* is randomized as a result (Chen et al. 1998; Brody et al. 2000; M. M. Zhang et al. 2004). *Rfx3* mutants form nodal cilia but they grow slowly and are shorter than the wild-type cilia at the two-somite stage (when nodal flow is required) (Bonnafe et al. 2004). *Rfx3* mutants show randomized L-R situs, suggesting that cilia must have a specific length to generate effective nodal flow (Bonnafe et al. 2004).

1.4.2 Zebrafish Kupffer's vesicle

Kupffer's vesicle (KV) is the equivalent to the mouse node ciliated organ of asymmetry in the zebrafish embryo that initiates L-R development of the brain, heart and gut (Essner 2005). First described in 1868 by *Kupffer*, KV is a conserved structure among teleost fishes, like *Fundulus heteroclitus* (Brummett & Dumont 1978). In zebrafish, KV is formed from a group of approximately two-dozen cells, known as dorsal forerunner cells (DFCs[‡]) that migrate at the leading edge of the embryonic shield (the zebrafish equivalent of the mouse node that gives rise to the notochord and floorplate) during gastrulation. At the end of gastrulation, DFCs migrate deep into the embryo and organize to form KV (reviewed in (Essner 2005)). During subsequent somite stages, KV constitute a small but distinctive epithelial closed vesicle containing fluid, located mid-ventrally posterior to the yolk cell or its extension, and transiently present during most of the segmentation period (Kimmel et al. 1995; Kramer-Zucker 2005).

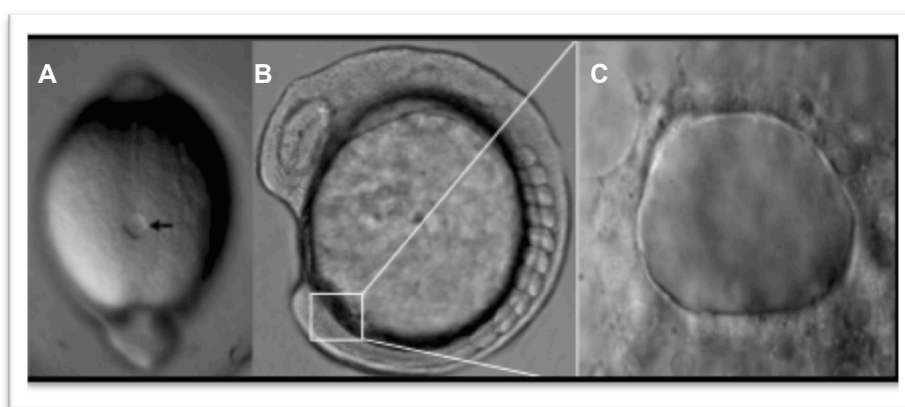


Figure 1.13 – DIC images of the zebrafish KV. (A and C) KV dorsal view in a 10th somite zebrafish embryo; (B) KV lateral view in a 10th somite zebrafish embryo.

[‡] In contrast to other cells in this region, DFCs do not involute during gastrulation, but remain at the leading edge of epibolic movements.

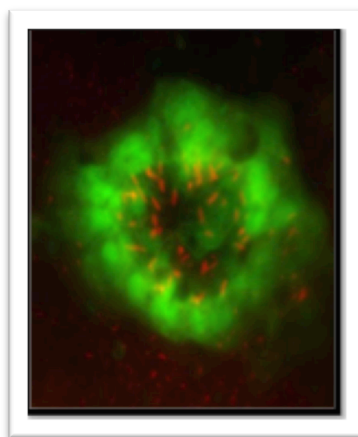


Figure 1.14 – Immunofluorescence experiment for visualizing KV cilia. Imaging experiment using a sox17:GFP transgenic zebrafish line, showing KV monocilia labelled with an antibody anti- acetylated alpha-tubulin (in red).

The epithelium of the KV is made of 9+2 (Ferrante et al. 2009; Kramer-Zucker 2005; Kreiling et al. 2007) monociliated cells (Figure 1.14) that generate a counterclockwise fluid flow. This flow triggers asymmetric calcium response on the left side of the cavity (Francescatto et al. 2010; Sarmah et al. 2007) and is involved in establishing and maintaining the L-R asymmetry of the body axis (Essner 2005; Kramer-Zucker 2005) as described in this Chapter. Even though, the presence of sensory immotile cilia is still a matter of debate in the fish (Borovina et al. 2010; Okabe et al. 2008).

Currently, it is assumed that KV is analogous to the mouse node in terms of L-R patterning (Essner 2005). While the ciliated surface of the mouse node is relatively flat, KV is a hollow sphere containing cilia, projecting both from dorsal roof and ventral floor (Kreiling et al. 2007; Amack et al. 2007). Kramer-Zucker et al. (Kramer-Zucker 2005) reported that cilia rotate counterclockwise when viewed from the apical side in the KV, which is opposite to what is observed in the mouse node. Kreiling et al. (Kreiling et al. 2007) found by 3D images analysis that cilia are concentrated in the dorsal-anterior region of the vesicle, suggesting that these cilia cause the dominant counterclockwise flow in KV (Figure 1.15). Okabe et al. (Okabe et al. 2008) hypothesized that the net flow in zebrafish KV is analogous to flow in the mouse node and medaka fish in terms of L-R patterning even though the ciliated cell structures appear to differ in architecture. Furthermore, Okabe et al. (Okabe et al. 2008) SEM and video microscopy studies demonstrate that numerous cilia within the vesicle are tilted to the posterior direction. Although the posterior tilt of the cilia in the mouse node is thought to be due to a shift of the base of the cilia to the posterior, the same can not be confirmed in KV (Okabe et al. 2008). It is more likely that the combination of cilia bending and cell orientation of KV causes cilia to be pointed towards the posterior (Okabe et al. 2008).

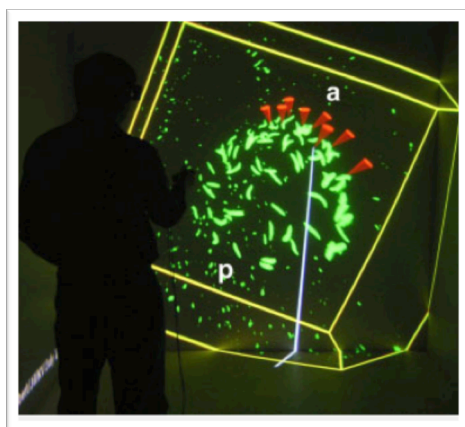


Figure 1.15 – Typical three-dimensional (3-D) reconstructions of confocal data sets of KV cilia at the 9th somite stage projected in the Cave. Distribution of KV cilia (green); anterior (a) is on top, posterior (p) is on the bottom. Some of the anterior cilia have been marked (red cones). The asymmetric distribution of cilia can be seen as a clustering of cilia on the anterior surface of KV. Adapted from (Kreiling et al. 2007).

Some differences were found between mouse node and KV from medaka and zebrafish (Figure 1.16). According to Kamura et al. (Kamura et al. 2011), all medaka KV cilia are motile, whereas in the mouse node McGrath et al. (McGrath et al. 2003) showed the presence of two populations of cilia, one motile and other immotile. Furthermore, Caspary et al. (Caspary et al. 2007) showed cilia from the mouse node with central pair, adding the presence of another type of cilia to the granted hypothesis of the 9+0 cilia (Nonaka et al. 2005) (as described previously – Figure 1.12). In zebrafish, immotile and motile cilia were seen in the KV, although is still a matter of debate (Borovina et al. 2010; Okabe et al. 2008).

However, the fluid dynamics inside KV is not completely understood and several groups are trying to figure it out (Supatto & Vermot 2011; Kreiling et al. 2007; Okabe et al. 2008; A. A. Smith et al. 2012; Cartwright et al. 2008). The diversity of cilia motility and fluid mechanics in the embryo is starting to be studied in vivo (Supatto & Vermot 2011). The number of flows that can be generated by such simple structure is limited, but the combination of cilia beating pattern and particular topology of the environment can participate to build up complex flows.

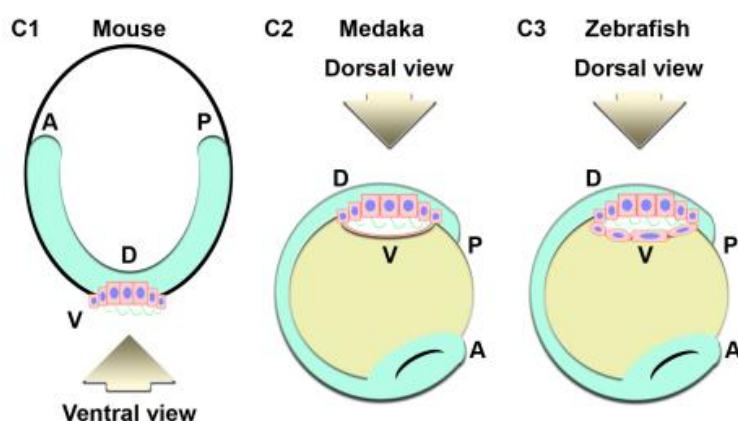


Figure 1.16 – Mouse, medaka and zebrafish left-right organizers: (C1) in the mouse node, ciliated cells are located on the ventral side of the embryo, and thus the cilia project to the outside (Vogan & Tabin 1999). This planar structure of ciliated tissue is analogous to that of fish like medaka, which have only one epithelial layer on the dorsal roof (Okada et al. 2005; Hojo et al. 2007)(C2). Zebrafish KV (C3) is composed of two layers of cells having the cilia both at the dorsal roof and the ventral floor (Amack et al. 2007; Kreiling et al. 2007). Adapted from (Okabe et al. 2008).

1.5 Motile cilia generated flow in zebrafish

1.5.1 Motile cilia beat pattern

A key parameter dictating cilia-mediated hydrodynamics is the type of beat they generate (Figure 1.18). The beat pattern seems related with the internal organization of the cilia but many unresolved questions remain concerning the correlation of structure and cilia beat in different developing organs.

The motility depends on the presence of dynein arms that are attached to the microtubules, the dynein regulatory complex (DRC) and on the presence of radial spokes (reviewed in Vincensini et al. 2011). Vertebrates 9+2 cilia can significantly bend during its motion with effective and recovery strokes, while 9+0 cilia have an almost perfect circular motion (Nonaka et al. 1998; Nonaka et al. 2005). In protists, the presence of the central pair of microtubules is critical in shaping the overall tridimensional motion of the beating cilium. The so-called central pair hypothesis constitutes an attractive view of the structural basis of cilia beat[§] (Castleman et al. 2009). In humans and zebrafish, mutants for the radial spoke heads affect cilia motion (Castleman et al. 2009) and the DRC is critical for proper cilia motility in zebrafish (Colantonio et al. 2009).

In terms of motility, little is known about potential factors that could control the direction and frequency of beating cilia in the zebrafish embryo. The relationship between the beat pattern and the directional flow will be discussed further in this section.

1.5.2 Motile Cilia Beat Frequency

In cases of Ciliopathies such as PCD, cilia beat frequency (CBF) is an important feature for the definitive diagnose (Armengot et al. 2012; Shoemark et al. 2012; Jackson et al. 2012). Cilia from nasal brushings and biopsy material are screened using high-speed videomicroscopy, as a way of studying CBF (Armengot et al. 2012; Shoemark et al. 2012; Jackson et al. 2012). CBF values under 10 Hz are considered abnormal (Green et al. 1993).

Several studies have been done in order to better characterize the CBF of ciliated organs in distinct animal organisms (Table 1.1). Some methodologies and techniques used for human CBF analysis were originated and validated in animal *in vivo* studies. Nevertheless, CBF should be even more characterized in model organisms, especially when related with L-R problems (Kunimoto et al. 2012; Lechtreck et al. 2008; Norris & Grimes 2012; Lucas et al. 2011).

[§] The primary role of the associated dynein motors of the nine outer doublet microtubules power the microtubule sliding that ultimately results in flagellar bending whereas the central pair acts as a coordinator of the doublet sliding through the radial spokes and the DRC.

Table 1.1 – Cilia properties in various embryonic models. Zebrafish, mouse, medaka and *Xenopus* are used as ciliated models. Cilia ultrastructure, CBF, length and rotation direction, among other ciliary characteristics are reviewed in this table, for distinct organs. Figure from (Supatto & Vermot 2011).

Species	Organ	Structure	Mono- or multiciliated cells	Frequency (Hz)	Length (μm)	Rotation direction (view from the cilium tip)	θ (deg)	ψ (deg)	Directional flow velocity ($\mu\text{m s}^{-1}$)
Zebrafish	Left-right organizer (Kupffer's vesicle)	9 + 2 ^a	Mono ^a	29.7 \pm 0.3 ^b	3.3 \pm 1.1 ^a	Clockwise ^{b,d,e}	30 ^f		10–50 ^f
	Inner ear	9 + 2	Mono ^d	26.2 \pm 1.6 ^a	3.7 \pm 0.8 ^a	Counterclockwise ^a			
		9 + 0		34 \pm 6 ^d	5.9 \pm 0.2 ^d			\sim 90 ^h	\sim 10–50 ^h
	Central canal spinal cord	(this study)							
		9 + 0 ^a	Mono ^a	12.3 \pm 3.4 ^a	2.1 \pm 0.7 ^a				0.45 \pm 0.03 ^a
Mouse	Pronephric ducts	9 + 2 ^a	Mono and multi ^a	20.0 \pm 3.2 ^a	8.8 \pm 2 ^a	Clockwise ^a			
	Left-right organizer (node)	9 + 0 ^d	Mono ^d	10.7 \pm 2.8 ⁱ	5.5 ⁱ	Clockwise ⁱ	35–40 ⁱ	40–50 ⁱ	4 (leftward) ⁱ – 2 (rightward) ⁱ 50 ^j
	Brain ventricles		Multi ^k	12–17 ^k	8–10 ^k	Wave pattern ^k			
Medaka	Left-right organizer (Kupffer's vesicle)	9 + 2 ^j	Mono ⁱ	42.7 \pm 2.6 ⁱ	5 ⁱ	Clockwise ⁱ	35–40 ⁱ	40–50 ⁱ	7.4 \pm 3.6 ⁱ
Xenopus	Gastrocoel roof plate			20–25 ^m	3–5 ^m	Clockwise ^m			3.5 (leftward) ^m

^a Kramer-Zucker et al. (2005).
^b Okabe et al. (2008).
^c Lopes et al. (2010).
^d Nonaka et al. (1998).
^e Okada et al. (1999).
^f Supatto et al. (2008).
^g Colantoni et al. (2009).
^h Wu et al. (2011).
ⁱ Okada et al. (2005).
^j Nonaka et al. (2002).
^k Hirota et al. (2010).
^l Kobayashi et al. (2010).
^m Schweickert et al. (2007).

1.5.3 Fluid hydrodynamics

Essentially, the main function of motile cilia is to generate fluid flow at the micrometer scale. However, fluid dynamics are governed by laws that are not trivial at this scale and the resulting fluid flow presents features that are not intuitive when used to human scale (Supatto & Vermot 2011).

In fluid mechanics, the *Reynolds* number (Re) is a dimensionless number that characterizes the nature of a fluid flow and the relative contribution of inertia and viscous dissipation. The cilia-driven flow involved in zebrafish development exhibits characteristic scales, $L < 100\mu\text{m}$ and $U < 100 \mu\text{m s}^{-1}$ (L = length; U = typical velocity) (Supatto & Vermot 2011). Using the kinetic viscosity of water ($\nu \approx 10^6 \mu\text{m}^2 \text{s}^{-1}$), the resulting Re is $< 10^{-2}$. The flow generated by beating cilia is characterized by a low Re (Re $\ll 1$) environment^{**}, and it is governed by *Stokes* equations - being referred as 'creeping flow' or 'Stokes flow' (Supatto & Vermot 2011).

From a modeling perspective, the low value of the Re enables the simplification of the *Navier–Stokes* flow equation, the general model governing fluid dynamics (Supatto & Vermot 2011). If Re $\ll 1$, the inertial forces can be neglected compared to the viscous forces and the unresolved *Navier–Stokes* flow equation can be approximated by the linear Stokes flow equation (Figure 1.17). This equation is the starting point of any modeling of cilia-driven flows (Cartwright et al. 2006; D. J. Smith et al. 2008; D. J. Smith et al. 2010; A. A. Smith et al. 2012; Supatto et al. 2008). Thus, the flow generated by an ensemble of cilia can be approximated as the sum of the flow induced by each single cilium. In addition, the linearity and the time reversibility of 'Stokes flow' equation provides fundamental properties of the flow that can be generated by motile cilia (Supatto & Vermot 2011).

^{**} At the human scale, a swimmer ($L \approx 1\text{m}$ and $U \approx 1\text{ms}^{-1}$) should swim in a fluid that is 10^8 times more viscous than water to experience such fluid behavior.

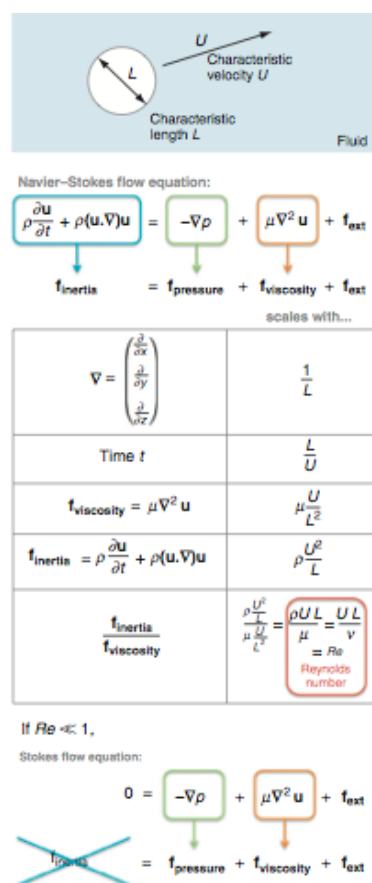


Figure 1.17 - Fluid dynamics at low Reynolds number. The velocity field \mathbf{u} of a fluid can be generally described by the *Navier–Stokes* flow equation. Each term of this equation scales as a force per unit volume: $\mathbf{f}_{\text{inertia}}$ includes the time-dependent and the nonlinear inertial components (blue), $\mathbf{f}_{\text{pressure}}$ is the force generated by a pressure gradient (green), $\mathbf{f}_{\text{viscosity}}$ is the viscous dissipation term (orange), and \mathbf{f}_{ext} corresponds to external forces applied to the liquid (such as force generated by a motile cilium). The Reynolds number (Re) compares $\mathbf{f}_{\text{inertia}}$ with $\mathbf{f}_{\text{viscosity}}$ to check if one of these terms can be neglected in the *Navier–Stokes* equation. $\text{Re} \ll 1$ means that viscous forces dominate inertia. In this case, the inertial term can be neglected to obtain the ‘Stokes flow’ equation. Figure and legend from (Supatto & Vermot 2011).

1.5.4 Directional flow

Once cilia beat in their fluidic environment, how can they generate a directional flow? Based on ‘Stokes flow’ equation, the first challenge to the generation of a directional flow is the difficulty to obtain a net flow (Supatto & Vermot 2011). The absence of inertia results in a velocity that is proportional to the force applied to the fluid^{††} (Supatto & Vermot 2011; A. A. Smith et al. 2012). Time reversibility of the ‘Stokes flow’ equation means that the time asymmetry is not sufficient to create a net flow (reversing time does not affect the equation), as described by (Supatto & Vermot 2011; A. A. Smith et al. 2012). According to both studies (Supatto & Vermot 2011; A. A. Smith et al. 2012), in order to produce a directional flow at low Re, a beating cilium needs an asymmetry in space or shape.

Models predict that a directional flow cannot be produced by either a stiff cilium rotating in free space (Buceta et al. 2005) or a distribution of cilia arranged on a spatially asymmetric pattern (Cartwright et al. 2006), as reviewed in (Supatto & Vermot 2011). Presumably due to the cilia ultrastructure, length, and/or orientation, three types of spatially asymmetric cilia beating patterns have been proposed theoretically and observed experimentally in different organs of developing embryos (Figure 1.18): the ‘corkscrew-like motion’, the ‘asymmetric bending’, and the ‘tilted conical’ motion (Supatto & Vermot 2011).

^{††} In other words, it means that if a cilium stops beating and applying a force on the surrounding fluid, the flow velocity drops instantaneously (Supatto & Vermot 2011; A. A. Smith et al. 2012).

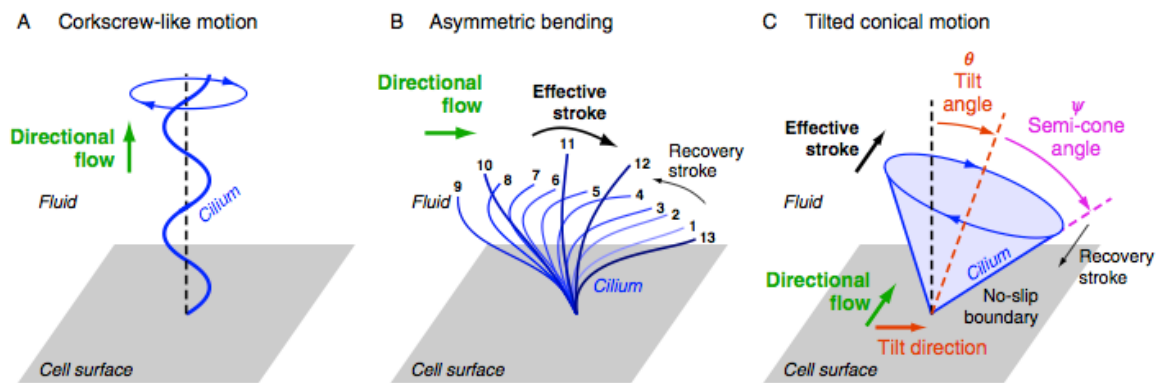


Figure 1.18 - Pumping flow with motile cilia at low Reynolds numbers: three types of spatially asymmetric beating patterns observed experimentally: (A) helical motion or corkscrew-like motion which pump fluids along the cilium, (B) asymmetric motion which is related to an asymmetric bending of the cilium during its movement, (C) cylindrical rotation with a tilted cilium. In (B) and (C), the effective stroke corresponds to the cilium momentum where fluid is moved efficiently in the direction of motion, whereas poor transport occurs during the cilia recovery phase (Supatto & Vermot 2011).

The ‘corkscrew-like motion’ (Figure 1.18A) is well known and is used by flagella to propel bacteria, but is not common in cell epithelium. Nevertheless, such cilia motion pattern has been observed during zebrafish kidney development (Kramer-Zucker 2005). In the ‘corkscrew-like motion’, the direction of the net flow generated is parallel to the rotation axis of the cilium, and it depends on the rotation direction and the helix orientation (Supatto & Vermot 2011).

In the ‘asymmetric bending’ (Figure 1.18B), the cilium changes its shape while rotating. During one beating cycle, its bending is not the same on one way compared to the other, producing an effective and a recovery stroke (Supatto & Vermot 2011). The flow direction is perpendicular to the rotation axis of the cilium and depends on the bending asymmetry. Flow direction does not directly depend on the cilium direction of rotation, but on the orientation of the effective strokes (Supatto & Vermot 2011). Such beating pattern has been observed in the left–right organizer in xenopus (Schweickert et al., 2007).

At last, the ‘Tilted conical’ motion (Figure 1.18C) is characterized by having a directional flow generated by cilia that exhibits a symmetrical circular motion without asymmetric shape as in the two previous cases. This type of cilia motion has been observed experimentally in mouse, rabbit, and fish L-R organizer (Okada et al. 2005). Recent models proposed that the spatial symmetry can be broken without the bending of the cilium. In this case, the cilium interaction with the cell surface plays a critical role (Cartwright et al. 2006; D. J. Smith et al. 2008; D. J. Smith et al. 2010; A. A. Smith et al. 2012; Vilfan et al. 2012): if the velocity of the fluid at the cell surface match the velocity of the surface itself (no-slip boundary condition (Supatto & Vermot 2011)), the rotation forms an effective stroke when the cilium is far from the surface, and a recovery stroke when it is close to the surface. Thus, the direction of the net flow generated depends on the cilium tilt and on the cell surface, and must be

perpendicular to the direction of the cilium tilt and parallel to the surface. The model predictions of a cilium tilt have been experimentally confirmed *in vivo* in mouse (Okada et al. 2005) (Figure 1.10) and in zebrafish (Supatto et al. 2008). Interestingly, among the three asymmetric beating patterns generated by biological cilia, the tilted conical motion is the easiest to reproduce artificially as it does not require controlling the bending of the cilium. For this reason, the generation of directional flow at low Re in microfluidic devices can be obtained using stiff artificial cilia beating with tilted conical motion (Nonaka et al. 2005; Vilfan et al. 2012).

Among the asymmetric cilia beating patterns, it is interesting to mention that only the ‘tilted conical’ motion allows breaking the L-R symmetry without preexisting L-R asymmetry at the scale of the cilium (Supatto & Vermot 2011). This pattern allows translating an anterior–posterior or dorsal–ventral asymmetry into a L-R asymmetry (Supatto & Vermot 2011). This would not be true for ‘corkscrew-like’ motion or ‘asymmetric bending’: a net flow in the L-R direction would require having a preexisting L-R asymmetry at the level of the cilium (Supatto & Vermot 2011).

1.5.5 Interplay between models and experiments

Efforts have been made to address the hydrodynamics involved in the L-R symmetry breaking during early vertebrate development. Through the modeling of the leftward directional flow in the L-R organizer, some key predictions have been explored.

In recent years, several models and simulations have been developed based on mouse node experimental data (section 5.1 of this Chapter). In these theoretical studies, the cilium is modeled either as an infinitesimal sphere rotating in its place (Cartwright et al. 2006), a small sphere moving on a fixed trajectory in the vicinity of a planar surface (Vilfan et al. 2012) or a slender body (D. J. Smith et al. 2008). Whatever the complexity of the model used, they are a great advantage to understand how biological processes occur, by explaining new observations, raising specific predictions, and suggesting the next set of experiments.

How the spatial asymmetry allows the generation of a directional flow within the L-R organizer was the first question that theorists wanted to address. The proposition that cilia were beating with a tilted conical motion^{††} was first suggested by Cartwright et al. (Cartwright et al. 2006) and further investigated by demonstrating the importance of the cell surface and the no-slip boundary condition to obtain efficient and recovery strokes (D. J. Smith et al. 2008; Vilfan et al. 2012). It is noted that the beating pattern of KV’s cilia is different from the mouse nodal cilia since they do not share the same ultrastructure. More sophisticated models are now taking into account the geometry of the L-R organizer and the spatial distribution and the density of cilia in mice. Kreiling et al. (Kreiling et al.

^{††} The posterior tilt of cilia has been first observed in mouse (Okada et al. 2005). This topology promotes a directional flow toward the left direction with cilia rotating clockwise (Figure 1.10). In zebrafish, the flow circulating around the dorsal–ventral axis within the KV cannot be due to a posterior tilt, but due to a dorsal tilt (Supatto & Vermot 2011), already observed *in vivo* (Supatto et al. 2008). Nevertheless, posterior tilting have been observed in the dorsal roof of the KV (Kramer-Zucker 2005; Okabe et al. 2008). Such topology cannot produce the observed flow around the dorsal–ventral axis (Supatto & Vermot 2011).

2007) showed that 80% of the cilia are located on the dorsal side of KV, revealing that the structure of KV could be more similar to the ventral node in mouse embryos than previously believed.

While many features are common between mice and fish, each species remain distinct and might have developed different ways to break the embryonic symmetry using the same basic ciliary machinery (Supatto & Vermot 2011). Thus, it is crucial to improve the characterization of the L-R organizers, especially the differences between the different animal organisms, in order to establish more accurate L-R theoretical models.

1.6 Project goals

The main goal of this Master project was the characterization of cilia motility through the study of cilia beat frequencies (CBFs) in the Kupffer's vesicle (KV) of zebrafish embryos. It was our objective to understand how could potential changes in CBFs impact on KV fluid flow, important for the establishment of the left-right axis of asymmetry.

The first part of the project consisted in studying CBF in the Kupffer's vesicle monociliated cells using spectral analysis. It was our objective to film KV cilia, using high-speed videomicroscopy, and apply a designed script, that allowed the extraction and decomposition of CBF results from the movies. The second part of this project was to study the cilia-generated fluid flow inside the zebrafish KV by tracking native particles and calculating their velocity in a non-invasive assay. Through the study of CBF and KV fluid flow mean velocity, we aimed to investigate if there were different populations of cilia based on CBF criteria and to classify the range of fluid flow velocities operating in this organ.

A tissue-specific screen previously done in our lab was the foundation for the third part of my Master project. With this screen we found several differential expressed genes in *deltaD*^{-/-} mutants, compared to wild-type embryos. Having identified some motile cilia-related genes, we proposed a validation study of gene expression using quantitative real time polymerase chain reaction (qPCR) and whole-mount *in situ* hybridization (WISH). The three motile cilia-related genes we proposed to validate were *dnha7*^{ss}, *rsph3*^{***} and *foxj1a*^{†††}. It was our ultimate goal, to test causality between CBF patterns and gene expression.

With this Master project we wanted to test if *deltaD* mutants had a different CBF evaluation and whether that could partially explain the defects in L-R patterning reported (Lopes et al. 2010).

^{ss} *dnha7* (Dynein Heavy Chain 7) was one of such differentially expressed genes. The expression of *dnha7* mRNA is induced during ciliated cell differentiation, being present in normal motile cilia. Zhang et al (2002) identified DNAH7 as an inner dynein arm component of human cilia important for its motility. Cilia from PCD patients have an absence of DNAH7.

^{***} Initially identified in *Chlamydomonas*, *rsph3* (Radial Spoke Protein Homolog 3)⁸¹ is 1 of more than 20 identified radial spoke structural components of motile cilia and is required for axonemal sliding and flagellar motility. Radial spoke proteins are thought to be important in transducing signals from the inner pair of microtubules to the outer doublets in the flagellar axoneme, regulating dynein-mediated axonemal sliding and subsequent flagellar motility.
^{†††} *foxj1a* gene is considered the master motile ciliogenic transcription factor⁸², and as showed by Lopes et al.²⁷ is downstream of *DeltaD* since it successfully rescued cilia length in *deltaD*^{-/-} mutants in a cell-autonomous manner.

CHAPTER 2

Materials and Methods

2.1 Recording Cilia Beat Frequencies in the Kupffer's Vesicle

Recording cilia in the Kupffer's vesicle (KV) with high-speed videos allowed us to perform a detailed analysis on cilia beat frequency (CBF) from live embryos, providing novel information on cilia motility.

2.1.1 Zebrafish mating

AB wild type (WT) and *deltaD*^{-/-} mutant embryos were staged according to Kimmel et al. (Kimmel et al. 1995). In this project, zebrafish females and males were selected from the main tank-system and then added to the mating box in the evening. In the following morning females laid eggs and these were externally fertilized by males. The eggs fell through a sieve, being protected from cannibalism by parents. After this process, adult fish returned to the original tank and the collected eggs were placed in a Petri dish with embryonic medium (5 mM NaCl, 0.2 mM KCl, 0.3 mM CaCl₂, 0.3 mM MgSO₄, ddH₂O—pH 6.5). The Petri dishes with the collected eggs stayed at 32°C until the embryos reached the 6th somite-stage of development.

2.1.2 Mounting zebrafish live embryos for recording CBF in the KV

Visualize motile cilia inside the KV needed the development of a special mounting set up as the embryos are extremely fragile at this stage of development. Because we used an inverted microscope with the camera recording from the bottom, the zebrafish embryos had to be mounted with the dorsal roof of the KV facing the objective lens - defined as "dorsal view" (Figure 2.1A). For this purpose the embryo's head was facing up and consequently the KV dorsal roof was directed to the bottom of the mold. (Figure 2.1B)

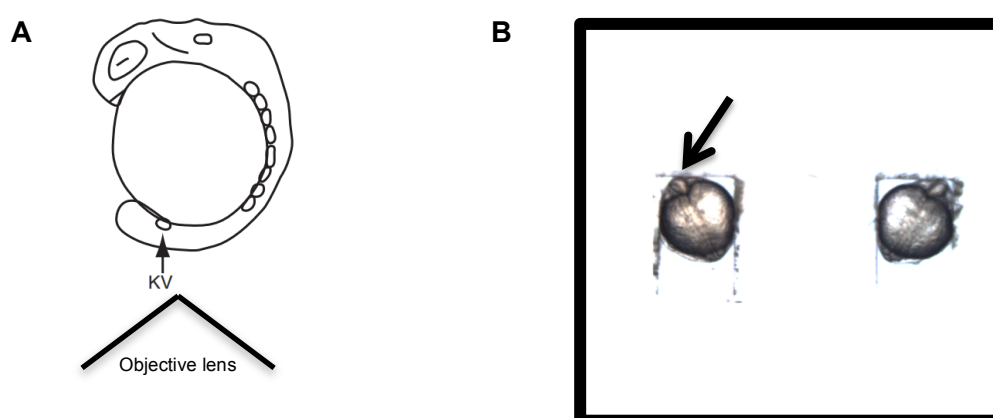


Figure 2.1 – Mounting of zebrafish live embryos for recording CBF in the KV: **A.** Schematic representation of an 8th somite-stage zebrafish embryo mounted for recording CBF in the KV, showing the dorsal roof of the KV facing the objective lens - "dorsal view". Picture adapted from (Jaffe et al. 2010). **B.** 8th somite-stage zebrafish live embryos mounted correctly inside the agarose mold, placed in the glass-bottom Petri dish (the arrow is pointing the zebrafish head).

Approximately at 6th somite-stage, live embryos were very carefully dechorionated and washed in embryonic medium to be finally placed inside the 2% agarose mold. With the help of little plastic forceps, embryos were placed correctly inside the mold so that KV was facing down the glass-bottom Petri dish (FluoroDishTM, WPI Inc, China) (Figure 2.1B). To immobilize embryos in this position inside the mold we used a solution of 1.5% low melting point (LMP) agarose (Jaffe et al. 2010) as an embedding medium. Because hot agarose could irreversibly damage zebrafish tissues, it was crucial to always check melted LMP agarose temperature prior using. Before covering the embryos it was necessary to eliminate the excess of liquid as it dilutes the agarose and impacts in its solidification. The polymerization process took a few minutes and once the agarose was solidified, the embryos were ready to be filmed.

2.1.3 Microscope setup

Mounted embryos were set under the 63x/1.20 water immersion objective lens (NA 1.20) on an Andor Revolution® XD Spinning disk laser microscopy system with the dorsal view facing the objective lens (Figure 2.1). Live images were recorded by video microscopy using a high-speed Andor iXon2 897 camera. The high-speed camera's management was done using *Andor IQ2 and Micromanager software 1.4* (Edelstein et al. 2001).

At the microscope the methodology consisted in finding the KV at the base of the zebrafish notochord (Figure 2.2) and focusing the condenser to obtain proper Difference Interference Contrast (DIC) quality images. A good DIC was the limiting factor for the acquisition of good quality images.

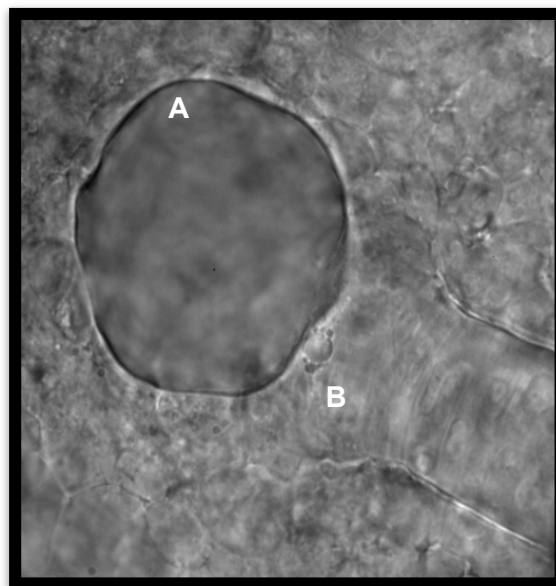


Figure 2.2 – Snapshot DIC image of a zebrafish KV from a live embryo filmed from the dorsal side. A: zebrafish KV; B: zebrafish notochord. 63x magnification.

2.1.4 Recording KV cilia – image frames acquisition

KV was scanned until a single beating cilium was found, and its anterior-posterior and left-right position was recorded, allowing a proper localization of each cilium filmed inside KV (See Movie 1 and 2 in Annex III).

The image sequence recorded for each cilium was a collection of snapshots, known as image frames, taken at a properly selected rate to avoid motion artifacts. In order to film individual cilia inside the KV as fast as possible, a small region of interest (ROI, $\sim 50 \times 50 \mu\text{m}$) was carefully manually defined as a narrow square around each cilium (Figure 2.3). Ciliary movement was recorded for each pixel within the ROI, resulting in a set of temporal waveforms with as many members as there were pixels inside the ROI. Each waveform depicted the pixel intensity as a function of time, displaying the periodicities of the ciliary movement (Olm et al. 2011) in a graph called kymograph (Figure 2.5A and 2.6).

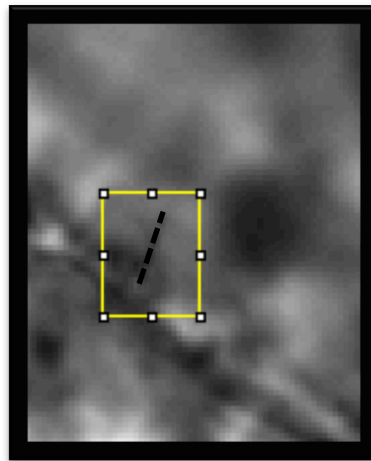


Figure 2.3 – ROI representation. Snapshot DIC image of a representative cilium (dashed line) inside the narrow square (ROI, $\sim 50 \times 50 \mu\text{m}$).

Accurate measurements of cilia beat frequencies were critically dependent on the frame rate at which images were acquired. The *Nyquist-Shannon* sampling theorem implies that to measure the frequency F_0 of cilia, acquisition of images should be performed at a rate more than twice as fast ($F > 2 * F_0$) (Jaffe et al. 2010). Not fulfilling this condition can lead to an artefact known as aliasing (motion artifacts). In practice, acquisitions at even faster rate are highly recommended (typically, $F > 3-4 * F_0$). The higher acquisition rate compensates for the fact that the movement cannot be exactly periodic and the measurement is of finite duration, overall facilitating the frequency measurement. Previous measurements have already shown that cilia beat frequencies in the KV are approximately 30 times per second (Kramer-Zucker 2005) (Okabe et al. 2008), and according to (Jaffe et al. 2010) a frame rate exceeding 120 frames per second (fps) is recommended.

In order to determine the best frame rate at which we should film, at the beginning of this project, I acquired videos with frame-rates from 91 up 380 fps. Experiments at higher temporal resolution (up to

380fps) were achieved by decreasing camera exposure from 10 to 2 ms. However these videos showed that the resolution of the resulting kymographs was dramatically decreased making it difficult to discriminate the cilium from the background. We determined by filming at 380fps that the highest fundamental frequency found was around 40Hz and therefore decided to use 91fps as an optimal acquisition speed. This experimental setup allowed us to measure 5 to 45 Hz CBF, which is the frequency range reported by other groups (Jaffe et al. 2010; Supatto & Vermot 2011) at a frequency resolution of 0.5 Hz. In summary, according to *Nyquist-Shannon* theorem ($F > 2 * F_0$), a frame-rate of 91pfs was fast enough to study the KV ciliary movement, and additionally, allowed the design of good quality kymographs.

The number of frames filmed was 1000 frames in total for each movie. With the frame-rate of 91fps, 1000 frames corresponded to a movie of 11 seconds. In summary, in this project the image acquisition of beating cilia were 1000 frames per cilium, during 11 seconds with a frame-rate of 91 fps.

2.1.5 Image processing and kymograph design

CBFs were obtained by image filtering using ImageJ program (<http://rsbweb.nih.gov/ij/>), followed by Fourier analysis in R software (R Development Core Team, 2010). Image frames were processed with ImageJ to extract the resulting kymographs. The main steps of ImageJ protocol were as follows: a) imotile objects must be removed by creating an average time projection of individual CBF recording (1000 frames) that was subtracted to each frame of the movie - as the result of such processing, the motile objects (such as the cilium) appeared as bright objects in a dark background (Figure 2.4); b) the 1000 frames were cropped to a small region ($\sim 10 \times 10\mu\text{m}$) enclosing the cilium; c) CBF image stacks (x, y, t) were represented as orthogonal views (x, t) and (y, t) (Figure 2.5A); d) a straight line was drawn over the time domain of the entire (x, t) kymograph - ImageJ returned the correspondent plot profile from each traced line in the kymograph (Figure 2.5B), which gave the number of peaks in the total period of time, and a list of values that corresponded to the position of the peaks over time in a XY axis (also named plot values - Figure 2.5C). The plot values list (Annex I), corresponding to the plot profile, was exported to R software to perform Fourier analysis with the Fast Fourier Transform (FFT) algorithm (Figure 2.5B, C).

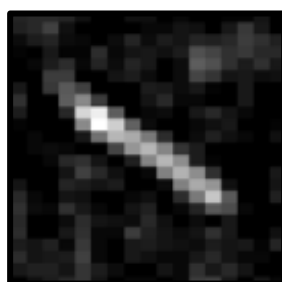


Figure 2.4 – Motile cilia after image processing. Cilia appeared as bright objects in a dark background.

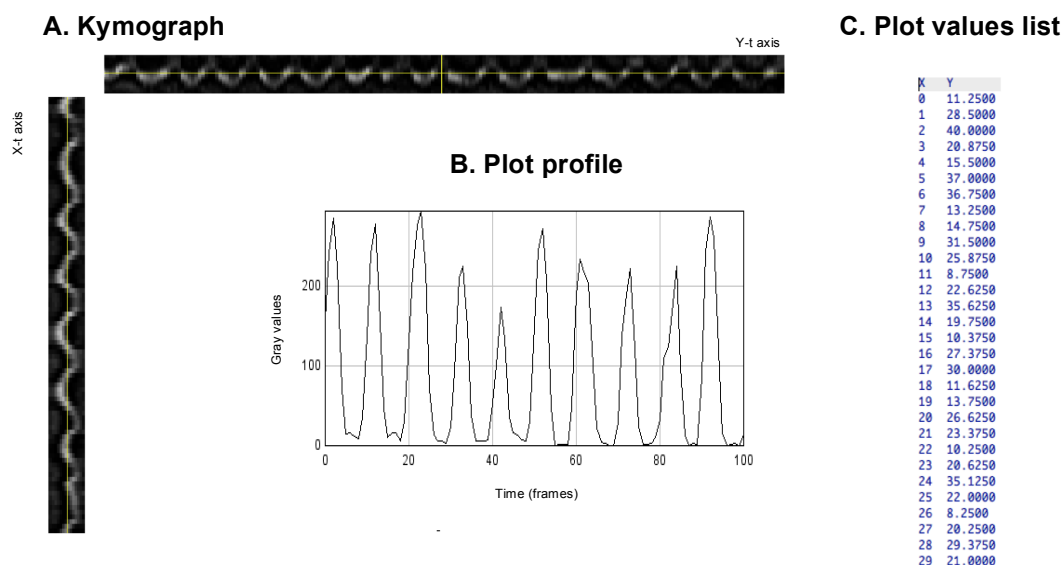


Figure 2.5 – ImageJ kymograph design. A: Kymograph analysis using an orthogonal view of the cilium, B: Plot profile resultant from the analysis of the line traced in the kymograph; C: Plot values list correspondent to the plot profile.

The first critical step after having imported all the images to ImageJ was to increase contrast between the pixel intensity of each cilium and its background. This was crucial to obtain a good kymograph and produce a correct spectral analysis.

The second critical step was the definition of the correct place to trace a straight line crossing the entire kymograph (the total 1000 image frames). Cilia that got out of focus for some periods of time had to be discarded from the analysis. To solve this problem, since spectral analysis was very sensitive to embryo drifting, we decided to do this analysis for 10 periods of each 1000 image frame video, by tracing a line correspondent to 90 frames (Figure 2.6) – segments of 90 frames. We also tested if randomly measuring any 10 periods along the 1000 frames would retrieve the same Fourier spectra (Figure S1 in Annex III) confirming the possibility of using only ten periods to study KV cilia CBF.



Figure 2.6 – Kymograph with the traced line represented. To solve the problem of analysing the entire kymograph, a 90 frame's line was used to study KV CBF. The line is drawn in yellow in a 300 frames representative kymograph.

2.1.6 CBF spectral analysis

The aim of the spectral analysis was to estimate, based on this set of waveforms, the proportion of each CBF value in relation to the overall movement of the cilia within the ROI. As described previously, for each cilium the list of plot values obtained using ImageJ was imported to R program. In collaboration with Dr. Adán Guerrero (Instituto Gulbenkian da Ciência) we developed a script for R program, which applies FFT to KV cilia data ("FFT function" in Annex II).

In this type of analysis time and frequency domains are related to each other by the FFT, so each variable in the time domain has a characteristic frequency spectrum. Fourier power spectra were obtained as a result of the applied FFT to the KV cilia data obtained by video-microscopy. In the end we could characterize each KV cilium by the number of the existent frequencies, represented as peaks in the Fourier spectra (Figure 2.7).

Significant cilia beat frequencies were selected from their Fourier spectra based on local maxima criteria using a frequency window of 4.5Hz. Only local maxima that were beyond 2Hz were considered. These parameters made the algorithm very robust, allowing a confident spectral analysis.

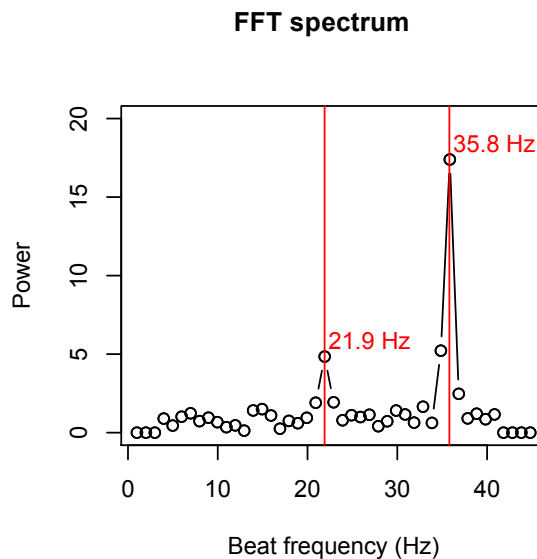


Figure 2.7 - Fast Fourier transform (FFT) spectral analysis. This cilium shows a double FFT spectrum. The corresponding measured frequencies are depicted in their Fourier spectra as vertical red lines

2.1.7 Statistical analysis of CBF results

Data were presented for a number of individual cilia (WT = 63 cilia; *deltaD*^{-/-} = 65 cilia) that were selected randomly from different KVs from at least 11 embryos of each genotype.

Differences in the number of cilia displaying a given CBF within WT and *deltaD*^{-/-} populations separately were assessed with the binomial test. Differences in the number of cilia between the WT and *deltaD*^{-/-} were assessed with the Fisher test. Differences in CBF were assessed using Wilcoxon non-parametric test. Multimodality in the single CBF populations was addressed by the Hartigan's dip test.

The coefficient of variation of the CBF was calculated as $c.v. = 100 \sigma / \mu$, where σ is the standard deviation and μ is the mean of the CBF. Differences in the dominant CBF variability were assessed with the Brown – Forsythe Levene's test.

All statistical tests were performed using R software (R Development Core Team, 2010), and all the codes used are described in Annex II. The significance level was set at 95%. Comparisons among videos (e.g. different beating cilia) were possible since all were recorded at the same magnification (63x) and with the same number of total frames (1000).

2.2 Cilia localization inside the Kupffer's vesicle

All cilia filmed for cilia beat frequency (CBF) studies were localized inside the Kupffer's vesicle, according to the axes left-right and anterior posterior. Using the scheme represented in Figure 2.8 we were able to localize cilia and correlate the localization with a specific CBF pattern after CBF spectral analyses. Differences in the localization of distinct cilia types inside KV were assessed with the Fisher test, using R software (R Development Core Team, 2010). The significance level was set at 95%.

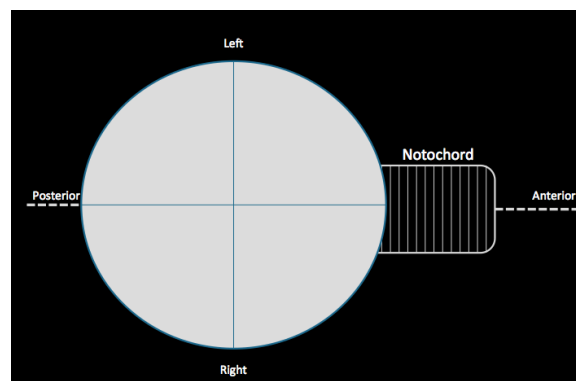


Figure 2.8 – Schematic Kupffer's vesicle used to annotate cilia localization.

2.3 High speed videomicroscopy for measuring the KV Fluid Flow

After analyzing the WT and *deltaD*^{-/-} mutant KV CBFs, we investigated the fluid flow velocity by measuring the native particles that move with the flow inside the vesicle. By tracking these particles we were able to measure the velocity of the fluid flow in a non-invasive way as in Lopes et al.(Lopes et al. 2010).

In terms of methodology this part of the project was very similar to CBF analysis (see section 2.1 in this Chapter). Zebrafish mating was performed as described in section 2.1.1. We used the same microscope and high-speed camera, and the embryos were also mounted with the dorsal view facing down (i.e. facing the microscope objective). The selected ROI was larger and included the entire zebrafish KV in order to film the particles moving inside without losing the global perspective of the movement (Figure 2.9). KVs without particles were discarded – the success rate was approximately 1:3. These KV movies had 3000 total frames each and were filmed with approximately the same frame-rate used for CBF analysis (91 fps).

The major difference in methodology compared to Lopes et al.(Lopes et al. 2010) occurred in the post-filming analysis. We used the ImageJ plugin named MTrackJ to follow each individual particle (<http://www.imagescience.org/meijering/software/mtrackj/>)(Meijering et al. 2012).

Particles were selected manually and the plugin automatically returned the X and Y coordinates of each point. For each particle we have analyzed 100 points (temporal window of analysis – 100 XY pairs of coordinates). All the coordinates were imported to an Excel datasheet (Microsoft® Excel® for Mac 2011 - version 14.2.3) and the velocity was calculated according to the following equation: $v=d/t$ (v = velocity, d = distance, t = time/frame-rate). Potential differences in KV Fluid Flow velocity between WT and *deltaD*^{-/-} mutant embryos were assessed using t-student's test, whereas for velocity variability was used the Brown – Forsythe Levene's test. As for CBF results, all statistical tests were performed using R software (R Development Core Team, 2010) - codes described in Annex II -, and the significance level was set at 95%.

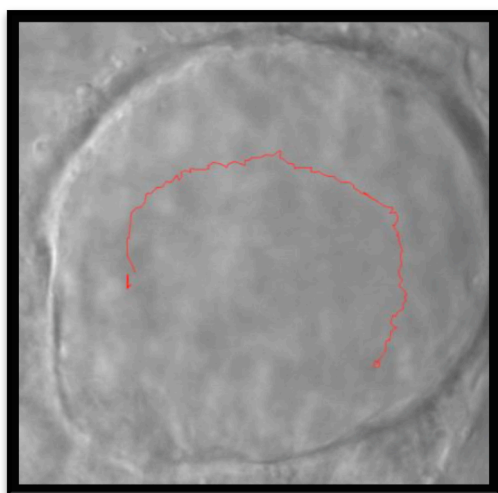


Figure 2.9 – Zebrafish KV with a tracked particle inside.

Using MtrackJ plugin from ImageJ software it was possible to follow particles inside the KV and calculate KV's fluid-flow velocity.

2.4 Molecular study of motility genes downstream of DeltaD

In order to understand the molecular players responsible for the motility defects present in *deltaD*^{-/-} mutants (Lopes et al. 2010), our lab performed a tissue specific screen^{†††} using microarrays that resulted in providing potential candidates. Among these, three candidates for motility defects were studied: *dnah7*, *rsph3* and *foxj1a* (see section 1.6 in Chapter 1). We validated the gene expression data for these genes by performing *in situ* hybridization and quantitative real-time Polymerase Chain Reaction (qPCR) experiments.

2.4.1 Whole-mount *in situ* hybridization (WISH)

In situ hybridization (ISH) is a powerful technique for localizing specific nucleic acid targets within fixed tissues and cells, allowing us to obtain temporal and spatial information about gene expression and genetic *loci* (C. Thisse & B. Thisse 2008). The big advantage of ISH is the greater amount of information gained by visualizing the results within the tissue, but on the other hand, ISH is not a good method for quantification.

We performed whole-mount *in situ* hybridization (WISH) experiments to study the localization of *dnah7*, *rsph3* and *foxj1a* gene expression in zebrafish embryos. In this experiment we used *ntl* (no-tail) a gene homologous to *brachyuri* in mouse, as positive control of the WISH experiments. All the RNA-probes used have been developed previously in the lab, except *dnah7* RNA-probes that were developed within this Master project (see section 2.4.3).

The WISH procedure followed Thisse's protocol (C. Thisse & B. Thisse 2008). Zebrafish mating occurred as described in the section 2.1.1. WISH was performed on 4% paraformaldehyde (PFA)/100% Methanol (MeOH) fixed zebrafish embryos at two distinct developmental stages (Table 2.1). Embryos were then brought through 75%, 50% and 25% MeOH-PBS for 5 min each at RT and then twice for 5 min in PBT (PBS/Tween20 0.1%) for rehydration. Embryos were dechorionated prior proteinase treatment. This treatment consisted in the embryo's digestion with Proteinase K (5mg/ml in PBT) at RT for 1 min (time recommended for embryos in early somitogenesis). Immediately after, embryos were fixed in 4% PFA for 20 min, followed by a series of washes in PBT.

The pre-hybridization and hybridization were conducted at 65°C for all ribo-probes in HYB-mix solution (Formamide (Roche), 20x SSC, Tween20 10%, 1M Citric acid to pH6 and heparine (0.63mg/ml)). After a pre-hybridization of at least two hours, the probes were added to the embryos and incubated overnight (see RNA-probes dilutions in Table 2.1).

In the second day, the probes were recovered and embryos were brought through 100%, 75%, 50% and 25% HYB-mix/2x SSC for 15 min each at 65°C and then once for 15 min in 2x SSC at 65°C.

^{†††} This tissue specific-screen was done using a zebrafish transgenic *sox17:GFP* line, that specifically labelled KV precursor cells, enabling their sorting by FACS. After the GFP sorting, the transcriptome of KV precursor cells were assessed by a microarray study.

Next, embryos were washed twice in 0.2 SSC for 30 min and then through 75%, 50% and 25% 0.2 SSC/PBT for 10 min each at RT, finishing with a RT wash in PBT for 10 min.

Embryos were blocked for at least 2 hours at RT with BSA, goat serum (GS) and PBT (50mL PBT with 100mg BSA and 1ml GS). *In situ* hybridization signals were detected with sheep anti-digoxigenin-AP Fab fragments (Roche Mannheim, Germany), and incubated at a 1:5000 dilution in blocking solution, overnight at 4°C.

In the next day antibody solution was removed and embryos were washed in PBT in a 6-times series of 15 min. Next embryos were equilibrated in staining buffer (1M TRIS pH9.5, 1M MgCl₂, 5M NaCl and Tween20 10%), 3 times for 5 min each at RT. The color staining was carried out with NBT/BCIP (Roche Mannheim, Germany), alkaline phosphatase substrates, until the probes reached the desired level of purple staining. In order to stop the staining reactions we used 4% PFA for 20 min at RT, followed by several washes in PBS prior to mounting embryos in 100% glycerol.

WISH results were photographed using an upright microscope (Leica DMLB2) and images were treated with Leica's software.

Table 2.1 – WISH experiment: list of mRNA-probes, dilution factors and embryo-stages used.

mRNA-probes	Dilution factor	Embryo-stage used
<i>dnha7</i>	5:200	Bud-stage and 8 th somite-stage
<i>rsph3</i>	4:100	
<i>foxj1a</i>	8:400	
<i>ntl</i>	0.5:100	8 th somite-stage

2.4.2 Quantitative Real-Time Polymerase Chain Reaction experiments

After performing WISH experiments to study the localization of *dnha7*, *rsph3* and *foxj1a* gene expression in WT and *deltaD*^{-/-} embryos, a qPCR experiment was done using bud-stage zebrafish embryos (see section 3.3 in Chapter 3 for WISH results) for gene expression analysis.

Since its introduction more than ten years ago, qPCR has become the standard method for quantification of levels of transcription. qPCR provides the simultaneous measurement of gene expression in many different samples for a limited number of genes, and is especially suitable when only a small number of cells are available.

For qPCR, two pools of 100 WT and 100 *deltaD*^{-/-} mutant embryos were collected at bud-stage. Total RNA was isolated using RNeasy[®] micro Kit (Qiagen Inc., Valencia, CA) according to the instructions of the manufacturer, and later quantified at the NanoPhotometer[®] P-Class (IMPLEN). This

quantification was important to guaranty that only RNA of high integrity (not degraded) was used. Given the prevalence of RNases in the environment, we performed the reverse transcription of total RNA samples into cDNA immediately after the quantification. One microgram of total RNA from WT and *deltaD*^{-/-} mutant embryos was reverse-transcribed using iScriptTM cDNA Synthesis Kit (BIO-RAD, Hercules, CA) according to the manufacturer's instructions.

Primers for amplification were designed with Primer - BLAST (NCBI) and sequences are shown in Table 2.2. The primer sequence of *ef1a* was according to (Silva et al. 2011).

Using the qPCR thermal-cycler, we decided to perform a temperature gradient reaction - around the calculated primer's melting temperature in order to determine the optimal annealing temperature for each primer pair. The amplification profiles indicated that the most efficient amplification for each primer pair occurred at the annealing temperatures where the curves were at the lowest C_t (Table 2.2).

Table 2.2 – qPCR analysis: list of primers, annealing temperatures (T_a) and qPCR reaction efficiency (for all genes studied by qPCR the reaction efficiency was higher than 95%).

Gene	Forward primer	Reverse primer	T _a
<i>sox17</i>	CCTGCACAATGCGGAGCTGAGT	ACGTTTCGGCCTCCTCAACGA	71.2°C
<i>ef1a</i>	ACGCCCTCCTGGCTTTCACCC	TGGGACGAAGGCAACACTGGC	71.2°C
<i>dnha7</i>	AGTCCCGCTCTTCAGGTGGCA	AGCTGGTGGGGTACTTGCGC	66.9°C
<i>rsph3</i>	TGAAGAGAGGGAACGGCGCCT	TGCTGAGCAAATGCCCTCGCA	66.9°C
<i>foxj1a</i>	CGCCACGCAGATCCCACCTG	TCCAGAAGCCGCTTTGCC	66.9°C

qPCR was performed on the CFX96TM Real-Time PCR Detection System (BIO-RAD, Hercules, CA) using the SsoFastTM EvaGreen[®] Supermix (BIO-RAD, Hercules, CA). Cycling parameters were as follows: 95°C for 3 min and 49 cycles of the following: 95°C for 10s, 71.2°C (for *sox17* and *ef1a*) or 66.9°C (for *dnha7*, *foxj1a* and *rsph3*) for 30s, and 70°C for 30s. Fluorescence changes were monitored with EvaGreen after every cycle.

One of the important features of qPCR experiments is the establishment of the standard curve. A standard curve is generally used to determine the qPCR reaction efficiency. Standard procedures were followed for a standard curve design (Hellemans et al. 2007; Vandesompele et al. 2002; Taylor et al. 2010) and four replicates of a 10-fold dilution series for each gene under study were produced. Furthermore, in every run for each primer pair in test, was included a template control (NTC) reaction to ensure no DNA contamination and no unspecific amplifications or formation of primer-dimers (Figure 2.10). All reactions were performed in duplicates. *sox17* and *ef1a* were used as reference controls since their expression did not vary between WT and *deltaD*^{-/-} mutant embryos. Reference genes are used as controls to normalize the data, correcting the differences in amplification caused

by stochastic variations during qPCR. The target stability value calculated based on Bio-Rad CFX Manager 2.0 software (BIO-RAD, Hercules, CA) was used to confirm the validity of the chosen genes as reference (mean coefficient variance < 0.25 and mean M value < 0.5). All the results were evaluated with the Bio-Rad CFX Manager 2.0 software (BIO-RAD, Hercules, CA). The data were calculated by the comparative method using C_t values of *sox17* and *ef1a*.

	1	2	3	4	5	6	7	8	9	10
A	Std dnah7 Wt	Std dnah7 Wt	Std dnah7 Wt	Std dnah7 Wt	Std dnah7 Wt	Std dnah7 Wt	Std dnah7 Wt	Std dnah7 Wt	NTC dnah7 Wt	NTC dnah7 Wt
B	Std dnah7 deltaD	Std dnah7 deltaD	Std dnah7 deltaD	Std dnah7 deltaD	Std dnah7 deltaD	Std dnah7 deltaD	Std dnah7 deltaD	Std dnah7 deltaD	NTC dnah7 deltaD	NTC dnah7 deltaD
C	Std foxj1a Wt	Std foxj1a Wt	Std foxj1a Wt	Std foxj1a Wt	Std foxj1a Wt	Std foxj1a Wt	Std foxj1a Wt	Std foxj1a Wt	NTC foxj1a Wt	NTC foxj1a Wt
D	Std foxj1a deltaD	Std foxj1a deltaD	Std foxj1a deltaD	Std foxj1a deltaD	Std foxj1a deltaD	Std foxj1a deltaD	Std foxj1a deltaD	Std foxj1a deltaD	NTC foxj1a deltaD	NTC foxj1a deltaD
E	Std rsph3 Wt	Std rsph3 Wt	Std rsph3 Wt	Std rsph3 Wt	Std rsph3 Wt	Std rsph3 Wt	Std rsph3 Wt	Std rsph3 Wt	NTC rsph3 Wt	NTC rsph3 Wt
F	Std rsph3 deltaD	Std rsph3 deltaD	Std rsph3 deltaD	Std rsph3 deltaD	Std rsph3 deltaD	Std rsph3 deltaD	Std rsph3 deltaD	Std rsph3 deltaD	NTC rsph3 deltaD	NTC rsph3 deltaD

Figure 2.10 – Example of a plate for qPCR. Four replicates of a 10-fold dilution series were produced for each gene (10^{-1} for columns 1 and 2; 10^{-2} for columns 3 and 4; 10^{-3} for columns 5 and 6; 10^{-4} for columns 7 to 8). In the 9th and 10th columns was included a template control (NTC). Wells from A and B lines belonged to *dnah7* gene, C and D lines to *foxj1a* and E and F lines to *rsph3*.

2.4.3 Cloning of dynein axonemal heavy chain 7 (*dnah7*)

As described previously in this project we had to develop one mRNA-probe for *dnah7* WISH experiments. We cloned a specific region of the *dnah7* gene by using pGEM®-T easy vector system and *E. Coli* bacteria.

2.4.3.1 PCR amplification

dnah7 cDNA sequence (ENS DART00000026924) was analyzed using *Ensemble Gene Browser* for the zebrafish genome (Ensembl - Zv9) and used to design PCR specific primers with Primer Blast.

dnah7 gene was amplified by PCR *touchdown* using a forward primer (5'-GCAAAAGGAATGCCCCAAGAAA-3') and a reverse primer (5'-GTGCCAGGCTTTGGAGCTGTG-3'). PCR was optimized in MyCycler™ (Thermal Cycler) instrument.

Only one specific band was obtained in several amplifications. The brighter band was cut from the electrophoresis gel and purified using Wizard®SV Gel and PCR Clean-up System (Promega), according to the manufacture's protocol. For that propose, the excised *dnah7* DNA band was placed in a 1.5 ml eppendorf tube. At last, the DNA was resuspended from the SV Minicolumn using 30µl of Nuclease-free water. The *dnah7* DNA was quantified using *NanoPhotometer® P-Class* (IMPLEN) and stored at 4°C.

2.4.3.2 *dnah7* cloning into pGEM®-T easy vector

A plasmid containing resistance to ampicillin was used as a vector. The insertion of *dnha7* DNA (PCR product) into the plasmid was done using the pGEM®-T easy vector system (Promega) according to Table 2.3. After ligation overnight at 4°C, the plasmid was then used to transform *E. coli* bacteria. Before starting the transformation reaction we prepared LB plates with ampicillin as a selective medium for the bacteria. Only bacteria that had acquired the plasmid could grow on the plate rich in ampicillin.

Table 2.3 – Reaction mixture for the *dnah7* DNA ligation with pGEM®-T easy vector system: list of reagents and quantities used.

Reagent	Quantity used (10 µl maximum volumm)
<i>2X Rapid Ligation Buffer T4 DNA Ligase</i>	5 µl
<i>pGEM®-T easy vector system</i>	1 µl
<i>dnah7</i> DNA (PCR product)	3 µl
<i>T4 DNA Ligase</i>	1 µl

The transformation was done using the SBCLNG EFF DH5α (Invitrogen™) competent cells, stored at -80°C. To start, 50 µl of competent cells were carefully transferred to the ligation tube containing 2 µl of the ligation reaction, previously described. The tube was gently flicked and incubated on ice for 30 min, followed by a heat-shock for 90 seconds at 42°C in a dry bath. The tube was immediately returned to ice for more 2 min. Next, 400 µl of LB without agar or ampicillin were added to the tube containing the competent cells and placed for 1 hour at 37°C, with mild shaking (approximately 150 rpm). Two different volumes (100µl and 50µl) of competent cells mixture were plated in the LB plates with ampicillin previously prepared, and incubated overnight at 37°C (with mild shaking - approximately 150 rpm), in order to let competent cells selectively grow.

In the next day, based on the ampicillin selection, up to 6 individual colonies were picked up from the LB plate and grown separately in 15ml centrifuge tubes with 5ml of LB medium with 5 µl of ampicillin, at 37°C for 16h. After this incubation, 2ml of the mixture were added to glycerol and stored at -80°C for later use. The other 3ml were used in the following protocols. DNA plasmid from each colony was purified using Wizard®Plus SV minipreps (Promega), eluted in 30 µl of Nuclease-free water, and quantified at NanoPhotometer® P-Class (IMPLEN). The resulting DNA was stored at -20°C in the freezer.

2.4.3.3 mRNA *in vitro* transcription and probe production

Using NEBcutter V2.0 (New England BioLabs®Inc - <http://tools.neb.com/NEBcutter2/>) we studied the *dnah7* DNA sequence and found the sites for all commercially available restriction enzymes that did not cut the *dnah7* sequence. *Not I* was used to linearize the plasmid, since this restriction enzyme only cuts the plasmid (and not the *dnah7* insert), according to Table 2.4. This reaction occurred at 37°C for 2 hours and the confirmation of the size of the insert plus the plasmid was done by gel electrophoresis.

Table 2.4 – Reaction mixture for *dnah7* insert release with *Not I*: list of reagents and quantities used.

Reagent	Quantity used for 1 reaction (30 µl maximum volume)
<i>NEBuffer 3</i>	1 µl
<i>BSA</i>	0.3 µl
<i>Not I</i>	0.5 µl
<i>DNA</i>	5 µl
<i>Milli-Q water</i>	21.2 µl

Since we wanted to develop a RNA-probe for WISH, both sense and anti-sense transcripts were designed and then blindly tested for WISH. The high copy number pGEM®-T Easy Vectors contain two distinct RNA Polymerase promoters, T7 and SP6, one on each side of the multiple cloning site, allowing transcription of either strand of an inserted sequence – Figure 2.11.

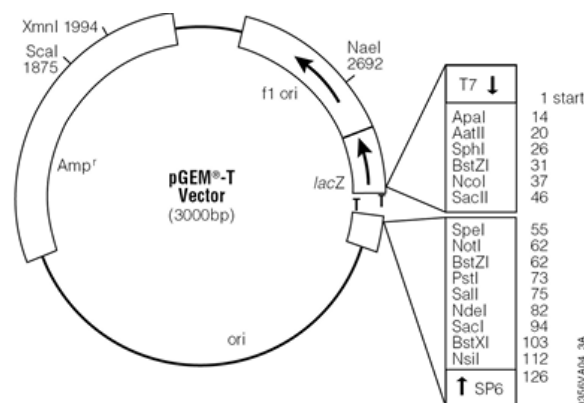


Figure 2.11 – Scheme of pGEM®-T easy vector system

Again, using Nebcutter V2.0 we found the proper restriction enzymes to perform the digestion and the *in vitro* transcription of *dnha7* DNA fragment. Accordingly, the digestion of *dnah7* DNA was performed with the enzymes *SacI* for using the T7 RNA Polymerase promoter, and *SacII* for using the SP6 RNA Polymerase promoter, following the conditions described in Table 2.5 and Table 2.6, respectively. This step of the protocol was performed at 37°C over-night, and later confirmed by an electrophoresis assay. The sample purification was done using DNA Clean and Concentrator™-5 kit (Zymo) and quantified at NanoPhotometer® P-Class (IMPLEN).

Table 2.5 – Reaction mixture for the plasmid digestion with *SacI*: list of reagents and quantities used. The Buffer 5 from Biolabs did not contain BSA.

Reagent	Quantity used for 1 reaction (30 µl maximum volume)
<i>Buffer 5 (Biolabs)</i>	3 µl
<i>BSA</i>	0.3 µl
<i>Sac I</i>	1 µl
<i>DNA</i>	9 µl
<i>Milli-Q water</i>	17 µl

Table 2.6 – Reaction mixture for the plasmid digestion with *SacII*: list of reagents and quantities used. The Buffer J from Promega includes BSA.

Reagent	Quantity used for 1 reaction (30 µl maximum volume)
<i>BufferJ (Promega)</i>	3 µl
<i>Sac II</i>	1 µl
<i>DNA</i>	9 µl
<i>Milli-Q water</i>	17 µl

At last, we performed the *in vitro* transcription and probe production of *dnha7*, at 37°C for 3 hours, following the conditions described in Table 7. Antisense and sense digoxigenin (DIG)-labeled RNA probes were generated using the DIG RNA labeling mix (Roche Diagnostics, Germany). After incubation the *dnha7* RNA probes were purified using Roche mini quick spin RNA columns (Roche) and quantified at *NanoPhotometer® P-Class* (IMPLEN). The probes were then blindly tested by WISH (see section 3.4 in Chapter 3).

Table 2.7 – Reaction mixture for *in vitro* transcription and RNA probe production: list of reagents and quantities used.

Reagents	Quantity used for 1 reaction (20 µl maximum volume)
<i>Transcription Buffers:</i> <i>Buffer5 (Promega) for SacII</i> <i>and</i> <i>BufferJ (Promega) for SacI</i>	4 µl
<i>DNA</i>	6 µl (maximum)
<i>DIG (Roche)</i>	2 µl
<i>DTT 0.75M</i>	1 µl
<i>RNAse inhibitor</i>	0.5 µl
<i>RNA Polymerase</i> <i>(SP6 for Sac II and T7 for SacI)</i>	1 µl
<i>Milli-Q water</i>	5.5 µl

CHAPTER 3

Results

The results obtained by performing high-speed videomicroscopy in the Kupffer's vesicle (KV) are reported here. These included Cilia Beat Frequency (CBF) studies and KV fluid-flow velocity measurements, both in wild-type (WT) and *deltaD*^{-/-} mutant embryos. One important feature of this study was the fact live embryos after being filmed, have survived and have the same characteristics as a non-filmed zebrafish embryo.

In addition, to complement the biophysical work with molecular studies we validated gene expression results from a tissue-specific screen previously done in our lab for a cluster of genes involved in motility by whole-mount *in situ* hybridization (WISH) and quantitative real-time polymerase chain reaction (qPCR) for WT and *deltaD*^{-/-} mutant embryos.

3.1 Recording Cilia Beat Frequencies in Kupffer's vesicle

By performing the Fast Fourier Transform (FFT) spectral analysis on cilia data acquired by high-speed videomicroscopy as described in the previous Chapter, we were able to classify cilia according to the number of Cilia Beat Frequencies (CBFs) revealed in the spectra.

3.1.1 Cilia Beat Frequency analysis in WT identifies two cilia populations

Our results show that in the WT zebrafish organizer there are two major populations of motile cilia characterized by different CBFs ($p < 0.05$, binomial test): one population characterized by each cilium having a single CBF (60%) and a second population characterized by each cilium having double CBFs (35%) - Figure 3.1. In addition, immotile cilia (3%) and cilia that beat with more than two CBFs (2%) were also seen.

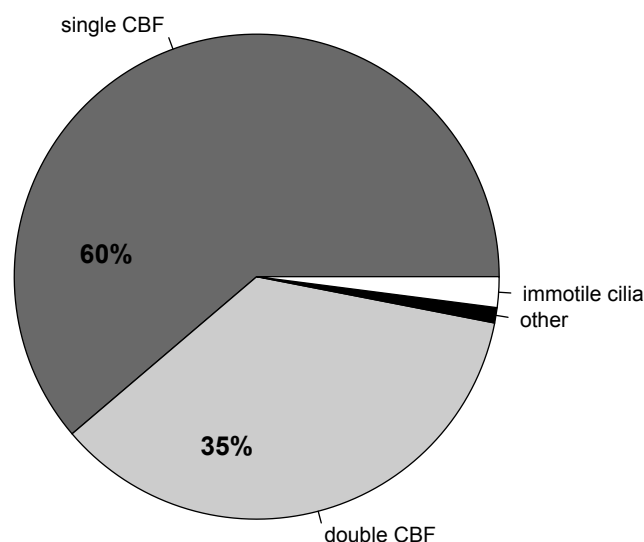


Figure 3.1 – WT CBF population: quantification of the different types of cilia according to CBFs in the Kupffer's vesicle - 60% of total cilia observed beat with single CBFs, whereas 35% of total cilia observed beat with double CBFs. 3% of immotile cilia and 2% of cilia with more than two CBFs were observed. $n_e=11$, $n_c=63$. CBFs (cilia beat frequencies); n_e (number of embryos), n_c (number of cilia).

Within the population of cilia that displays one single CBF there are two subpopulations, reflected on the bimodality of the distribution. One subpopulation beats around 25Hz and another around 37Hz (Figures 3.2A; $p < 0.05$, Hartigan's dip test). Two representative Fourier power spectra from the subpopulations of cilia with one single CBF are shown in Figure 3.2B and 3.2C. Along a period of time of eleven seconds these cilia always displayed only one CBF detected by FFT.

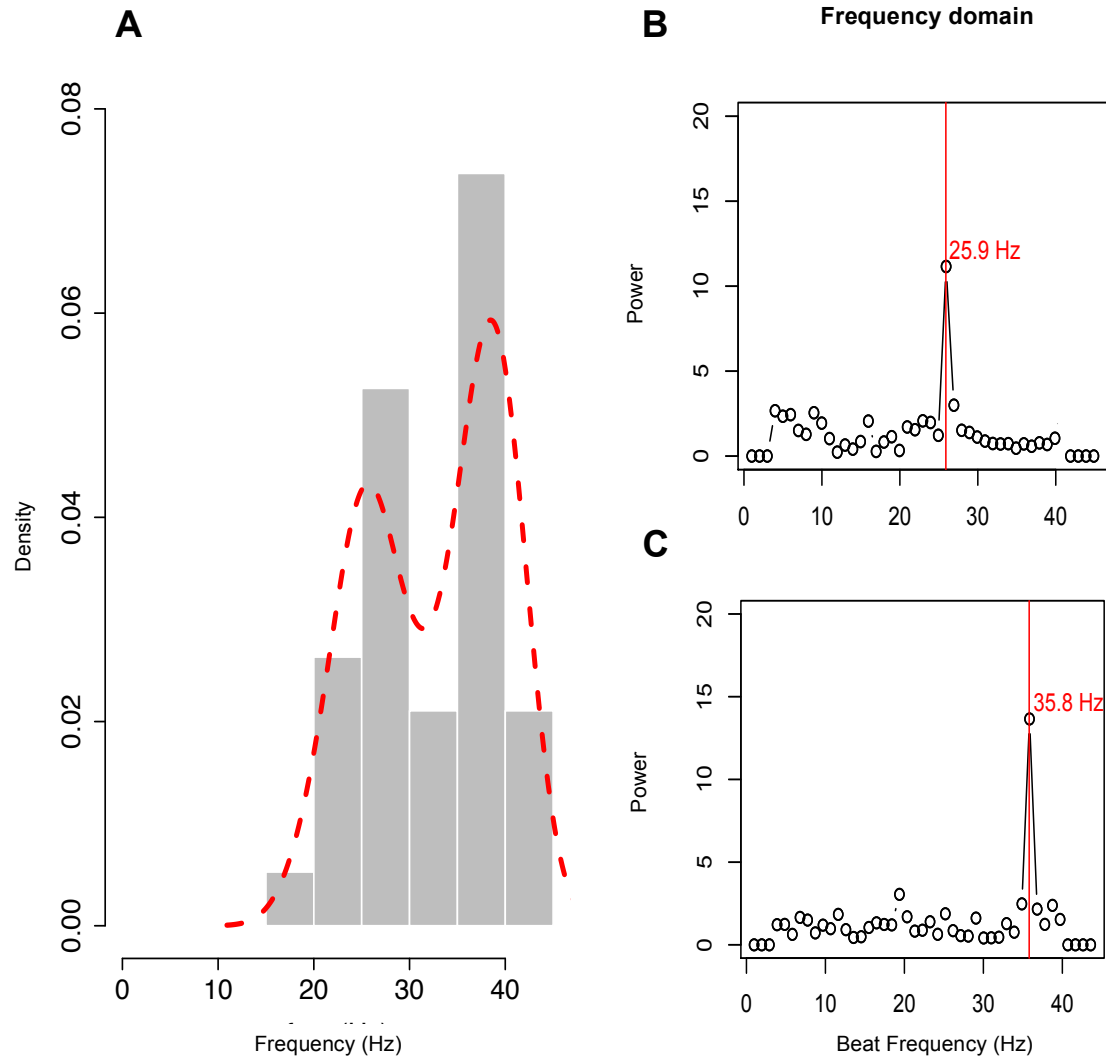


Figure 3.2 – WT cilia population with single CBFs: A- CBF frequency distribution of the cilia population that displays single CBFs; B and C - Representative results from one cilium with single CBFs after FFT spectral analyses. CBF (cilia beat frequency).

In addition, the second population of WT cilia is characterized by each cilium beating at two different CBFs - one around 18Hz and another around 37Hz (Figures 3.3A). A representative Fourier power spectrum from the WT cilia population with double CBFs is shown in Figure 3.3B.

To better examine these cilia displaying double frequencies we further classified the frequencies into dominant and secondary according to the power of the FFT spectra (Figure 3.4). This analysis showed that the dominant frequency was the higher, averaging 37Hz, whereas the secondary frequency averaged 18Hz (Figure 3.4C; $p < 0.01$, Wilcoxon test). The dominant frequency is the one that occurs more often, meaning these cilia spend more time beating faster.

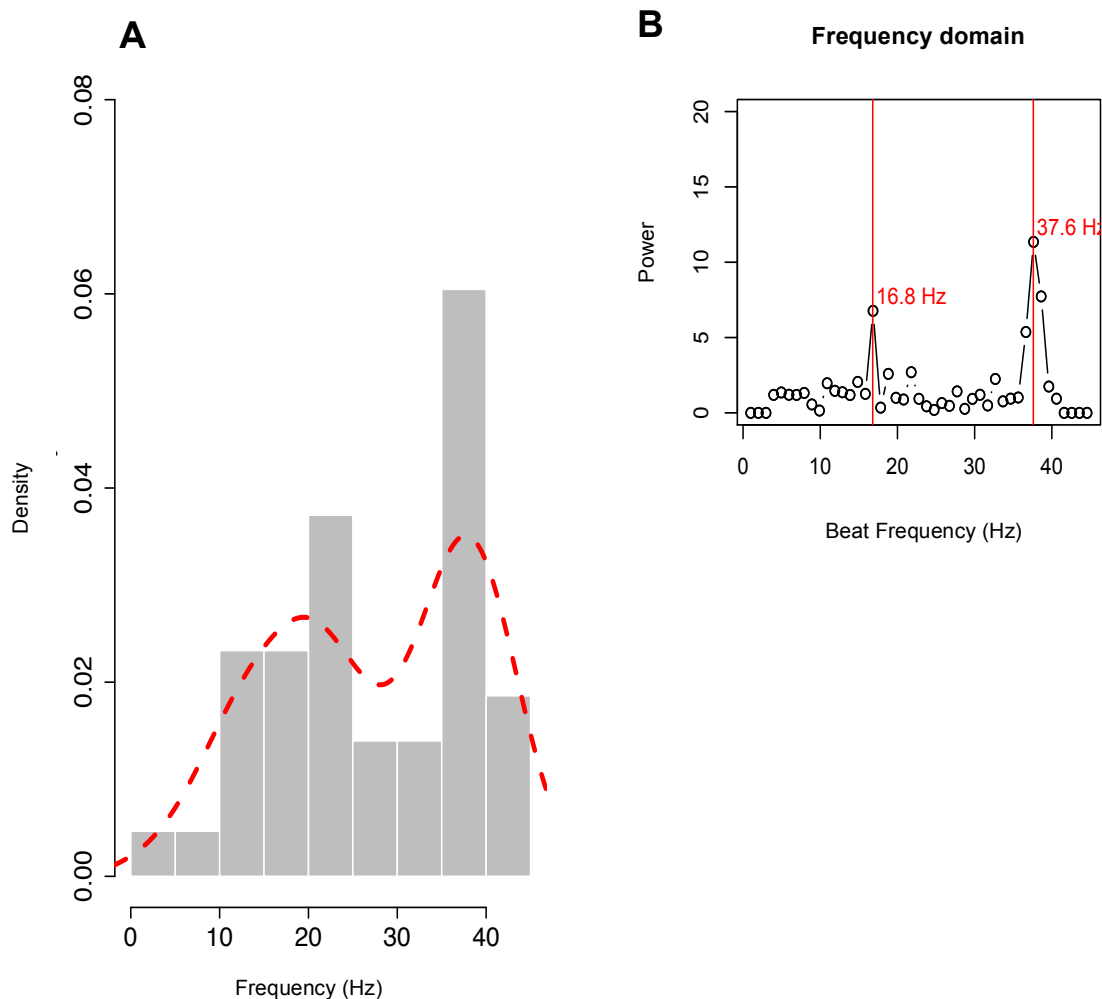


Figure 3.3 - WT cilia population with double CBFs: A - CBF frequency distribution of the cilia population that displays double CBFs; B - Representative result from one cilium that has double CBFs after FFT spectral analyses; CBF (Cilia Beat Frequency)

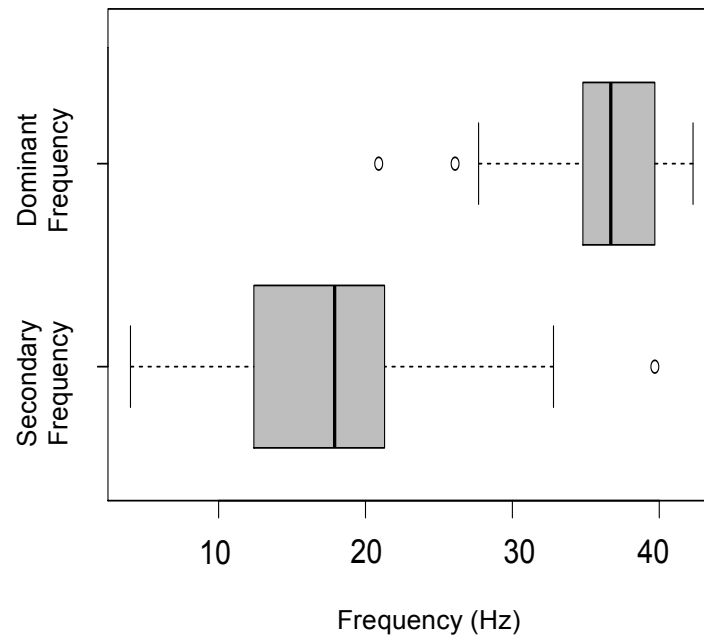


Figure 3.4 - Classification of double CBFs into dominant and secondary frequencies of the WT double cilia population. The double frequencies are statistically different ($p < 0.01$); CBFs (Cilia Beat Frequencies).

Furthermore, by comparing WT KV cilia that beat at single CBFs (Figure 3.2A) with those that have double CBFs (Figure 3.3A) it was clear that the lower frequency values ($< 15\text{Hz}$) present in the cilia with double CBFs are absent from the cilia with single CBFs.

Altogether, our data for WT embryos revealed two different populations of motile cilia based on the criteria of CBF number by spectral analysis using FFT.

3.1.2 *deltaD*^{-/-} mutants have a wider range of Cilia Beat Frequencies

Next, we have analysed the CBFs in zebrafish *deltaD*^{-/-} homozygous mutants. These mutants were characterized before by having shorter cilia, defective fluid flow and gut laterality defects (Lopes et al. 2010).

Judging by their CBFs spectral analysis, we found that the two different cilia populations identified in the WT embryos were maintained in the mutant ($p < 0.01$, binomial test), both cilia that beat at a single CBF and cilia that display double CBFs (Figure 3.5). The proportion of each population was different in the *deltaD*^{-/-} mutants, since cilia that beat at only one CBF increased from 60 to 74% at the expense of those that have double CBFs (18%) - Figure 3.5 compared to Figure 3.1. However, no statistical differences were found by comparing *deltaD*^{-/-} CBF classification against WT ($p = 0.14$, Fisher test). Some immotile cilia (6%) and some cilia that beat with more than two CBFs (2%) were also seen, similarly to WT.

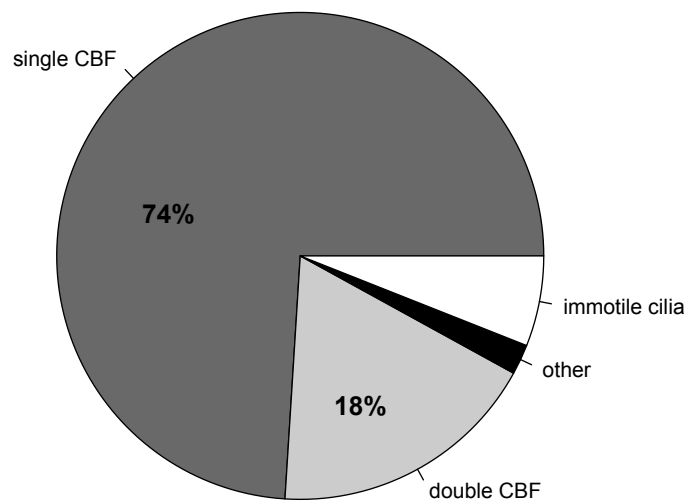


Figure 3.5 – *deltaD*^{-/-} mutants CBF population: quantification of the different types of cilia according to CBFs in the Kupffer's vesicle - 74% of total cilia observed beat with single CBFs, whereas 18% of total cilia observed beat with double CBFs. 6% of immotile cilia and 2% of cilia with more than two CBFs were observed. $n_e=16$, $n_c=65$. CBF (cilia beat frequency); n_e (number of embryos), n_c (number of cilia).

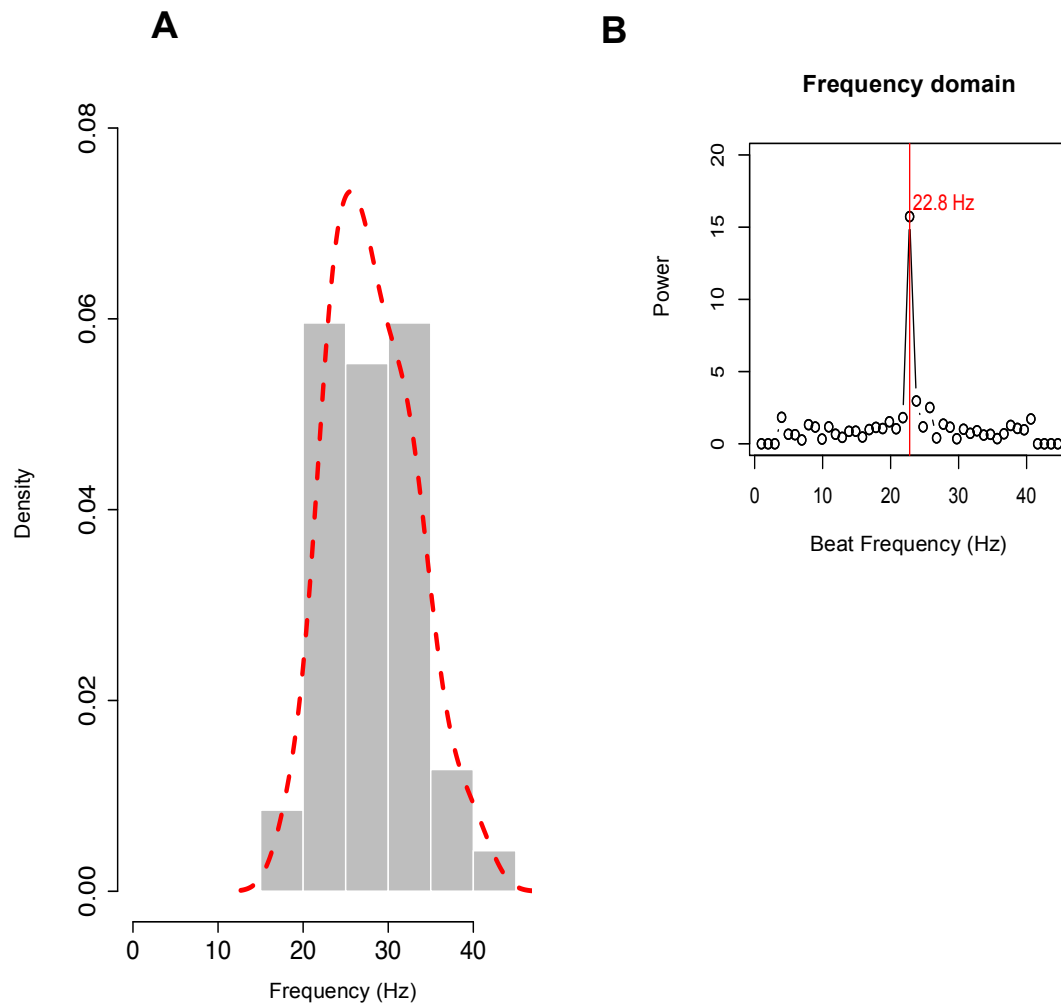


Figure 3.6 - *deltaD*^{-/-} cilia population with single CBFs: A - CBF frequency distribution of the cilia population that displays single CBFs; B - Representative result from one cilium with single CBFs after FFT spectral analyses. CBF (cilia beat frequency)

Regarding the cilia population characterized by a single CBF we identified only one subpopulation in the *deltaD*^{-/-} mutants beating at around 25Hz (Figures 3.6A – compare to Figure 3.2A; $p = 0.4$, Hartigan's dip test). A representative Fourier power spectrum from the subpopulations of one single *deltaD*^{-/-} mutants CBF cilia is shown in Figure 3.6B. Similarly to the WT, along a period of time of eleven seconds these cilia always displayed only one CBF detected by FFT.

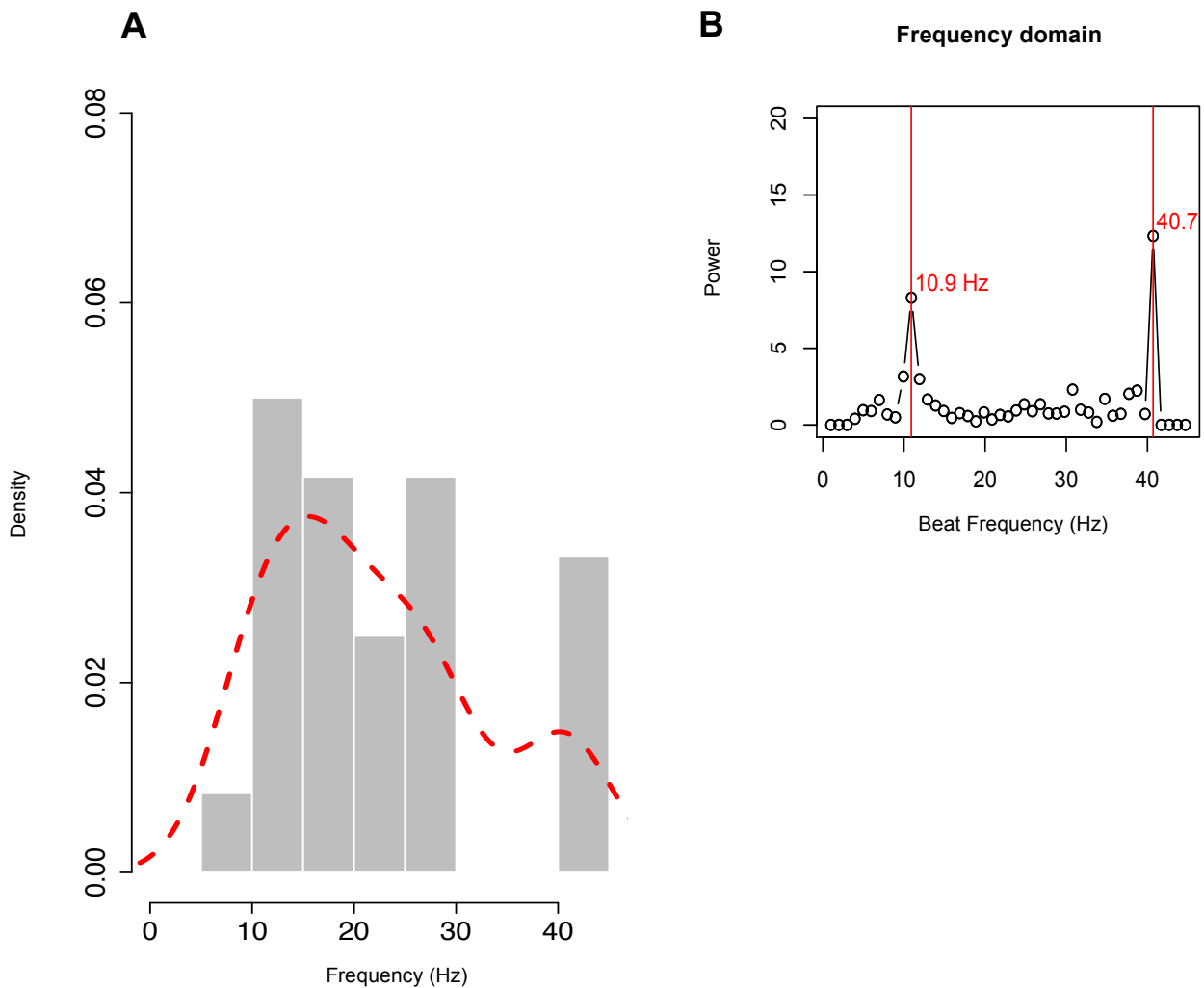


Figure 3.7 - *deltaD*^{-/-} cilia population with double CBFs: A- CBF frequency distribution of the cilia population that displays double CBFs; B - Representative result from one cilium that has double CBFs after Fast Fourier transform spectral analyses; CBF (cilia beat frequency).

In addition, the second population of *deltaD*^{-/-} mutant cilia is characterized by each cilium beating at two different CBFs - one around 15Hz and another around 40Hz (Figures 3.7A). A representative Fourier power spectrum from the population of *deltaD*^{-/-} mutant cilia with double CBFs are shown in Figure 3.7B.

Classification of the mutants into dominant versus secondary frequencies was significantly different ($p < 0.05$, Wilcoxon test).

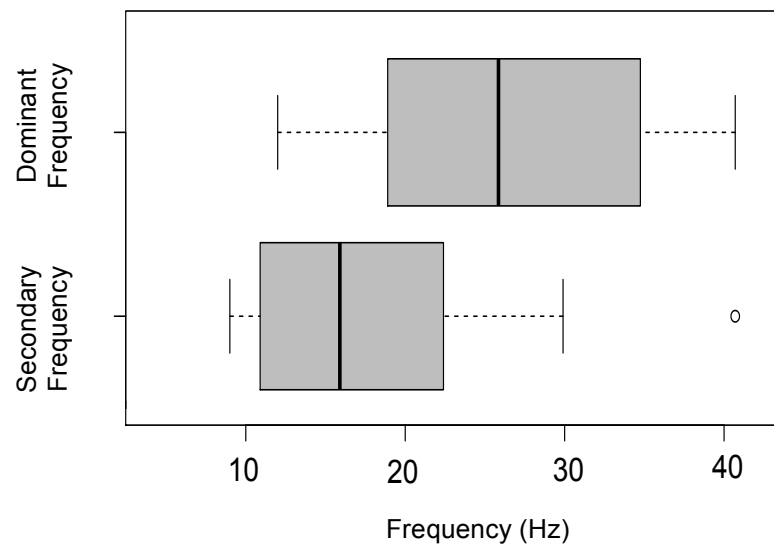


Figure 3.8 - Classification of double CBFs into dominant and secondary frequencies of the $\delta\text{eltaD}^{-/-}$ double cilia population. The double frequencies are statistically different ($p < 0.05$); CBFs (Cilia Beat Frequencies).

Furthermore, $\delta\text{eltaD}^{-/-}$ mutant embryos showed a greater dispersion of frequency values compared to the WT, relatively to the dominant frequency ($p = 0.03$; Brown-Forsythe Levene's test, Table 3.1). By comparing the $\delta\text{eltaD}^{-/-}$ mutant cilia secondary frequency with the dominant frequency of WT, despite the first had a higher value of coefficient of variation, the reduced number of $\delta\text{eltaD}^{-/-}$ mutant cilia with double CBFs did not allow the existence of differences between them. Nevertheless, the distribution of the dominant frequencies (mean = 26 Hz) changed to lower values than the observed WT values (mean = 35 Hz) ($p < 0.05$, Wilcoxon test) (compare Figure 3.8 and 3.4).

Table 3.1 – Summary statistics over variability in CBF. Brown-Forsythe Levene's test - Coefficient of variation: as c.v. = $100 \sigma/\mu$.

	C_v	Variability $p.value^a$			
		wt 1 st freq.	wt 2 nd freq.	$\delta\text{eltaD}^{-/-}$ 1 st freq.	$\delta\text{eltaD}^{-/-}$ 2 nd freq.
wt 1 st freq.	15.4	-			
wt 2 nd freq.	43.6	0.18	-		
$\delta\text{eltaD}^{-/-}$ 1 st freq.	37.8	0.03	0.34	-	
$\delta\text{eltaD}^{-/-}$ 2 nd freq.	52.8	0.11	0.34	0.74	-

In summary, our data showed that $\delta\text{eltaD}^{-/-}$ mutant cilia have on average lower CBFs than WT embryos but display a wider range of dominant frequencies.

3.2 Cilia localization in the Kupffer's vesicle

Taking into consideration the correlation between the cilia localization and the two different types of motile cilia observed by CBF analysis, we found that WT and *deltaD*^{-/-} mutant cilia types were placed randomly inside Kupffer's vesicle (Figure 3.9A for WT and B for *deltaD*^{-/-} mutants).

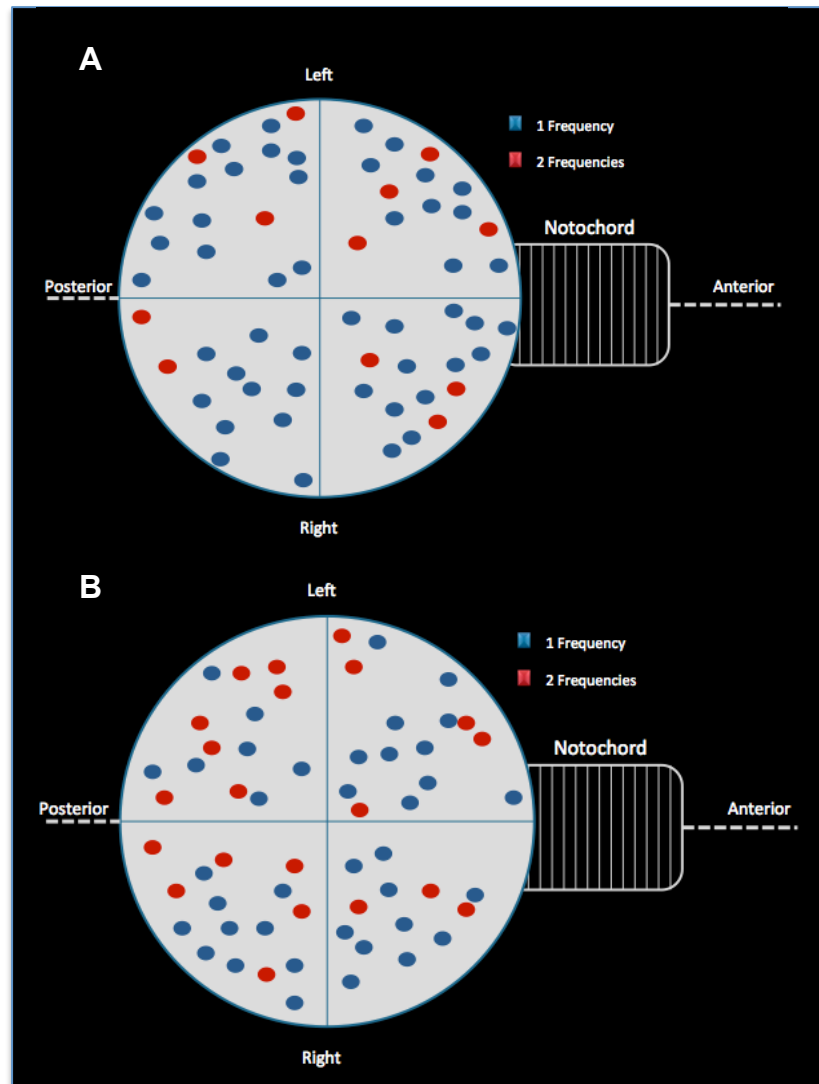


Figure 3.9 – Spatial distribution of the two motile cilia populations in the KV: A – WT cilia population and B - *deltaD*^{-/-} mutant cilia population. Blue circles mean cilia with single CBFs whereas red circles mean cilia with double CBFs. CBFs (cilia beat frequencies)

We divided the KV in four quadrants (left-posterior, left-anterior, right-posterior and right-anterior) and in two sets of 2 quadrants: one divided KV in left and right sides, and other divided KV in posterior and anterior sides. No statistical difference was found in the several quadrants ($p > 0.05$, Fisher test) for WT and *deltaD*^{-/-} mutants. Thus, we have not found any difference in the spatial distribution of the two motile cilia populations in the KV – random distribution of cilia.

3.3 High-speed videomicroscopy for measuring KV Fluid Flow

Since CBF impacts fluid flow velocity we decided to investigate the relevance of the CBF differences described between WT and *deltaD*^{-/-} mutant embryos in the KV fluid flow velocity. We measured the flow velocity by tracking naturally occurring particles that did not get trapped by cilia to avoid measuring the vortical fluid flow described by (Supatto et al. 2008).

3.3.1 Cilia Beat Frequency variations seem to affect KV vesicle fluid flow

Based on tracking naturally occurring particles inside KV, we calculated the average flow speed around the dorsal ventral axis and found that the average value was slightly increased in the *deltaD*^{-/-} mutants (from 26 $\mu\text{m/s}$ in WT to 30 $\mu\text{m/s}$ in the mutants) (Figure 3.10; $p = 0.08$, t student's test). However, more importantly, the dispersion of the flow velocity was much wider in the *deltaD*^{-/-} mutants (10-45 $\mu\text{m/s}$) compared to WT embryos (20-35 $\mu\text{m/s}$) (Figure 3.10; $p < 0.02$ – c.v.WT = 17,5 and c.v.*deltaD*^{-/-} = 28.7; Brown-Forsythe Levene's test). The counter clockwise movement of particles were confirmed as described in Kramer-Zucker et al. (Kramer-Zucker 2005). See Movie 3 in Annex III.

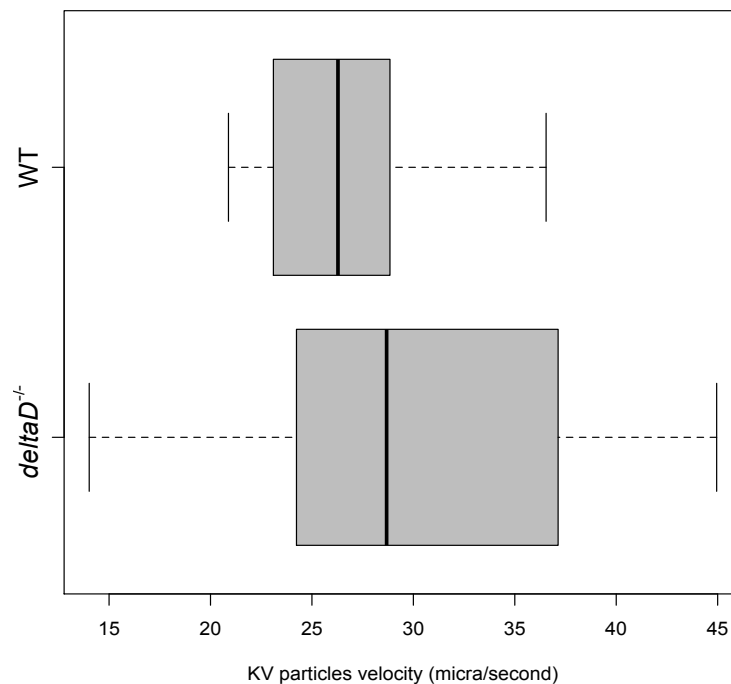


Figure 3.10 - Comparison of KV fluid flow velocity between WT and *deltaD*^{-/-} mutant embryos. WT embryos display fluid flow velocities that averaged $26 \pm 4.6 \mu\text{m/s}$ ($n_p = 18$; $n_e = 8$), whereas *deltaD*^{-/-} mutants averaged a speed of $30 \pm 8.6 \mu\text{m/s}$ ($n_p = 24$; $n_e = 5$). n_p (number of particles), n_e (number of embryos).

In the *deltaD*^{-/-} mutant KVs, the particles moved in the same direction as in the WT. In addition, the mutants showed a more variability in the KV Fluid Flow velocity. This could be related with the differences observed in CBFs analysis, although at a low Reynolds number (Re) environment, fluid flow velocities might be more influenced by the ciliary movement than by the CBFs, as dictated by 'Stokes flow'.

3.4 Molecular study on motility genes downstream of DeltaD

In order to better understand the molecular players responsible for the cilia motility defects present in *deltaD*^{-/-} mutants (Lopes et al. 2010), our lab decided to perform a tissue-specific screen using microarrays, revealing the transcriptome of the KV precursor cells. Our results showed the existence of more than 762 genes differentially expressed between WT and *deltaD*^{-/-} mutants.

This screen provided some potential candidates for the differences in CBF described above since of those 762 differentially expressed genes 3 were known to be related to cilia motility, namely *foxj1a*, *rsph3* and *dnah7*. According to the screen all the three genes were up-regulated in the *deltaD*^{-/-} KV precursor cells compared to WT. Only *foxj1a* was not found to be significantly up-regulated after the microarray statistical analysis. (*foxj1a*: $p > 0.05$; *rsph3*: $p = 0.029$; *dnah7*: $p = 0.003$)

Taking into consideration my previous characterization of distinct CBF populations and distinct KV fluid flow velocity dispersion ranges between WT and *deltaD*^{-/-} mutants, we decided to further study these cilia motility-related genes by doing quantitative real-time polymerase chain reaction (qPCR) and whole-mount *in situ* hybridization (WISH) experiments.

3.4.1 Motility related genes are differently expressed in *deltaD*^{-/-} mutants

We have started by performing WISH experiments in bud and at 8th somite-stage zebrafish embryos from WT and *deltaD*^{-/-} mutants in order to study the gene expression localization of *dnah7*, *foxj1a* and *rsph3*.

ntl gene expression was used as an experimental positive control for WISH staining at 8th somite-stage embryos. *ntl* expression was confined to the embryo's tail bud region and notochord (Figure 3.11).

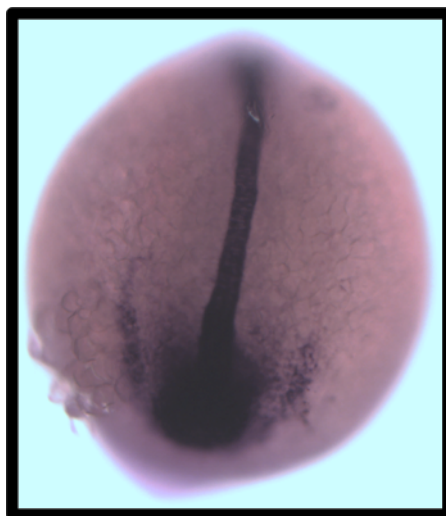


Figure 3.11 – WISH experiment for *ntl* gene in WT 8th somite-stage embryos. *ntl* gene expression was used as an experimental positive control for WISH staining in 8th somite-stage embryos.

3.4.1.1 *dnah7* gene expression

dnah7 anti-sense RNA-probe was transcribed using SP6 RNA Polymerase and the restriction enzyme Sac II. *dnah7* gene expression was restricted to the KV at 8th somite-stage WT and *deltaD*^{-/-} mutant embryos, showing a clear up-regulation in the mutants (Figure 3.12A - higher magnification in B). At bud-stage, no labelling was seen in the embryos in the expected region (KV precursor cells), maybe because *dnah7* expression levels were not sufficient for being detected by WISH experiments in that stage.

The *dnah7* sense RNA-probe, transcribed using T7 RNA Polymerase and Sac I, did not present any labelling in the KV, as expected (Figure 3.12C).

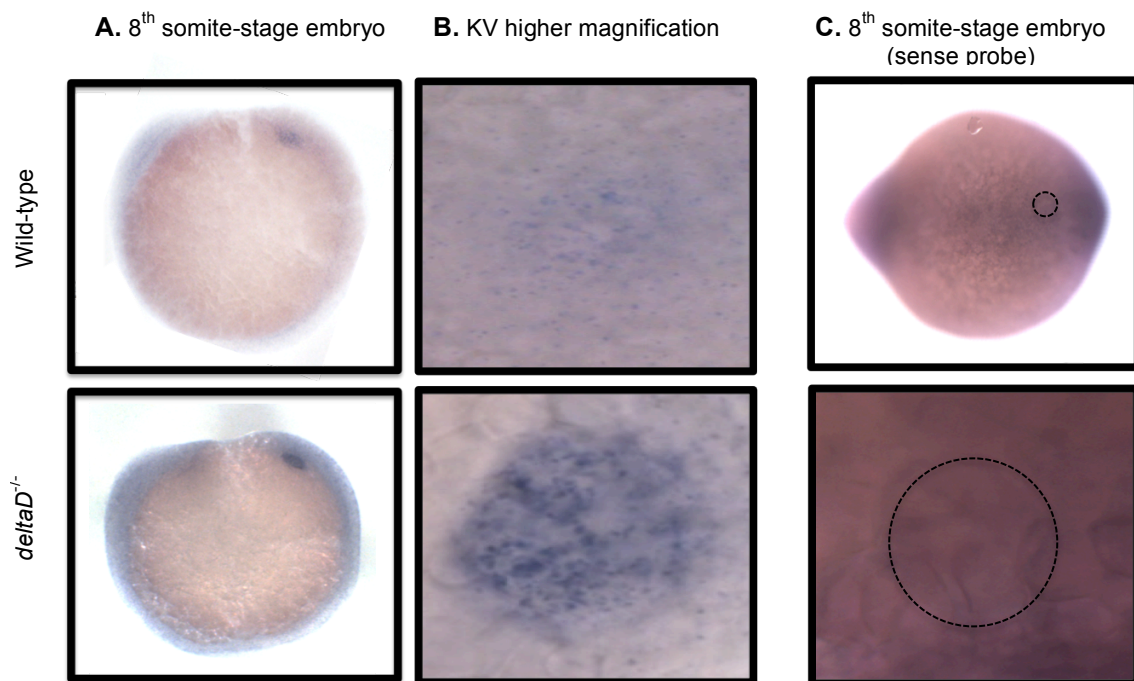


Figure 3.12 – WISH experiment for *dnah7* in WT (upper panel) and *deltaD*^{-/-} mutants at 8th somite-stage embryos (lower panel). *deltaD*^{-/-} mutant 8th somite-stage embryos showed an up-regulation of *dnah7*, whereas the WT revealed the normal expression level of *dnah7* (A). In KV higher magnification, the difference in the levels of *dnah7* expression between WT and *deltaD*^{-/-} mutant embryos was evident (B). *dnah7* sense probe was tested in 8th somite-stage embryos and no labelling in the KV was detected (C). KV is represented as a dashed circle.

3.4.1.2 *foxj1a* gene expression

foxj1a was expressed in bud-stage embryos, presenting a labelled cluster in the bud-tail region in WT and *deltaD*^{-/-} mutants. After stopping the development of the *in situ* reaction at the same time, this cluster was clearly down-regulated in the mutants (Figure 3.13A – higher magnification in B). At the KV stage (8th somites), *foxj1a* was not expressed in the KV region. Instead, its expression was restricted to the pronephros precursor cells and floor-plate (Figure 3.13C) in both WT and *deltaD*^{-/-}

mutants, as described previously by Yu et al (Yu et al. 2008). No differences in the expression levels were detected at KV stages for the two sets of embryos.

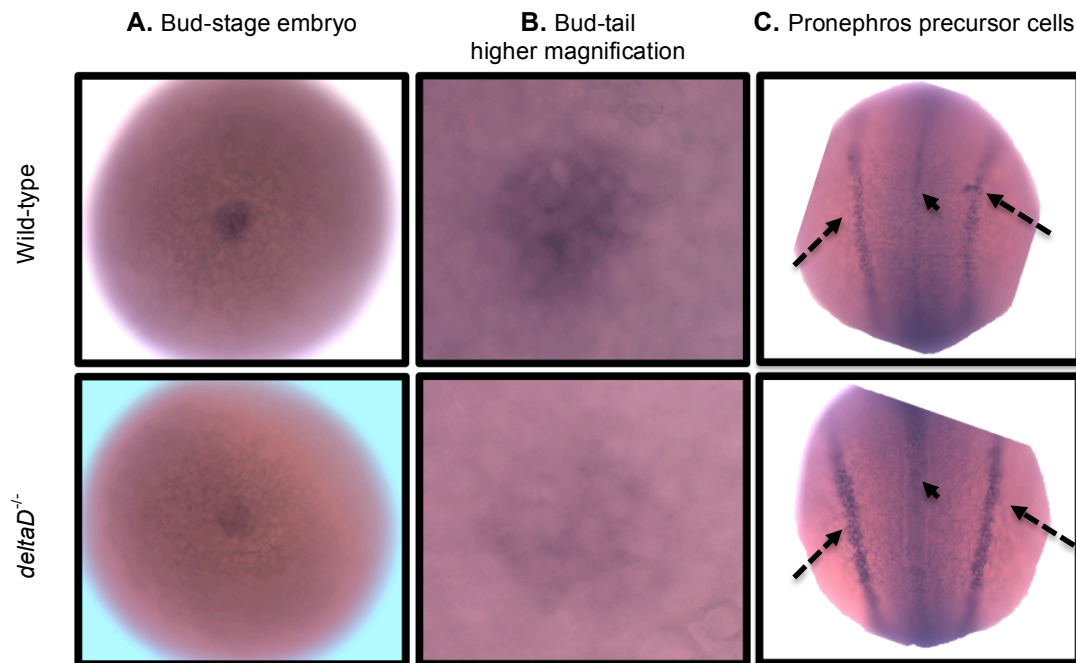


Figure 3.13 – WISH experiment for *foxj1a* in WT (upper panel) and *deltaD*^{-/-} mutants at bud-stage and 8th somite-stage embryos (lower panel). *deltaD*^{-/-} mutant bud-stage embryos showed a down regulation of *foxj1a*, whereas the WT revealed its normal expression level (A). In bud-stage higher magnification, the difference in the levels of *foxj1a* expression between WT and *deltaD*^{-/-} mutant embryos was evident (B). In 8th somite-stage embryos, *foxj1a* was not expressed at the KV but instead, the expression was localized to the pronephros precursor cells (arrows) and floor plate (arrowhead) in both sets of embryos (C).

3.4.1.3 *rsph3* gene expression

At bud-stage, *rsph3* gene expression was not detected by WISH in the expected region (KV precursor cells), maybe because its expression levels were not sufficient for being detected by WISH experiments in that stage.

However, WISH experiments in KV-stage WT and *deltaD*^{-/-} mutant embryos showed that *rsph3* gene expression was restricted to the KV and to some floor plate cells in the WT embryos whereas in the mutants was undetectable. *deltaD*^{-/-} mutant embryos did not show any *rsph3* expression in the KV and this fact could indicate the existence of active down-regulation of *rsph3* in *deltaD*^{-/-} mutants (Figure 3.14A – higher magnification in B).

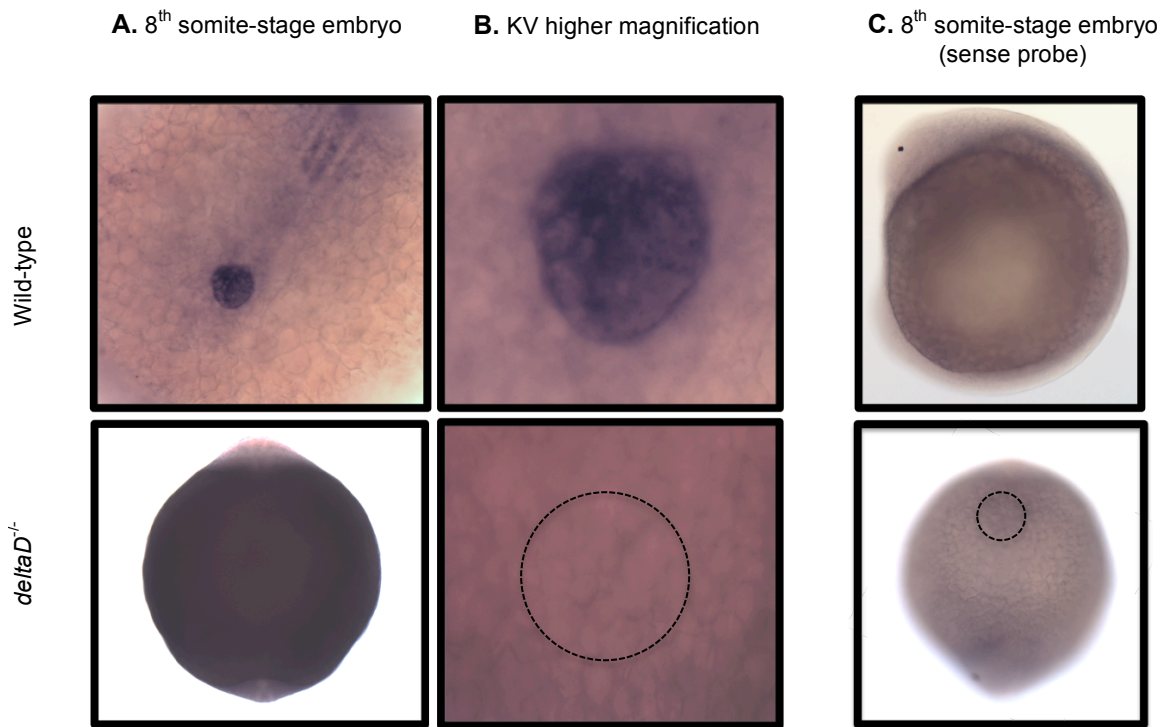


Figure 3.14 – WISH experiment for *rsph3* in Wild-type (upper panel) and *deltaD*^{-/-} mutants at 8th somite-stage embryos (lower panel). *deltaD*^{-/-} mutants with 8 somites showed a severe down regulation of *rsph3* (A and B lower panel). In contrast, in wild-type *rsph3* expression was perfectly localized to the KV (A and B upper panel). *rsph3* sense probe was tested in the same batch of 8th somite-stage embryos and no labelling was detected as expected (C). KV is represented as a dashed circle.

Altogether, the obtained results revealed some findings about the expression of the three motile-related genes. In bud-stage embryos, the expression of *dnah7* and *rsph3* were lower than the WISH detection limit. On the other hand, *foxj1a* gene expression was clearly seen at bud-stage embryos from the same batch, confirming that these embryos were intact. *foxj1a* expression presented a down regulation in *deltaD*^{-/-} mutant embryos as reported before (Lopes et al. 2010).

At 8th somite stage embryos (KV stage) *dnah7* gene expression showed an up-regulation in *deltaD*^{-/-} mutant embryos, whereas *rsph3* showed a severe down-regulation, compared to the WT gene expression. Regarding *foxj1a* this gene expression was undetected in the KV. Because some of the bud-stage expression results were different from our microarray data we decided to perform qPCR experiments as a better quantitative gene expression test.

3.4.2 Motile-related genes were up-regulated in *deltaD*^{-/-} mutants by qPCR

qPCR experiments were done using bud-stage embryos as in the microarray experiment. The obtained results showed an up-regulation of the three motile-related genes in *deltaD*^{-/-} mutant embryos (Figure 3.15). These results were concordant with the tissue-specific screen done previously in our lab, since all the three genes studied also presented an up-regulation in *deltaD*^{-/-} mutant embryos when compared to the WT. All qPCR results were normalized using *sox17* and *ef1α* as reference genes.

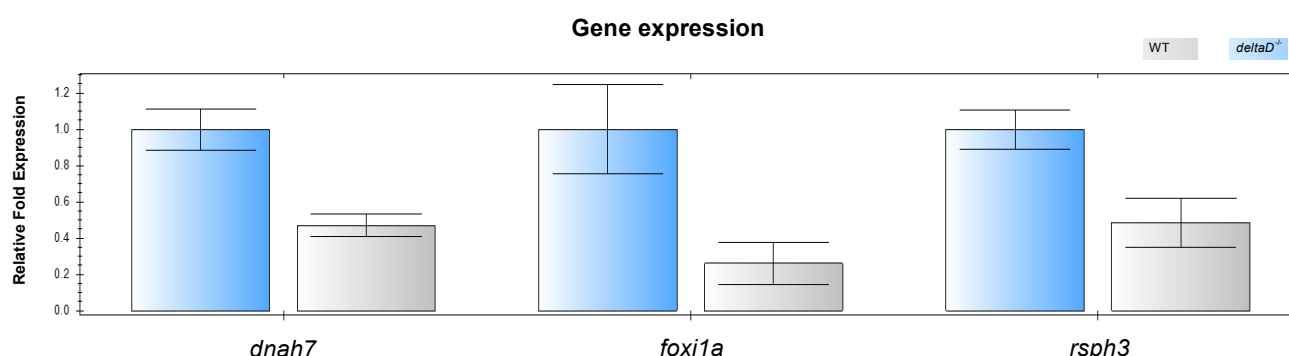


Figure 3.15 – Gene expression analysis of cilia motility-related genes by qPCR in WT and *deltaD*^{-/-} mutants. Relative Fold Expression of *dnah7*, *foxj1a* and *rsph3* in WT (grey) and *deltaD*^{-/-} (blue) bud-staged embryos by qPCR. Gene expression results were normalized by using *sox17* and *ef1α* as reference genes.

All the three genes presented an up-regulation in bud stage as results of microarray and qPCR experiments. Both techniques used bud stage embryos. In contrast to the qPCR experiment in which the whole embryos were used, for the microarray KV precursor cells were sorted in order to enrich the sample for KV specific cells. Despite this, both techniques presented the same results for the 3 motile-related gene expressions. For WISH in bud stage embryos, the obtained results were not in concordance with the microarray and qPCR. For *dnah7* and *rsph3* WISH experiments, no expression was seen in the bud stage embryos. The expression of those genes appeared later in the KV at 8th somite stage: *dnah7* confirmed the up-regulation observed by the other techniques, whereas *rsph3* showed a novel down-regulation.

Regarding *foxj1a* the WISH result was not in concordance with microarray and qPCR experiments (all done using bud stage embryos), showing a down-regulation in *deltaD*^{-/-} mutants.

Altogether these results led us to design other experiment. Because the in situ for *rsph3* and *foxj1a* bud-stage results were different from our microarray and qPCR data, we propose a time-lapse qPCR experiment in which WT and *deltaD*^{-/-} mutant embryos in 2 different developmental stages (bud-stage and 8th somite stage) will be used in order to study gene expression along the development of the zebrafish embryos.

Table 3.2 – Summary of the molecular study on motility genes downstream of DeltaD

Genes	Microarray	WISH		qPCR
	Bud stage	Bud stage	8 th somite stage	Bud stage
<i>dnah7</i>	Up	Not seen	Up	Up
<i>foxj1a</i>	Up	Down	Not seen	Up
<i>rsph3</i>	Up	Not seen	Down	Up

CHAPTER 4

Discussion

For the first time we have identified two different populations of KV motile cilia based on a careful Cilia Beat Frequency (CBF) spectral analysis. By applying Fast Fourier Transform (FFT) we were able to show that one population beats at a single frequency while the other beats at two different frequencies. Other studies (Kramer-Zucker 2005; Okabe et al. 2008; Supatto & Vermot 2011; Jaffe et al. 2010; Supatto et al. 2008) have shown zebrafish KV CBF results obtained by averaging a few random cilia (usually from 3-4 embryos). In contrast, our CBF data was generated by analysing more than 60 cilia in a total of 11 embryos for each genotype. Our reported CBF values are within the range described in the other studies (Kramer-Zucker 2005; Okabe et al. 2008; Supatto & Vermot 2011; Jaffe et al. 2010; Supatto et al. 2008), but our spectral analysis brought innovation to the study of the vertebrate organizer allowing us to identify two different types of motile cilia based on CBF distinct patterns. By using *deltaD* homozygous mutants we could manipulate the different contributions of the two motile cilia populations and observe that the dispersion of fluid flow velocity was the main parameter affected, indicating that a specific range of flow velocities may be needed to determine a functional LR patterning.

Having identified one population of cilia characterized by each cilium beating at two different frequencies we questioned if these double frequencies could result from cilia with alternating beating behaviours, like harmonic components of the beating, or from cilia beating at two different frequencies simultaneously (wobbling motion patterns^{§§§}).

After analysing more than 100 movies we found no evidence of alternating beating behaviours in the time scale analysed (1 - 10 seconds), leading us to conclude the inexistence of alternating behaviours. When confronted with the hypothesis of having a harmonic behaviour in our fundamental CBF, we found that in the cilia with double frequencies, the dominant frequency was always higher comparing with the secondary frequency. This fact allowed us to exclude that the secondary frequency could be a harmonic of the fundamental frequency leaving us with the wobbling motion as the most suited option. Figure S2 (Annex III) shows an example of one cilium beating during one second at two different frequencies simultaneously.

Cilia with wobbling motion is the way our collaborators, a group of mathematicians led by Dr. David Smith and Dr. John Blake (Birmingham University), have modelled the movement correspondent to the cilia with two frequencies we have observed experimentally. They developed the most recent KV fluid-flow model (A. A. Smith et al. 2012) and we are working together in order to further improve it. We are currently waiting for their results on how these two different populations of cilia may impact on fluid flow and whether having two CBF populations changes their previous model of flow fields in the KV (A. A. Smith et al. 2012).

We hypothesize that the two CBF populations of motile cilia may have differential contribution to the establishment of the KV flow fields and may be important to define the L-R asymmetry of the zebrafish embryo. Therefore, in this project we have performed the mapping of each cilium analysed

^{§§§} The term “wobbling” means: “to move or rotate with an uneven or rocking motion or unsteadily from side to side”.

by FFT. Our data indicated that for the > 60 cilia analysed there was not a differential spatial distribution of the two motile cilia populations in the KV (Figure 3.9), which raised the hypothesis that randomly distributed cilia showing differential CBF may impact the flow. David Smith's group is testing this hypothesis in their model (A. A. Smith et al. 2012).

We have showed that broader CBF in the mutants, results in equally wider fluid flow velocities. Knowing that *deltaD*^{-/-} mutants have gut *situs* defects (Lopes et al. 2010) it is tempting to speculate that such broader flow pattern in the mutants is less effective in promoting the correct L-R body patterning. Recently, in the KV of medaka embryos it was proposed that motile cilia have a double role, to generate nodal flow and to interpret it through mechanosensory Pkd111-Pkd2 complexes (Kamura et al. 2011). The observation that Pkd111-Pkd2 complexes are present in all motile cilia (Kamura et al. 2011) means that, in theory, any fluctuations in the fluid flow, such as the wider velocity spectrum we reported for *deltaD*^{-/-} mutants, may trigger abnormal mechanosensory responses in the KV cells which could explain why *deltaD*^{-/-} mutants have *situs* defects. One interesting experiment that will be crucial to perform in the near future will be to score the gut *situs* in the same embryos that were imaged for fluid flow measurements. In this way it will be possible to start to understand the real impact of flow velocity in L-R determination.

The discovery of cilia showing different motility patterns raised the question of whether these biophysically different populations are also molecularly and structurally different. In the mouse L-R field a similar argument currently exists - a controversy stands on whether some node motile cilia have a central pair (Caspary et al. 2007). In case this is confirmed an additional motility pattern to the one described by Okada et al. (Okada et al. 2005) could be expected in the mouse node, but so far no one has described nodal cilia that bend in a wavy pattern. Instead, all nodal cilia seem to have an almost perfect tilted conical motion (Nonaka et al. 1998; Nonaka et al. 2005). Nevertheless it is probably difficult to guess motility patterns based on axonemal structure alone.

On the other hand, in zebrafish it is commonly accepted that the KV has 9+2 motile cilia (Kreiling et al. 2007; Kramer-Zucker 2005; Supatto & Vermot 2011; Sarmah et al. 2007). Nevertheless, others have reported 9+0 and 9+2 types of cilia ultrastructure in the KV (Ferrante et al. 2009). Altogether, there is evidence that different cilia types exist in the vertebrate L-R organizer. It is our future goal to assign molecular markers to these different motility behaviours primarily described here.

One important aspect is the fact that while most of the motile cilia are structurally 9+2 in the zebrafish embryo (Kreiling et al. 2007; Kramer-Zucker 2005; Supatto & Vermot 2011; Sarmah et al. 2007), not all of them display a typical waveform motion. Supatto and Vermot (Supatto & Vermot 2011) recently revisited the types of spatially asymmetric beating patterns for motile cilia observed experimentally in zebrafish and described a 'corkscrew-like' motion in the kidney; an 'asymmetric bending' motion in the adult or embryonic epithelium in mouse and in the left-right organizer in *xenopus*; and a 'tilted conical' motion in the KV. We would like to add to these motility patterns the wobbling motion pattern we reported in our study.

We do not know what makes a cilium to wobble but it is likely to be related to its ultrastructure. Inner dyneins are described to have a role in cilia wave pattern. In our comparative molecular study of WT and mutants we found one inner dynein arm component and one radial spoke component to be deregulated in the *deltaD*^{-/-} mutants. In fact, it is described that the absence of RSP3 (zebrafish *rsph3* homologous) causes the flagella to become more rigid in *Chlamydomonas* (Kamiya 2002). Furthermore, the radial spokes do not assemble properly without RSP3 (reviewed in (Kamiya 2002)). Another study (Kamiya 2002) using *Chlamydomonas* mutants, suggested that inner dynein arms, but not outer dynein arms, are under the control of central pair microtubules and radial spokes in the axoneme of cilia and flagella. Importantly, they concluded that the axoneme presents two distinct types of beating: one involving the inner dynein arms, central pair and radial spokes; and other involving outer dynein arms alone (Kamiya 2002). We thus wonder if the deregulation of *dnah7* expression (inner dynein arm component) and *rsph3* (radial spoke component) we reported in this project may cause the drop in the population that beats with two CBFs (wobbling cilia) from 35% in the WT to 18% in the mutants. These differences are likely to be genetically encoded, since we have shown in this work that *foxj1a*, a master gene for motile cilia is affected in the *deltaD*^{-/-} mutants in agreement with a previous study (Lopes et al. 2010). We also proposed here that downstream of the DeltaD-Notch pathway there are other cilia motility genes transcriptionally deregulated. Indeed our data showed an up-regulation of *dnah7*, and a severe down-regulation of *rsph3* in the *deltaD*^{-/-} mutants. We wonder if these changes in expression may further affect the two motile cilia populations differentially and cause the change from bimodal to unimodal distribution described for cilia with a single CBF in WT and mutants, respectively.

One interesting experiment to study the contributions of *dnah7* and *rsph3* to the KV Fluid-Flow phenotype seen in WT embryos, it will be to do the knockdown of each gene separately, followed by KV fluid flow velocity analysis in the injected embryos.

Consequently, in order to see what is the contribution of *dnah7* and *rsph3* genes in the KV Fluid-Flow in a *deltaD*^{-/-} mutant background, three more interesting experiments should be done: by using *dnah7* morpholino it might be possible to rescue the *dnah7* over-expression levels observed in *deltaD* embryos, and thus study its effect on the KV Fluid-Flow velocity of *deltaD*^{-/-} mutants; other experiment would be to do the *rsph3* over-expression by injecting mRNA in *deltaD*^{-/-} mutants embryos - in this way it would be possible to study the effects of the over-expression on the KV Fluid-Flow in the mutants; the last would be the co-injection of *dnah7* morpholino (performing the knockdown) and *rsph3* mRNA (performing the over-expression) in the same mutant embryos. For all the three experiments described, we expect the velocity dispersion to decrease, rescuing the velocity ranges seen for the mutant embryos.

Nothing is described in humans or animal models regarding the over-expression of *dnah7* or of any dynein gene. Mutations reported in ciliary motility genes usually lead to loss-of-function phenotypes (Armengot et al. 2012; Bartoloni et al. 2001; O'Callaghan et al. 2011; Loges et al. 2008; Mitchison et al. 2012; Panizzi et al. 2012). Nevertheless, so far, only one case of a PCD patient is associated with the absence of DNAH7 protein (Y. J. Zhang 2002). This patient had absence of inner dynein arms in

the ciliary axonemes, evaluated by electron microscopy. According to Zhang et al. (Y. J. Zhang 2002) DNAH7 was undetectable in cilia from cells taken from the PCD patient, whereas intracellular DNAH7 was abnormally present, showing that DNAH7 was synthesized but not assembled in this individual case of PCD (Y. J. Zhang 2002). In this study (Y. J. Zhang 2002), the PCD patient diagnostic was given based on an axonemal defect seen by electron microscopy – the absence of the inner dynein arm. Another recent study (Theegarten & Ebsen 2011) showed that in a large series of PCD patients, the dominant ultrastructural defects in PCD cilia were related to inner dynein arms. A variety of defects were reported, ranging from the total loss of inner dynein arms to a rudimentary structure resembling it. Nevertheless, the complete loss of inner dynein arms was very common (found in 75.2% of the PCD cases) (Theegarten & Ebsen 2011). Nevertheless, these PCD cilia were still motile but the CBF and cilia pattern were affected the inner dynein arms are needed for the motile cilia proper bending (Merveille et al. 2010).

The relevance of studying *deltaD*^{-/-} mutants is due to the fact that they present a deregulation on the expression of an inner dynein arm component that might influence the ciliary motility, and a CBF phenotype that presents differences compared to the WT (see section 3.1 in Chapter 3). Merveille et al. (Merveille et al. 2010) studied mutations on CCDC39 (axonemal protein) whose absence results in the failure of the correct assemble of inner dynein arms and radial spoke complexes, thereby causing axonemal disorganization and dyskinetic beating. So far we can not prove that *dnha7* and *rsph3* are responsible for the CBF differences observed in this study, but previous studies (Merveille et al. 2010; E. F. Smith & Yang 2004; Stannard et al. 2010; Theegarten & Ebsen 2011; Loges et al. 2009) support our guess in thinking that they might be important for the motile cilia axoneme to beat properly.

At present, several groups (Lucas et al. 2011; Jackson et al. 2012; Armengot et al. 2012; Stannard et al. 2010; Shoemark et al. 2012) are trying to develop the gold-standard method to diagnose PCD properly, since cilia motility and structure can vary between patients, making the diagnosis difficult. A PCD diagnostic based only on potential ultrastructural defects is limited and not accurate (Bush et al. 2007; Robert et al. 2007). At present, medical guidelines for PCD diagnose include the CBF analysis, using high-resolution and high-speed digital videomicroscopy, as a screening method before electron microscopy analysis (Armengot et al. 2012; Green et al. 1993; Armengot et al. 2012; Jackson et al. 2012). This system of video analysis is more useful than the ultrastructural study and mucociliary transport for PCD screening, since electron microscopy analysis can confirm but do not always exclude a diagnosis of PCD (Armengot et al. 2012; Shoemark et al. 2012). According with Stannard et al. (Stannard et al. 2010), the use of CBF alone to screen which biopsies should follow for electron microscopy, results in a significant number of missed diagnoses. This group showed that ciliary beat pattern analysis is more sensitive and specific for PCD than CBF alone, since some PCD patients could have a CBF value expected for a healthy person, but their cilia beat in a dyskinetic fashion (Stannard et al. 2010). In summary, at present the PCD patient's diagnostic includes CBF and beat pattern analysis using high-speed videomicroscopy, followed by an electron microscopy analysis for potential ultrastructural defects. It takes considerably more time but the rate of missed diagnoses have been decreasing dramatically (Stannard et al. 2010).

The coexistence of PCD and situs defects has a frequency between 40% and 50% among patients with PCD (Armengot et al. 2012; Shoemark et al. 2012; Merveille et al. 2010), reason why is highly relevant to study the basic mechanisms involved in L-R defects. Cilia motility abnormalities and dynein arms defects can be the basis of situs problems in PCD (Loges et al. 2009; Loges et al. 2008). Papon et al. (Papon et al. 2010) studied PCD situs patients with normal ciliary ultrastructure, and recommended the analysis of CBF and cilia pattern, as we described previously. As it is impossible to study CBF of human nodal cilia and relate it to PCD patient *situs* we suggest that CBF should be more carefully characterized in model organisms. Especially, in L-R mutants that do not have obvious cilia structural defects, as these could be potential new models for PCD (Kunimoto et al. 2012; Lechtreck et al. 2008; Norris & Grimes 2012; Lucas et al. 2011).

References

- Afzelius, B.A., 1995. Situs inversus and ciliary abnormalities. What is the connection? *The International Journal of Developmental Biology*, 39(5), pp.839–844.
- Afzelius, B.A.B., 2004. Cilia-related diseases. *Journal of Pathology*, 204(4), pp.470–477.
- Amack, J.D., Wang, X. & Yost, H.J., 2007. Two T-box genes play independent and cooperative roles to regulate morphogenesis of ciliated Kupffer's vesicle in zebrafish. *Developmental Biology*, 310(2), pp.196–210.
- Armengot, M. et al., 2012. Development and Validation of a Method of Cilia Motility Analysis for the Early Diagnosis of Primary Ciliary Dyskinesia. *Acta Otorrinolaringologica (English Edition)*, 63(1), pp.1–8. Available at: <http://linkinghub.elsevier.com/retrieve/pii/S2173573512000129>.
- Badano, J.L. et al., 2006. The ciliopathies: an emerging class of human genetic disorders. *Annual review of genomics and human genetics*, 7, pp.125–148.
- Bartoloni, L. et al., 2001. Axonemal Beta Heavy Chain Dynein DNAH9: cDNA Sequence, Genomic Structure, and Investigation of Its Role in Primary Ciliary Dyskinesia. *Genomics*, 72(1), pp.21–33.
- Bloodgood, R.A., 2010. Sensory reception is an attribute of both primary cilia and motile cilia. *Journal of Cell Science*, 123(4), pp.505–509.
- Bonnafe, E.E. et al., 2004. The transcription factor RFX3 directs nodal cilium development and left-right asymmetry specification. *Molecular and Cellular Biology*, 24(10), pp.4417–4427.
- Borovina, A. et al., 2010. Vangl2 directs the posterior tilting and asymmetric localization of motile primary cilia. *Nature Publishing Group*, 12(4), pp.407–412.
- Brennan, J.J., Norris, D.P.D. & Robertson, E.J.E., 2002. Nodal activity in the node governs left-right asymmetry. *Genes & development*, 16(18), pp.2339–2344.
- Brody, S.L.S. et al., 2000. Ciliogenesis and left-right axis defects in forkhead factor HFH-4-null mice. *American Journal of Respiratory Cell and Molecular Biology*, 23(1), pp.45–51.
- Brummett, A.R.A. & Dumont, J.N.J., 1978. Kupffer's vesicle in *Fundulus heteroclitus*: a scanning and transmission electron microscope study. *Tissue and Cell*, 10(1), pp.11–22.
- Buceta, J.J. et al., 2005. Nodal cilia dynamics and the specification of the left/right axis in early vertebrate embryo development. *Biophysical Journal*, 89(4), pp.2199–2209.
- Bush, A.A. et al., 2007. Primary ciliary dyskinesia: current state of the art. *Audio, Transactions of the IRE Professional Group on*, 92(12), pp.1136–1140.
- Cartwright, J.H.E. et al., 2006. Embryonic nodal flow and the dynamics of nodal vesicular parcels. *Journal of The Royal Society Interface*, 4(12), pp.49–55.

- Cartwright, J.H.E., Piro, O. & Tuval, I., 2008. Fluid dynamics in developmental biology: moving fluids that shape ontogeny. *HFSP Journal*, pp.1–17.
- Caspary, T., Larkins, C.E. & Anderson, K.V., 2007. The Graded Response to Sonic Hedgehog Depends on Cilia Architecture. *Developmental Cell*, 12(5), pp.767–778. Available at: <http://linkinghub.elsevier.com/retrieve/pii/S1534580707001049>.
- Castleman, V.H. et al., 2009. Mutations in radial spoke head protein genes RSPH9 and RSPH4A cause primary ciliary dyskinesia with central-microtubular-pair abnormalities. *American journal of human genetics*, 84(2), pp.197–209.
- Chen, J.J. et al., 1998. Mutation of the mouse hepatocyte nuclear factor/forkhead homologue 4 gene results in an absence of cilia and random left-right asymmetry. *Journal of Clinical Investigation*, 102(6), pp.1077–1082.
- Colantonio, J.R. et al., 2009. The dynein regulatory complex is required for ciliary motility and otolith biogenesis in the inner ear. *Nature*, 457(7226), pp.205–209.
- Cole, D.G. et al., 1998. Chlamydomonas kinesin-II-dependent intraflagellar transport (IFT): IFT particles contain proteins required for ciliary assembly in *Caenorhabditis elegans* sensory neurons. *Journal of Cell Biology*, 141(4), pp.993–1008.
- Dentler, W.W., Vanderwaal, K.K. & Porter, M.E.M., 2009. Recording and analyzing IFT in *Chlamydomonas* flagella. *Methods in Cell Biology*, 93, pp.145–155.
- Edelstein, A. et al., 2001. *Current Protocols in Molecular Biology* F. M. Ausubel et al., eds., Hoboken, NJ, USA: John Wiley & Sons, Inc. Available at: <http://doi.wiley.com/10.1002/0471142727.mb1420s92>.
- Ellerman, A.A. & Bisgaard, H.H., 1997. Longitudinal study of lung function in a cohort of primary ciliary dyskinesia. *European Respiratory Journal*, 10(10), pp.2376–2379.
- Essner, J.J., 2005. Kupffer's vesicle is a ciliated organ of asymmetry in the zebrafish embryo that initiates left-right development of the brain, heart and gut. *Development*, 132(6), pp.1247–1260.
- Ferrante, M.I. et al., 2009. Convergent extension movements and ciliary function are mediated by *ofd1*, a zebrafish orthologue of the human oral-facial-digital type 1 syndrome gene. *Human Molecular Genetics*, 18(2), pp.289–303.
- Field, S.S. et al., 2011. *Pkd1l1* establishes left-right asymmetry and physically interacts with *Pkd2*. *Development*, 138(6), pp.1131–1142.
- Fliegauf, M., Benzing, T. & Omran, H., 2007. When cilia go bad: cilia defects and ciliopathies. *Nature reviews. Molecular cell biology*, 8(11), pp.880–893.
- Francescatto, L. et al., 2010. The activation of membrane targeted CaMK-II in the zebrafish Kupffer's vesicle is required for left-right asymmetry . pp.1–10.
- Freund, J.B. et al., 2012. Fluid flows and forces in development: functions, features and biophysical

- principles. *Development*, 139(7), pp.1229–1245. Available at: <http://eutils.ncbi.nlm.nih.gov/entrez/eutils/elink.fcgi?dbfrom=pubmed&id=22395739&retmode=ref&cmd=prlinks>.
- Goetz, S.C.S. & Anderson, K.V.K., 2010. The primary cilium: a signalling centre during vertebrate development. *Audio, Transactions of the IRE Professional Group on*, 11(5), pp.331–344.
- Green, A. et al., 1993. Computerized measurement of ciliary beat frequency
. *Journal of Medical Engineering & Technology*, pp.1–6.
- Guerrero, A. et al., 2011. Strategies for locating the female gamete: the importance of measuring sperm trajectories in three spatial dimensions. *Molecular Human Reproduction*, 17(8), pp.511–523.
- Hamada, 2008. Breakthroughs and future challenges in left-right patterning. *Development Growth & Differentiation*, 50 Suppl 1, pp.S71–S78.
- Hellemans, J. et al., 2007. qBase relative quantification framework and software for management and automated analysis of real-time quantitative PCR data. *Genome Biology*, 8(2), p.R19.
- Hirokawa, N., Tanaka, Y. & Okada, Y., 2009. Left-right determination: involvement of molecular motor KIF3, cilia, and nodal flow. *Cold Spring Harbor perspectives in biology*, 1(1), p.a000802.
- Hojo, M. et al., 2007. Right-elevated expression of charon is regulated by fluid flow in medaka Kupffer's vesicle. *Development Growth & Differentiation*, 49(5), pp.395–405.
- Jackson, C.L., Goggin, P.M. & Lucas, J.S., 2012. Ciliary beat pattern analysis below 37°C may increase risk of primary ciliary dyskinesia misdiagnosis. *Chest*, 142(2), pp.543–544.
- Jaffe, K.M. et al., 2010. *Chapter 22 - Imaging Cilia in Zebrafish*, Elsevier Inc.
- Jivan, A. et al., 2009. Radial spoke protein 3 is a mammalian protein kinase A-anchoring protein that binds ERK1/2. *The Journal of biological chemistry*, 284(43), pp.29437–29445.
- Jorissen, M.M., Bertrand, B.B. & Eloy, P.P., 1997. Ciliary dyskinesia in the nose and paranasal sinuses. *Acta Oto-Rhino-Laryngologica Belgica*, 51(4), pp.353–366.
- Kamiya, R., 2002. Functional diversity of axonemal dyneins as studied in Chlamydomonas mutants. *International review of cytology*, 219, pp.115–155.
- Kamura, K. et al., 2011. Pkd1l1 complexes with Pkd2 on motile cilia and functions to establish the left-right axis. *Development*, 138(6), pp.1121–1129.
- Kimmel, C. et al., 1995. Stages of Embryonic Development of the Zebrafish. *Developmental Dynamics*, pp.253–310.
- Kobayashi, T. et al., 2011. Centriolar Kinesin Kif24 Interacts with CP110 to Remodel Microtubules and Regulate Ciliogenesis. *Cell*, 145(6), pp.914–925.
- Kramer-Zucker, A.G., 2005. Cilia-driven fluid flow in the zebrafish pronephros, brain and Kupffer's vesicle

- is required for normal organogenesis. *Development*, 132(8), pp.1907–1921.
- Kreiling, J.A. et al., 2007. Analysis of Kupffer's vesicle in zebrafish embryos using a cave automated virtual environment. *Developmental Dynamics*, 236(7), pp.1963–1969. Available at: <http://doi.wiley.com/10.1002/dvdy.21191>.
- Kunimoto, K. et al., 2012. Coordinated Ciliary Beating Requires Odf2-Mediated Polarization of Basal Bodies via Basal Feet. *Cell*, 148(1-2), pp.189–200.
- Lechtreck, K.-F. et al., 2008. Mutations in Hydin impair ciliary motility in mice. *the journal of cell biology*, 180(3), pp.633–643.
- Lee, J.D.J. & Anderson, K.V.K., 2008. Morphogenesis of the node and notochord: the cellular basis for the establishment and maintenance of left-right asymmetry in the mouse. *Developmental Dynamics*, 237(12), pp.3464–3476.
- Loges, N.T. et al., 2009. Deletions and Point Mutations of LRRC50 Cause Primary Ciliary Dyskinesia Due to Dynein Arm Defects. *The American Journal of Human Genetics*, 85(6), pp.883–889.
- Loges, N.T. et al., 2008. DNAI2 Mutations Cause Primary Ciliary Dyskinesia with Defects in the Outer Dynein Arm. *The American Journal of Human Genetics*, 83(5), pp.547–558.
- Lopes, S.S. et al., 2010. Notch signalling regulates left-right asymmetry through ciliary length control. *Development*, 137(21), pp.3625–3632.
- Lucas, J.S. et al., 2011. Static respiratory cilia associated with mutations in Dnahc11/DNAH11: A mouse model of PCD. *Human Mutation*, 33(3), pp.495–503.
- Marshall, W.F., 2008. The cell biological basis of ciliary disease. *the journal of cell biology*.
- Marshall, W.F.W. & Nonaka, S.S., 2006. Cilia: tuning in to the cell's antenna. *Current Biology*, 16(15), pp.R604–R614.
- McGrath, J., 2003. Cilia are at the heart of vertebrate left–right asymmetry. *Current Opinion in Genetics & Development*, 13(4), pp.385–392.
- McGrath, J. et al., 2003. Two Populations of Node Monocilia Initiate Left-Right Asymmetry in the Mouse. *Cell*, 114(1), pp.61–73.
- Meijering, E., Dzyubachyk, O. & Smal, I., 2012. Methods for Cell and Particle Tracking. *Methods in enzymology*, 504(Imaging and Spectroscopic analysis of Living Cells), pp.183–200.
- Merveille, A.-C. et al., 2010. CCDC39 is required for assembly of inner dynein arms and the dynein regulatory complex and for normal ciliary motility in humans and dogs. *Nature Publishing Group*, 43(1), pp.72–78.
- Mitchison, H.M. et al., 2012. Mutations in axonemal dynein assembly factor DNAAF3 cause primary ciliary dyskinesia. *Nature Publishing Group*, 44(4), pp.381–389.
- Nauli, S.M.S. et al., 2003. Polycystins 1 and 2 mediate mechanosensation in the primary cilium of kidney

- cells. *Nature Genetics*, 33(2), pp.129–137.
- Nicastro, D. et al., 2011. Cryo-electron tomography reveals conserved features of doublet microtubules in flagella
- D. Nicastro et al., eds. *PNAS*, pp.1–9.
- Nonaka, S. et al., 2005. De novo formation of left-right asymmetry by posterior tilt of nodal cilia. *PLoS Biology*, 3(8), pp.e268–e268.
- Nonaka, S. et al., 2002. Determination of left-right patterning of the mouse embryo by artificial nodal flow. *Nature*, 418(6893), pp.96–99.
- Nonaka, S.S. et al., 1998. Randomization of left-right asymmetry due to loss of nodal cilia generating leftward flow of extraembryonic fluid in mice lacking KIF3B motor protein. *Cell*, 95(6), pp.829–837.
- Norris, D.P. & Grimes, D.T., 2012. Mouse models of ciliopathies: the state of the art. *Disease models & mechanisms*, 5(3), pp.299–312.
- O'Callaghan, C. et al., 2011. Inner dynein arm defects causing primary ciliary dyskinesia: repeat testing required. *The European respiratory journal : official journal of the European Society for Clinical Respiratory Physiology*, 38(3), pp.603–607.
- Okabe, N., Xu, B. & Burdine, R.D., 2008. Fluid dynamics in zebrafish Kupffer's vesicle. *Developmental Dynamics*, 237(12), pp.3602–3612.
- Okada, Y. et al., 2005. Mechanism of nodal flow: a conserved symmetry breaking event in left-right axis determination. *Cell*, 121(4), pp.633–644.
- Olm, M.A.K. et al., 2011. Primary ciliary dyskinesia: evaluation using cilia beat frequency assessment via spectral analysis of digital microscopy images. *Journal of Applied Physiology*, 111(1), pp.295–302.
- Panizzi, J.R.J. et al., 2012. CCDC103 mutations cause primary ciliary dyskinesia by disrupting assembly of ciliary dynein arms. *Nature Genetics*, 44(6), pp.714–719.
- Papon, J.F. et al., 2010. A 20-year experience of electron microscopy in the diagnosis of primary ciliary dyskinesia. *European Respiratory Journal*, 35(5), pp.1057–1063. Available at: <http://eutils.ncbi.nlm.nih.gov/entrez/eutils/elink.fcgi?dbfrom=pubmed&id=19840971&retmode=ref&cmd=prlinks>.
- Pazour, G.J. et al., 2000. Chlamydomonas IFT88 and its mouse homologue, polycystic kidney disease gene tg737, are required for assembly of cilia and flagella. *Journal of Cell Biology*, 151(3), pp.709–718.
- Piperno, G.G. & Mead, K.K., 1997. Transport of a novel complex in the cytoplasmic matrix of Chlamydomonas flagella. *PNAS*, 94(9), pp.4457–4462.
- Robert, A. et al., 2007. The intraflagellar transport component IFT88/polaris is a centrosomal protein regulating G1-S transition in non-ciliated cells. *Journal of Cell Science*, 120(5), pp.918–918.

- Sarmah, B. et al., 2007. A role for the inositol kinase Ipk1 in ciliary beating and length maintenance. *Proceedings of the National Academy of Sciences*, 104(50), pp.19843–19848.
- Schwabe, G.C. et al., 2008. Primary ciliary dyskinesia associated with normal axoneme ultrastructure is caused by DNAH11 mutations. *Human Mutation*, 29(2), pp.289–298. Available at: <http://gateway.webofknowledge.com/gateway/Gateway.cgi?GWVersion=2&SrcAuth=mekentosj&SrcApp=Papers&DestLinkType=FullRecord&DestApp=WOS&KeyUT=000253033000012>.
- Schweickert, A. et al., 2007. Cilia-driven leftward flow determines laterality in *Xenopus*. *Current Biology*, 17(1), pp.60–66.
- Shah, A.S. et al., 2009. Motile cilia of human airway epithelia are chemosensory. *Science*, 325(5944), pp.1131–1134.
- Shiratori, H. & Hamada, H., 2006. The left-right axis in the mouse: from origin to morphology. *Development*, 133(11), pp.2095–2104.
- Shoemark, A. et al., 2012. Twenty-year review of quantitative transmission electron microscopy for the diagnosis of primary ciliary dyskinesia. *Journal of clinical pathology*, 65(3), pp.267–271. Available at: <http://eutils.ncbi.nlm.nih.gov/entrez/eutils/elink.fcgi?dbfrom=pubmed&id=22135026&retmode=ref&cmd=prlinks>.
- Silva, I.A.L., Cancela, M.L. & Conceição, N., 2011. Molecular cloning and expression analysis of xpd from zebrafish (*Danio rerio*). *Molecular Biology Reports*, 39(5), pp.5339–5348.
- Singla, V. & Reiter, J.F., 2006. The primary cilium as the cell's antenna: signaling at a sensory organelle. *Science*, 313(5787), pp.629–633.
- Smith, A.A. et al., 2012. Symmetry breaking cilia-driven flow in the zebrafish embryo. *Journal of Fluid Mechanics*, 705, pp.26–45.
- Smith, D.J., Blake, J.R. & Gaffney, E.A., 2008. Fluid mechanics of nodal flow due to embryonic primary cilia. *Journal of the Royal Society*, pp.1–8.
- Smith, D.J., Smith, A.A. & Blake, J.R., 2010. Mathematical embryology: the fluid mechanics of nodal cilia. *Journal of Engineering Mathematics*, 70(1-3), pp.255–279.
- Smith, E.F. & Yang, P., 2004. The radial spokes and central apparatus: mechano-chemical transducers that regulate flagellar motility. *Cell Motility and the Cytoskeleton*, 57(1), pp.8–17.
- Stannard, W.A. et al., 2010. Diagnostic testing of patients suspected of primary ciliary dyskinesia. *American journal of respiratory and critical care medicine*, 181(4), pp.307–314.
- Sulik, K. et al., 1994. Morphogenesis of the murine node and notochordal plate. *Developmental Dynamics*, 201(3), pp.260–278.
- Supatto, W. & Vermot, J., 2011. *From Cilia Hydrodynamics to Zebrafish Embryonic Development* 1st ed, Elsevier Inc.
- Supatto, W., Fraser, S.E. & Vermot, J., 2008. An All-Optical Approach for Probing Microscopic Flows in

- Living Embryos. *Biophysical Journal*, 95(4), pp.L29–L31.
- Tabin, C.J. & Vogan, K.J., 2003. A two-cilia model for vertebrate left-right axis specification. *Genes & development*, 17(1), pp.1–6.
- Tanaka, Y., Okada, Y. & Hirokawa, N., 2005. FGF-induced vesicular release of Sonic hedgehog and retinoic acid in leftward nodal flow is critical for left–right determination. *Nature Publishing Group*, pp.1–6.
- Taylor, S. et al., 2010. A practical approach to RT-qPCR—Publishing data that conform to the MIQE guidelines. *Methods*, 50(4), pp.S1–S5.
- Theegarten, D. & Ebsen, M., 2011. Ultrastructural pathology of primary ciliary dyskinesia: report about 125 cases in Germany. *Diagnostic Pathology*, 6(1), p.115.
- Thisse, C. & Thisse, B., 2008. High-resolution in situ hybridization to whole-mount zebrafish embryos. *Nature Protocols*, 3(1), pp.59–69.
- Vandesompele, J. et al., 2002. Accurate normalization of real-time quantitative RT-PCR data by geometric averaging of multiple internal control genes. *Genome Biology*, pp.1–12.
- Vilfan, M. et al., 2012. Analysis of fluid flow around a beating artificial cilium. *Beilstein Journal of Nanotechnology*, 3, pp.163–171.
- Vincensini, L., Blisnick, T. & Bastin, P., 2011. 1001 model organisms to study cilia and flagella. *Biology of the Cell*, 103(3), pp.109–130.
- Vogan, K.J. & Tabin, C.J., 1999. A new spin on handed asymmetry. *Nature*, 397(6717), pp.295–297–8.
- Yu, X. et al., 2008. Foxj1 transcription factors are master regulators of the motile ciliogenic program. *Nature Genetics*, 40(12), pp.1445–1453.
- Zhang, M.M. et al., 2004. Foxj1 regulates asymmetric gene expression during left-right axis patterning in mice. *Biochemical and Biophysical Research Communications*, 324(4), pp.1413–1420.
- Zhang, Y.J., 2002. Identification of Dynein Heavy Chain 7 as an Inner Arm Component of Human Cilia That Is Synthesized but Not Assembled in a Case of Primary Ciliary Dyskinesia. *Journal of Biological Chemistry*, 277(20), pp.17906–17915.

Annex I

Data lists to R program

Wild-type CBF data

Single CBF list

35.8	25.1	30	30.9	24.2	34.8	25.2	25.8	24.8	25.9	34.9
38.6	37.7	40.8	39.7	41.1	41.2	19.8	20.8	25.8	25.8	27.8
22.8	27.8	39.7	36.7	23.8	35.7	37.7	38.6	29.8	38.7	37.8
40.6	38.8	39.7	39.6	32.7						

Double CBF list

1st	29	26.1	34.8	33.8	35.8	38.6	39.7	41	42.3	36.6	37.7	37.8
	20.9	38.6	27.7	35.6	36.7	35.7	40.7	39.8	40.6			
2nd	32.8	39.7	21.3	23.2	21.9	15.8	9.7	11	12.4	18.8	16.9	17.9
	4	16.8	24.7	20.8	20.8	20.8	10.9	12.9	11.9			

deltaD^{-/-} mutant CBF data

Single CBF list

24.2	23.2	23.2	24.3	23.3	27.7	26.8	26.8	31.6	24.8	23.8
22.8	22.8	23.8	23.8	33.1	28.2	28.2	28.2	26.2	26.2	30.1
30.1	29.1	32.8	32.8	32.8	30.8	30.8	30.7	30.7	34.7	33.7
36.7	35.8	26.8	40.7	26.8	38.7	26.8	26.8	24.8	33.5	21.9
18.9	21.9	18.9								

Double CBF list

1st	20.9	28.8	24.9	15.9	20.9	16.9	12	40.7	26.8	26.8	40.7	40.7
2nd	17.9	9	29.9	25.9	16.9	11	18.9	10.9	40.7	14.9	10.9	10.9

Wild-type KV velocity data

28.84641579	25.26088433	27.55285063	28.06303803	28.17347044
24.06883075	23.85007867	27.30567998	21.30066644	23.09999256
20.95458366	34.50257338	36.54288071	20.97601623	
20.88517725	30.68195761	23.19204068	29.52087529	

deltaD^{-/-} mutant KV velocity data

23.04172885	28.54334889	43.87047562	22.87523185	34.07132741
34.53758804	33.74795382	39.20943959	14.71665342	14.02125867
40.16925178	27.89073938	37.5604796	24.33843402	18.1940659
44.9510663	24.13766315	36.71033386	40.03247218	26.63505758
29.1941505	28.82002456	27.96398384	24.97448073	

Annex II

Scripts to R program

Fast Fourier Transform (FFT) function

```
peaks <- function(series,span=3)
{
  z <- embed(series, span)
  s <- span%%2
  v <- max.col(z, "first") == 1 + s # take first if a tie
  result <- c(rep(FALSE,s),v)
  result <- result[1:(length(result)-s)]
  result
}

filterTimeSeries<- function(timeSeries, LowFreqRange, HighFreqRange, end, timeScale)
{
  layout(matrix(c(1,2,3,4), 2, 2, byrow = TRUE))
  data.freqDomain<-fft(timeSeries)

  frequency<- c( 1:length(Mod(data.freqDomain)) )
  frequency<- frequency/length(data.freqDomain)
  frequency<- frequency/timeScale
  plot(frequency, Mod(data.freqDomain), type = "l", main = "Re Frequency domain", xlab = "Beat frequency
(Hz)", ylab ="Power", xlim = c(0,frequency[length(frequency)/2]))

  data.freqDomain[HighFreqRange] <- 0 + 0i
  #print(HighFreqRange)
  HighFreqRange2 <- rev(HighFreqRange)
  #print(HighFreqRange2)
  HighFreqRange2 <- length(timeSeries) - HighFreqRange2[1:length(HighFreqRange2)] + 1
  #print(HighFreqRange2)
  data.freqDomain[HighFreqRange2] <- 0 + 0i
```

```

data.freqDomain[LowFreqRange] <- 0 + 0i
#print(LowFreqRange)
LowFreqRange2 <- rev(LowFreqRange)
#print(LowFreqRange2)
LowFreqRange2 <- length(timeSeries) - LowFreqRange2[1:length(LowFreqRange2)] + 1
#print(LowFreqRange2)
data.freqDomain[LowFreqRange2] <- 0 + 0i

#identification of max peaks
ts.f<-Mod(data.freqDomain[1:(length(frequency)/2)])
pks  <- peaks( ts.f, span=5)
fq.max<-frequency[1:(length(frequency)/2)]
fq.max<-fq.max[pks]; fq.max
fq.max<-round(fq.max,1)

y.peaks<-ts.f[pks]
y.max<-y.peaks[which(y.peaks>4)]

x.max<-fq.max[which(y.peaks>4)]
vals<-data.frame(Max.Freq = x.max, Power = round(y.max, 1))

vals<- vals[order(-vals[,2]),]
print(vals)
plot(frequency[1:length(frequency)/2], Mod(data.freqDomain[1:length(frequency)/2]), type = "b",
main = "Re Frequency domain filtered", xlab = "Beat frequency (Hz)", ylab ="Power", xlim =
c(1,frequency[length(frequency)/2]), ylim = c(0,20))
abline(v=x.max, col = "red")
if(length(x.max>0)) text(x.max+ 5, y.max +1, paste (x.max, "Hz"), col = "red")
data.timeDomain <- fft(data.freqDomain, inverse = TRUE)
data.timeDomain <- data.timeDomain/length(data.freqDomain)
data.timeDomain <- Mod(data.timeDomain)

```

```

time <- c(1:length(data.timeDomain))*timeScale
plot(time,timeSeries, type = "l",
      main = "Time domain", xlab = "time (s)", ylab ="intensity")
plot(time,data.timeDomain, type = "l",
      main = "Time domain filtered", xlab = "time (s)", ylab ="intensity")
#return(data.timeDomain)
beatFreq <- cbind(frequency ,Mod(data.freqDomain))
return (beatFreq)
}

plotSelectedFreqDomain<- function(timeSeries, XLIM)
{
  layout(1)
  data.freqDomain<-fft(timeSeries)
  plot(Mod(data.freqDomain[XLIM]), type = "l",
       main = "Frequency domain filtered", xlab = "Frequency", ylab ="Power")
}

readData<-function(filename,totalTime, range)
{
  data <- read.table(filename, skip =1)
  #data
  colnames(data)<- c("t","f")
  colnames(data)
  #plot(data$f, type ="l")

  sampling = 1000 # Total number of frames
  timeScale = totalTime/sampling
  data.selected <-data$f[range]

```

```

#lets normalize the data

data.selected<-normalise(data.selected)
end<-round(length(data.selected)/2)

LowFreqRange<-1:3
HighFreqRange<-(end-4):end


ReFreqDomainFiltered<- filterTimeSeries(data.selected, LowFreqRange, HighFreqRange, end,
timeScale)

ReFreqDomainFiltered<-ReFreqDomainFiltered[range,]

#plot(ReFreqDomainFiltered)
return(ReFreqDomainFiltered)
}


normalise<-function(d)
{
d<as.vector(d)
d<-(d- min(d))/(max(d) - min(d) )
return(d)
}

```

Plot a histogram

```

A <- read.table ("WT_singlefreq.txt")
A.dD<- read.table ("dD_singlefreq.txt")

```

```

B <- A [-1]
B.dD <- A.dD [-1]

```

```

D<-c(B[1,])
D.dD<-c(B.dD[1,])

```

```

A2 <- read.table ("WT_doublefreq.txt")
A2.dD<- read.table ("dD_doublefreq.txt")

```

```

B2 <- A2 [-1]
B2.dD <- A2.dD [-1]

```

```

D2<-c(B2[1,], B2[2,])
D2.dD<-c(B2.dD[1,], B2.dD[2,])

```

```

D<-as.numeric(D)
D.dD<-as.numeric(D.dD)

D2<-as.numeric(D2)
D2.dD<-as.numeric(D2.dD)

par(cex.lab = 1.5, cex = 1.5, cex.axis = 1.5)

layout(matrix(1:4,1,4))

hist (D, freq = F, border = "white", col = 'gray', ylim = c(0,0.08), xlim = c(0,45), main = "WT population of
single CBF", xlab = "freq (Hz)" )

lines (density(D),lty = 2, col = 'red', lwd = 3)

hist (D.dD, freq = F, border = "white", col = 'gray', ylim = c(0,0.08), xlim = c(0,45), main = "deltaD mutant
population of single CBF", xlab = "freq (Hz)" )

lines (density(D.dD),lty = 2, col = 'red', lwd = 3)

hist (D2, freq = F, border = "white", col = 'gray', ylim = c(0,0.08), xlim = c(0,45), main = "WT population of
double CBF", xlab = "freq (Hz)" )

lines(density(D2),lty = 2, col = 'red', lwd = 3)

hist(D2.dD, freq = F, border = "white", col = 'gray', ylim = c(0,0.08), xlim = c(0,45), main = "deltaD mutant
population of double CBF", xlab = "freq (Hz)" )

```

Plot a pie-chart

```

pie.CBF_dD<-c(74, 18, 2, 6)
pie.CBF_WT<-c(60, 35, 1, 2)

names(pie.CBF_WT)<-c("single CBF", "double CBF", "other", "immotile cilia")
names(pie.CBF_dD)<-c("single CBF", "double CBF", "other", "immotile cilia")

pie(pie.CBF_WT, col= c("dimgray", "grey80", "black", "white"), clockwise=F, main="WT CBF population")
pie(pie.CBF_dD, col= c("dimgray", "grey80", "black", "white"), clockwise=F, main="deltaD mutant CBF
population")

```

Plot a box-plot

```

A <- read.table ("WT_singlefreq.txt")
A2 <- read.table ("WT_doublefreq.txt")

A.dD<- read.table ("dD_singlefreq.txt")
A2.dD<- read.table ("dD_doublefreq.txt")

```

```
B <- A [-1]
```

```
B.dD <- A.dD [-1]
```

```
D<-c(B[1,])
```

```
D.dD<-c(B.dD[1,])
```

```
D<-as.numeric(D)
```

```
D.dD<-as.numeric(D.dD)
```

```
Boxplot (D2, D, D2.dD, D.dD, horizontal=T, col = 'gray', xlab = "freq (Hz)", names=F)
```

```
B2 <- A2 [-1]
```

```
B2.dD <- A2.dD [-1]
```

```
D2<-c(B2[1,], B2[2,])
```

```
D2.dD<-c(B2.dD[1,], B2.dD[2,])
```

```
D2<-as.numeric(D2)
```

```
D2.dD<-as.numeric(D2.dD)
```

Wilcoxon test in CBF data

```
A <- read.table ("WT_singlefreq.txt")
```

```
A.dD<- read.table ("dD_singlefreq.txt")
```

```
A2 <- read.table ("WT_doublefreq.txt")
```

```
A2.dD<- read.table ("dD_doublefreq.txt")
```

```
B <- A [-1]
```

```
B.dD <- A.dD [-1]
```

```
B2 <- A2 [-1]
```

```
B2.dD <- A2.dD [-1]
```

```
D<-c(B[1,])
```

```
D.dD<-c(B.dD[1,])
```

```
D2<-c(B2[1,], B2[2,])
```

```
D2.dD<-c(B2.dD[1,], B2.dD[2,])
```

```
D<-as.numeric(D)
```

```
D.dD<-as.numeric(D.dD)
```

```
D2<-as.numeric(D2)
```

```
D2.dD<-as.numeric(D2.dD)
```

```
wilcox.test(D, D2)
```

```
data: D and D2
```

```
W = 1032.5, p-value = 0.02412
```

```
wilcox.test(D, D.dD)
```

```
data: D and D.dD
```

```
W = 1226.5, p-value = 0.003234
```

```
wilcox.test(D2, D2.dD)
```

```
data: D2 and D2.dD
```

```
W = 618.5, p-value = 0.1284
```

```
wilcox.test(D.dD, D2.dD)
```

```
data: D.dD and D2.dD
```

```
W = 806, p-value = 0.003294
```


Wilcoxon test in double frequency data

```
A <- read.table ("WT_1stfreq_only.txt")
A.dD<- read.table ("dD_1stfreq_only.txt")
A2 <- read.table ("WT_2ndfreq_only.txt")
A2.dD<- read.table ("dD_2ndfreq_only.txt")
```

```
B <- A [-1]
B.dD <- A.dD [-1]
B2 <- A2 [-1]
B2.dD <- A2.dD [-1]
```

```
D<-c(B[1,])
D.dD<-c(B.dD[1,])
D2<-c(B2[1,], B2[2,])
D2.dD<-c(B2.dD[1,], B2.dD[2,])
```

```
D<-as.numeric(D)
D.dD<-as.numeric(D.dD)
D2<-as.numeric(D2)
D2.dD<-as.numeric(D2.dD)
```

```
wilcox.test(D, D.dD)
      data: D and D.dD
      W = 187.5, p-value = 0.02226
```

```
wilcox.test(D2, D2.dD)
      data: D2 and D2.dD
      W = 142, p-value = 0.5613
```

```
wilcox.test(D, D2)
      data: D and D2
      W = 417.5, p-value = 7.642e-07
```

```
wilcox.test(D.dD, D2.dD)
```

data: D.dD and D2.dD

W = 109, p-value = 0.03442

Fisher test to CBF populations

```
A<-read.table("CBF distributions_WT and dD.txt")
```

```
fisher.test(A)
```

p-value = 0.1374

t student's test to KV fluid flow velocities

```
t.test(WT_KV, deltaD_KV)
```

Welch Two Sample t-test

data: WT_KV and deltaD_KV

t = -1.7596, df = 36.691, p-value = 0.08681

Variability analysis of frequencies: Brown-Forsythe Levene's test.

```
freq1.wt<-as.numeric(unlist(read.table("Wt_1stfreq_only.txt", header = T)))
```

```
freq2.wt<-as.numeric(unlist(read.table("Wt_2ndfreq_only.txt", header = T)))
```

```
freq1.dD<-as.numeric(unlist(read.table("dD_1stfreq_only.txt", header = T)))
```

```
freq2.dD<-as.numeric(unlist(read.table("dD_2ndfreq_only.txt", header = T)))
```

```
coef.var.wt.f1<-coeff.of.var(freq1.wt); coef.var.wt.f1
```

```
coef.var.wt.f2<-coeff.of.var(freq2.wt); coef.var.wt.f2
```

```
coef.var.dD.f1<-coeff.of.var(freq1.dD); coef.var.dD.f1
```

```
coef.var.dD.f2<-coeff.of.var(freq2.dD); coef.var.dD.f2
```

```

freq1.wt.f<-rep("WT1", length(freq1.wt))
freq2.wt.f<-rep("WT2", length(freq2.wt))
freq1.dD.f<-rep("dD1", length(freq1.dD))
freq2.dD.f<-rep("dD2", length(freq2.dD))

```

```

freq.wt<-c(freq1.wt, freq2.wt)
freq.wt.f<-as.factor(c(freq1.wt.f, freq2.wt.f))
leveneTest( freq.wt, freq.wt.f)

```

```

freq1.wt.dD<-c(freq1.wt, freq1.dD)
freq1.wt.dD.f<-as.factor(c(freq1.wt.f, freq1.dD.f))
leveneTest(freq1.wt.dD, freq1.wt.dD.f)

```

```

freq.wt1.dD2<-c(freq1.wt, freq2.dD)
freq.wt1.dD2.f<-as.factor(c(freq1.wt.f, freq2.dD.f))
leveneTest(freq.wt1.dD2, freq.wt1.dD2.f)

```

```

freq.wt2.dD1<-c(freq2.wt, freq1.dD)
freq.wt2.dD1.f<-as.factor(c(freq2.wt.f, freq1.dD.f))
leveneTest(freq.wt2.dD1, freq.wt2.dD1.f)

```

```

freq.wt2.dD2<-c(freq2.wt, freq2.dD)
freq.wt2.dD2.f<-as.factor(c(freq2.wt.f, freq2.dD.f))
leveneTest(freq.wt2.dD1, freq.wt2.dD2.f)

```

```

freq.dD<-c(freq1.dD, freq2.dD)
freq.dD.f<-as.factor(c(freq1.dD.f, freq2.dD.f))
leveneTest( freq.dD, freq.dD.f)

```

Variability analysis of KV particles velocity: Brown-Forsythe Levene's test.

```
v.wt<-read.table("WT_KV_copy.txt", header = F)
v.dD<-read.table("deltaD_KV_copy.txt", header = F)
```

```
coeff.of.var <- function(x)      {
    f<-100*sd(x)/mean(x)
    return(f)
}
```

```
v.wt<-as.numeric(unlist(v.wt))
v.dD<-as.numeric(unlist(v.dD))
```

```
coef.var.wt<-coeff.of.var(v.wt); coef.var.wt
coef.var.dD<-coeff.of.var(v.dD); coef.var.dD
library(car)
```

```
v.wt.f<-rep("WT", length(v.wt))
v.dD.f<-rep("dD", length(v.dD))
```

```
v<-c(v.wt, v.dD)
```

```
v.f<-as.factor(c(v.wt.f, v.dD.f))
leveneTest(v, v.f)
```

Annex III

Supplemental data

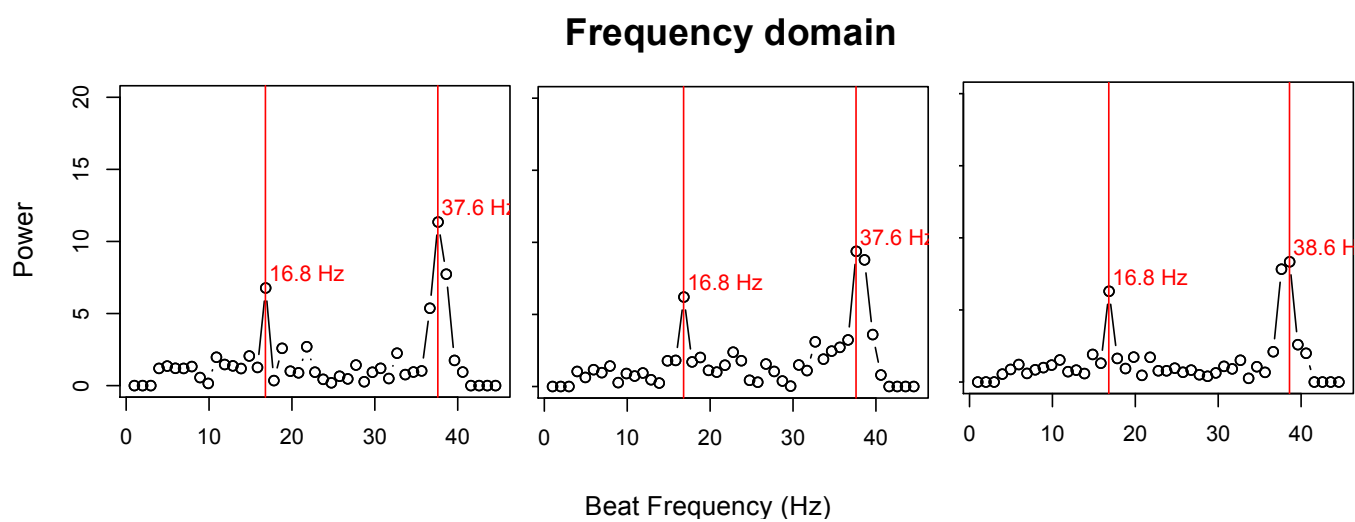


Figure S1 – Three CBF measurements of a single cilium in a WT embryo revealed similar FFT spectra. Randomly measuring any 10 periods along 1000 frames revealed similar FFT spectra - measured frequencies are depicted as vertical red lines.

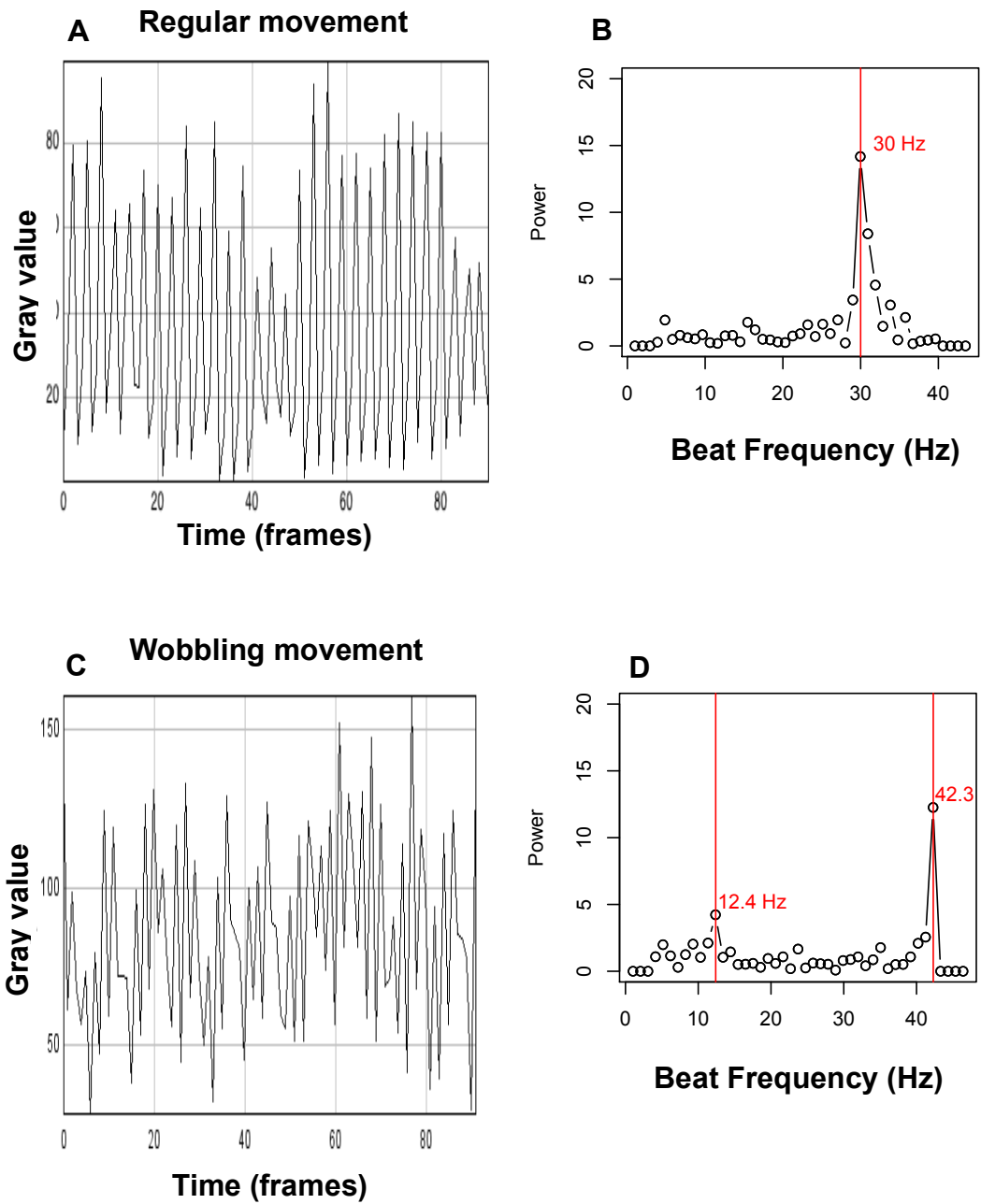


Figure S2 - Two CBF types identified in the KV of a WT embryo. Line profile of a cilium beating at a single (A), or two simultaneous frequencies (C), the change of gray value intensity indicates movement in/out of the observation plane. The corresponding measured frequencies are depicted in their Fourier spectra as vertical red lines (B, D). Note the pattern differences between regular and 'wobbling' movement.

CD

Movie S1 – DIC movie showing several motile cilia beating inside one wild-type zebrafish Kupffer's vesicle.

Movie S2 – DIC movie showing a cilium beating inside one wild-type zebrafish Kupffer's vesicle.

Movie S3 – *deltaD*^{-/-} mutant Kupffer's vesicle with tracked particles inside. Using the plugin MTrackJ from ImageJ program we could track native KV particles, thus calculating the KV fluid-flow velocity. See section 2.3 and section 3.3 for detailed information.

